6-12-2017

Structural, Optical and Catalytic Properties of Bimetallic and Metal-Semiconductor Nanorods

Sravan Kumar Thota
University of Connecticut - Storrs, sravan.thota@uconn.edu

Structural, Optical and Catalytic Properties of Bimetallic and Metal-Semiconductor Nanorods

Sravan Kumar Thota, Ph.D.

University of Connecticut, 2017

Metal and semiconductor nanomaterials exhibit highly tunable electric, magnetic, optical and catalytic properties. To obtain desired properties, structure and composition of the nanomaterials must be fine-tuned, which requires fundamental understanding of the growth mechanism. In the thesis research, we study Au-Cu alloy nanorods (NRs) growth mechanism using single particle scattering spectroscopy. From electrodynamics simulations, it was revealed that the unusual features of the single particle scattering spectra were due to atomic level structural defects made up of few atoms on the surface of NRs, caused by galvanic replacement reaction (GRR). NRs are further explored as templates for GRR using $HAuCl_4$. Interestingly, NRs transformed into hollow rods or break into nanospheres via a hollow junction dumbbell shaped intermediate, at different concentrations of $HAuCl_4$. The hollow rods showed enhanced catalytic activity for *p*-nitrophenol reduction, while dumbbell shaped intermediates displayed junction dependent optical properties. Later plasmon-exciton interactions in Ag-CdS hybrid nanorods were explored. The absorption studies revealed mixed electronic states at the metal semiconductor interface while the CdS length dependent photoluminescence displayed by hybrid nanorods was trap state emission. Our detailed studies of the structural transformation mechanisms and corresponding optical properties provide guidance to fabricate nanomaterials with tunable structure and compositions for exciting applications.

Structural, Optical and Catalytic Properties of Bimetallic and Metal-Semiconductor Nanorods

Sravan Kumar Thota

M.Sc. Integrated Chemistry, Kakatiya University, **2011**

A Dissertation

Submitted in Partial Fulfillment of the

Requirements for the Degree of

Doctor of Philosophy

at the

University of Connecticut

2017

2017

APPROVAL PAGE

Doctor of Philosophy Dissertation

Structural, Optical and Catalytic Properties of Bimetallic and Metal-Semiconductor Nanorods

Presented by

Sravan Kumar Thota, M.Sc. Integrated

Major Advisor _____
Dr. Jing Zhao

Associate Advisor _____
Dr. Steven L. Suib

Associate Advisor _____
Dr. Rebecca Quardokus

University of Connecticut

2017

Dedicated To

My late sister Ms. Srujana

Acknowledgements

I would like to thank my major Advisor, Dr. Jing Zhao for her immense support and exceptional guidance throughout my PhD career. She gave me the freedom to work on new ideas and encouraged independent thinking. Her tremendous confidence in me always motivated me to steer through tough times. I would like to thank my advisory committee, Dr. Steven Suib, Dr. Rebecca Quardokus, Dr. Douglas Adamson and Dr. Robert Mason for their valuable insights and support during these years. I would like to thank Dr. Xudong Yao and Dr. Fatma Selampinar for their constant support and knowledge. I would also like to thank my collaborator Dr. Shengli Zou (University of Central Florida) and his graduate student Yadong Zhou for providing us with theoretical calculations and simulations, which played a major role in explaining my research in the thesis work. I would take this opportunity to express my gratitude to Dr. Shutang Chen, an alumnus post-doc in the group, a good mentor, colleague and a great friend. The discussions we had outside the lab are some of the best memories during my Ph.D. life. I would like to thank my colleagues and good friends Dr. Swayandipta Dey and Dr. Julie Jenkins for support on my projects and for all of the endless conversations we had in the lab. I would like to thank my lab members Terianna Wax, Yi Luo, Xudong Wang, Yongchen Wang, Yonglei Sun for their constant support.

Special thanks to Dr. Roger Ristau and Dr. Lichun Zhang for the electron microscopy training and constant feedback and help with the instruments. I would like to thank University of Connecticut, Department of Chemistry and CAMMA Center at Institute of Materials Science for the all the instrumentation facilities and support over these years.

I would like to acknowledge the financial support from FEI industries, Department of Chemistry and Graduate school of UCONN.

Thanks to my family for their support and encouragement during all these years. Thank you, Mom and Dad, for always believing in me and encouraging me to pursue my dreams. I couldn't end a day without speaking to my mom, and she is my ultimate backbone for who I am today and what I would be in the future. I couldn't thank enough my better half Spandana for her constant support and motivation. Thanks for going through ups and downs in the life together. A very special thanks to my sister Samatha and brother in law Vasudev for guiding me through all the obstacles and all the personal support and constant mentoring. It was always the cute little smiles of my niece and nephews Manaswini, Charvik and Deetya, which made this world much more happier place for me. I would also like to thank my father in law Venugopala Chary for his kind support and encouragement. Special thanks to my cousin brother Kiran and all my little cousins for the fun and support all the time. I would like to thank my best friends and childhood buddies Ashish and Ravi Teja for being there for me every time when needed. I would also like thank my friends Sathish, Prithvi, Shiva and Praveen. I would like to thank and my friends here at UCONN, Karteek, Spundana, Santosh, Divya, Saketh, Meera Nair and all my well-wishers and everyone else, for all the encouragement and support during this journey. Finally, my thanks and praise to God who has blessed me tremendously.

Table of Contents

List of Schemes

List of Figures

List of Tables

Chapter 1. Introduction

1.1 Metal Nanoparticles

The properties of the matter at nano dimensions (5-100 nm) are different from that of bulk state and single atomic state. Especially, there is drastic increase in the surface areas compared to the bulk causing high densities of low coordination numbered atoms on the surface. This give rise to excellent catalytic activity for nanomaterial's compared to bulk. Among other nanomaterial's, metals nanoparticles were proved to be highly efficient catalysts due to optimum d-band energies for adsorption and release of the reactants. For example, Ru, Rh, Ir, Pd and Pt metal nanoparticles have been already used as heterogeneous catalysts in industries for large scale productions.[1] Also, metal nanoparticles are known to exhibit unique magnetic and optical properties at nano dimensions. For example metal nanoparticles like Fe, Co and Ni are known to exhibit strong magnetic fields locally, due to a phenomenon called super paramagnetism. Furhtermore, metals display size and shape dependent optical properties at nano dimensions. For example noble metal nanoparticles like Au, Ag and Cu support a unique phenomenon called localized surface plasmon resonance (LSPR).[1] Overall, metals exhibit unique catalytic, magnetic and optical properties, when they are reduced to nano dimensions.

1.2 Localized Surface Plasmon Resonance

The loosely held electrons in metal nanoparticles oscillate collectively when exposed to external electromagnetic radiation. If the oscillation frequency matches with that of

external source, resonance occurs, giving rise to LSPR. [2-4] The frequency, at which the resonance happens, depends on the local dielectric field constant of the medium, composition, and morphology of the nanoparticle. In particular, plasmonic materials like Au, Ag and Cu have resonance frequency in the visible region making them viable for many applications. LSPR causes increased sensitivity to local media, enhanced absorption and scattering cross sections, and strong electric and thermal fields locally.[5] As a result, metal nanoparticles find applications in sensing, bio imaging, surface enhanced spectroscopies like surface enhanced Raman spectroscopy (SERS), catalysis, photo thermal therapy etc.[3, 6-10] LSPR and the resulting properties can be fine tuned by controlling the composition and morphology of the nanoparticle. Over the past decade, shape control for monometallic nanoparticles has been achieved using bottom up synthetic methods like co-reduction, thermal decomposition, seed-mediated growth and galvanic replacement.[11] Much of current research is dedicated to composition control creating multimetallic nanoparticles, where LSPR can be tuned by changing both the composition and morphology.

1.3 Bimetallic Nanoparticles

Phase miscibility at nanometer regime, provides unique opportunity to combine different elements forming multimetallic nanoparticles. Particularly, bimetallic nanostructures pose to be unique systems with multifunctionality and enhanced properties compared to their components.[1, 12-16] Although bimetallic nanostructures are made up of only two metals, they can differ in their architecture based on the crystal structure, internal defects, atomic ordering and spatial distribution.[13] According to the spatial distribution of the two elementals, bimetallic nanoparticles are classified into alloy, core-shell and hetero

structures. Lattice constants, metal–metal bonding energies, reaction kinetics and the ligands are the important factors, which dictate the resulting bimetallic configuration during the synthesis.[1, 17] Bimetallic systems composed of Au-Ag, Au-Pd, Au-Pt, Ag-Cu, Pd-Pt, Pd-Rh, Pt-Ag in various configuration have been fabricated so far.[1] Especially, Au-Ag and Pt-Pd systems are most studied bimetallic systems for plasmonic and electrochemical catalytic applications, respectively.[18] Recently, Au-Cu emerged as another promising bimetallic system, which has shown excellent catalytic activity for carbon dioxide reduction in the alloyed configuration.[14]

1.4 Au-Cu alloy system

Au-Cu system has a synergistic effect of stability and cost reduction imparted by Au and Cu respectively. Hence, it can be explored for multiple applications. For example, Au-Cu alloy system have attracted lot of attention due to their high catalytic activity for partial oxidation of methanol to produce hydrogen fuels and catalytic oxidation of benzyl alcohol, CO and propene.[19] The selectivity and reactivity of the system depends on its morphology, crystal structure and internal defects. To obtain Au-Cu alloy nanoparticles of different morphologies and crystal structures, bottom up synthetic techniques have been developed in both the organic and aqueous phase, as discussed below.

1.4.1 Morphology Control

The morphology and crystal structure of the final product is dictated by the reaction pathways, controlled by the synthetic method choosen.[1] Broadly Au-Cu alloy synthetic protocols are classified into co-reduction, seed mediated growth and a combination of

both. A few examples of well-defined synthetic protocols with high yields are discussed here.

1.4.1.1 Co-reduction method

Co-reduction is a one-step, most straightforward synthetic method for generating Au-Cu alloy nanostructures. In this method, both Au and Cu precursors are reduced simultaneously. Reducing agent plays a key role in defining the reaction pathways. By changing relative reduction potential of reducing agents with respect to metal precursors, various morphologies can be generated. For example, spherical Au-Cu alloy particles have been fabricated using a co-reduction method developed by Schaak and co-workers[20]. In this method, 1-octadecene, oleic acid and oleylamine were used as the reducing and stabilizing ligands. $Au_{1-x}Cu_x$ alloy nanoparticles with x values varying from 0 to 0.5 were achieved by varying the amount of Cu precursor in the synthesis. The sample obtained was around 8 nm in size, with uniform size distribution and disordered crystal structure. Not only spherical, but also asymmetric geometries like nanowires have been achieved using co-reduction method. Again controlling reaction kinetics using reducing agent plays a key role in obtaining asymmetric geometries. For example, Au-Cu alloy nanowires were synthesized in the aqueous phase by Zhang and coworkers.[21] $NaBH_4$ was used as a strong reducing agent in this protocol. The reducing agent creates fast nucleation process at the initial stages. Along with this weak binding of the non-ionic surfactant Triton X-100 favored asymmetric addition, leading to the nanowire growth. Au-Cu alloy nanowires were polycrystalline, with a diameter around 3.5 nm and a length of several hundred nanometers. Following these methods, co-reduction strategy was extended to fabricate complex, three-dimensional geometries like nanocubes. For

example, uniform, single crystalline Au-Cu alloy nanocubes were synthesized by Walker and coworkers[22] using co-reduction. In this work 1,2-hexadecanediol is used as the reducing agent. Due to the mild reducing nature of 1,2-hexadecanediol, the reaction kinetics during initial nucleation process was slow. Slow kinetics allowed selective addition of the atoms on the preformed crystal. Au-Cu alloy nanocubes of edge lengths of 3.4, 5, 23, 45 and 85 nm with Au:Cu ratios between 3:1 to 1:3 were synthesized by varying the relative amount of precursors to reducing agent. Therefore, choosing the proper reducing agent and optimizing reaction conditions can lead to fabrication Au-Cu alloy nanoparticles of various geometries, such as spherical particles, nanowires and nanocubes, in a one-step co-reduction method.

1.4.1.2 Seed-mediated Strategy

Although co-reduction can generate different Au-Cu alloy structures, it's difficult to find common conditions to control the reduction of Au and Cu precursors most of the time. The difference in the physicochemical properties like redox potential, crystal structure, melting point etc cause inherent difficulties during the synthesis. Fine-tuning the morphology and composition at the same time is difficult to achieve using co-reduction methods. Seed mediated strategy is the most popular method for generation of bimetallic structures with complex morphologies.[1] In this strategy, a well-defined crystal (seed) made of Au is synthesized first. The Au seeds then serve as hetero nucleation sites for the incoming Cu atoms to attach on. Various protocols have been reported to fabricate well-controlled Au-Cu alloy structures by seed mediated strategy. For example, Li and coworkers[23] synthesized intermetallic (ordered) Au-Cu spherical particles using a seed mediated growth method. In this process, homogeneous collision of Cu atoms or clusters

occurred on the preformed Au seed surface, followed by diffusion of Cu atoms into the Au lattice. The particles were then annealed at elevated temperatures to form ordered Au-Cu alloy. Temperature required for annealing varied with the desired composition of final product (AuCu to $AuCu_3$). Seed mediated strategy was also extended to fabricate anisotropic structures like nanorods, which were difficult to achieve using co-reduction methods. Sonnichsen and coworkers[24] made Au-Cu alloy nanorods in aqueous phase using a seed mediated strategy. In this protocol, ascorbic acid was used as a mild reducing agent, while cetyl trimethylammonium bromide (CTAB) promoted the asymmetric growth, similar to that for Au nanorods.[25] Later in 2013, Chen and coworkers[26] developed an organic phase seed mediated protocol for the synthesis of $AuCu_3$ alloy nanorods using Au nanoparticles as seeds. Oleylamine acts as the solvent and mild reducing agent. Cu binds on one side of the Au seed at the initial stages, followed by inter diffusion of atoms at elevated temperatures. Prospectively, many complex Au-Cu alloy structures can be expected using seed mediated growth strategy.

1.4.1.3 Combined Co-reduction and Seed-mediated Strategy

Co-reduction and seed mediated strategies can be combined in a synthetic protocol to achieve structures with sharp tips for better catalytic and sensing applications. Preformed Au seeds with reactive sites allow growth only along specific directions creating sharp edges or branches, while co reducing Au and Cu precursors simultaneously allowa to fine tune the composition of the nanocrystals. For example, Au-Cu alloy nanopentacles were fabricated by Hou and coworkers[27] using co-reduction combined with seed mediated growth. Glucose acts as a strong reducing agent and helps in the formation of Au penta-twinned seeds at initial stages. Selective binding of hexadecylamine to (110) facets of the

seed later favored the addition of co-reduced Au and Cu atoms along twinning planes. This selective growth accompanied by slow kinetics, due to decrease in glucose concentration results in the branches and pentacle structure. By varying the precursor to reducing agent ratio, composition of nanopentacles can be tuned. Hence, choosing bottom up synthetic strategies, Au-Cu alloy structures of different morphologies and compositions can be fabricated. The Au-Cu alloy nanoparticles of different morphologies have been further explored for their optical and catalytic properties.

1.4.2 Optical Properties

Au and Cu nanoparticles are active plasmonic materials with LSPR frequencies in the visible region. For example, 20 nm spherical Au and Cu nanoparticles display LSPR bands at 520 and 560 nm respectively.[28] Alloying of Cu with the stable Au phase prevents the oxidation of Cu and gives rise to optical properties different from Au or Cu. LSPR of Au-Cu alloy particles display single or multiple peaks depending on their geometry and composition. For example, Au_xCu_{1-x} (x= 0 to 0.5) alloy nanoparticles of sizes 8-13 nm display a single peak in the visible region.[20] Alloying of Cu into Au caused a red shift and broadening of LSPR. In particular a red shift from 523 nm to 545 nm was observed when Cu content was increased from 0 to 48 %. The LSPR of Au-Cu alloy nanocubeshad a single broad peak at an intermediate wavelength between that of Au and Cu nanocubes.[22] The LSPR of the alloy nanocubes red shifted with increase in the cube size. Butthe expected higher order modes for the cubes are absent in alloy system.[28] When the geometry becomes anisotropic like rods, two peaks were displayed, one due to transverse mode and other due to the longitudinal mode. For example, Au-Cu alloy nanorods with aspect ratio of 3 displayed two peaks, although transverse mode was very

weak and sometimes absent.[24] The longitudinal plasmon mode was strong and sensitive to the composition change. It red shifted from 720 nm to 820 nm when the Au: Cu ratio was changed from 4:1 to 1:1. Interestingly, the alloy nanorods displayed a small blue shift of the longitudinal mode from 820 to 780 nm when the Cu content was further increased from 1:1 to 1:4.

The LSPR of the Au-Cu alloy systems also has multiple peaks when the morphology becomes more complex. For example, the LSPR of 70 nm Au-Cu alloy pentacle particles had three bands.[27] A major peak was found at 1100 nm, which is dipolar in nature, while two higher order modes were observed at 740 and 550 nm. Similarly, the 200 nm pentacles displayed three peaks at 1400, 810 and 530 nm. Overall, Au-Cu alloy nanoparticles have LSPR bands in the visible wavelength region, which are sensitive to the geometry and composition of the nanoparticle. As the geometry changes from simple spherical shape to complex nanopentacles, multiple peaks appeared due to higher order modes. Also, a common trend of red shift with increase in the size or Cu content was observed for all morphologies. Along with optical properties, Au-Cu system has been explored for exciting applications like photo thermal therapy and catalysis. Although Au-Cu alloy nanoparticles of different morphologies are fabricated, most of the products are polycrystalline and disordered in nature. There is still need to better control the defects and crystal structure of the nanoparticles, and to further fine-tune their shape and composition.

1.4.3 Structural Defects in Au-Cu

In bimetallic alloy NPs, structural instabilities/defects are commonly observed during the

alloy process.[16] The defects likely arise from lattice strain created by the mismatch of lattice parameters when combining the two metals. For example, in Au-Pd and Au-Cu alloy NPs, lattice strain builds up due to different atomic radii, leading to defects in the structure.[18, 27, 29-32] Even in systems like Au-Ag[32, 33] alloy NPs, where the lattice constants are similar, vacancy sites at the bimetallic interface migrate to the surface in alloying process, resulting in defects formation. Detailed studies of these structural defects at the atomic level will help to understand alloying mechanism and overcome the synthetic challenges. In our study, we demonstrate that, structural defects of few atomic layers in Au-Cu alloy nanorods can be detected using single particle scattering spectroscopy with the aid of discrete dipole approximation (DDA) simulations.[34]

1.4.4 Galvanic Replacement on Au-Cu

Due to the inherent difficulty in shape-controlled bimetallic nanoparticle synthesis, and unavoidable defects as explained above, post-synthetic modification approach like galvanic replacement reaction (GRR) has emerged as alternate strategy recently[35]. In a typical GRR, the metal precursor with higher reduction potential will oxidize the metal nanoparticle with lower reduction potential and gets deposited on the nanostructure. Remarkable progress has been made in creating bimetallic hollow nanostructures from monometallic nanoparticle templates using GRR in the last decade.[36-41] However, little is known about GRR using alloy nanoparticles as templates, where the reactivity of the metals in the alloy is different from that of the metal in the pure phase. This difference can potentially lower the GRR rates, allowing the diffusion of atoms at the boundary between different metals to play a more significant role in determining the hollow structure formation. In our study we use Au-Cu alloy rods as a model bimetallic template

for GRR with $HAuCl_4$ as the oxidizing agent. Elemental mapping and single particle scattering spectroscopy in combination with DDA simulations have been used to understand different reactions pathways. Catalytic and optical properties of products are also explored.[42, 43]

1.5 Metal-Semiconductor Hybrid Nanorods

Hybrid structures can be present in three configurations like core-shell, alloy and hetero structures.[13] Alloy and core-shell structures have been explored in bimetallic particles, especially for Au-Cu composition in our study. Hetero structure is another unique configuration where components are not mixed but finely combined into a single nanostructure as separate parts. The two components can be metals, semiconductors, or a metal and a semiconductor. Metal and semiconductor hybrid systems pose to be promising materials for photo catalysis due to the charge transfer that may occur between the metal and the semiconductor. In this process, the excited electron in the conduction band of semiconductor is transferred to the metal's Fermi level when it is aligned well with the electronic states of semiconductor. Later, the hybrid nanorods with electron rich metal surface can be explored for photo catalytic activity. Also, the strong interaction between the exciton and plasmon states can result in enhanced optical functionalities. For example Au-CdS hybrid rods displayed increased absorption cross-section in the visible region compared to individual components.[44] Detailed studies on the structural and optical properties of these hybrid structures will provide opportunity for improving the efficiency of photo catalysts, soalr cells, photoelectric devices, and biological labelling[44]. In our study, Ag-CdS metal–semiconductor hybrid nanorods, with three different lengths of CdS part were fabricated to explore the plasmon–exciton interactions. Optical studies

reveal unique absorption properties and unexpected photoluminescence of the Ag-CdS nanorods.

1.6 Overview of Dissertation

The goal of this dissertation was to study the structural, optical and catalytic properties of multi-component nanosystems. Two systems, bimetallic Au-Cu alloy nanorods and metal-semiconductor Ag-CdS nanorods were studied. A seed mediated growth strategy was used to fabricate these materials and later GRR was used as post synthetic modification strategy to fine tune their structure and composition. The fabricated structures showed optical properties, which are very sensitive to the small changes in morphology and enhanced catalytic activity compared to their components. The work has been organized into five chapters.

Chapter 1 focuses on introducing the fundamental concepts and applications of metal nanoparticles and hybrid systems. Along with the basic concepts, representative examples in the literature, has been discussed in order to introduce the evolution of the field. Detailed review has been given on the morphology control and corresponding optical properties of hybrid systems. An overview of the work completed in this dissertation was also presented in this chapter.

Chapter 2 focuses on understanding the growth mechanism of Au-Cu alloy nanoords. Single particle spectroscopy was used to monitor the growth of Au-Cu alloy nanorods together with transmission electron microscopy. Electrodynamics simulations have revealed that small structural defects of a few atomic layers formed during growth split the scattering peaks, giving rise to plasmon modes, which do not exist in defect-free rods

of similar geometry. The study shows that single particle scattering spectrum is very sensitive to atomic level structural defects.

Chapter 3 focuses on post-synthetic modifications to Au-Cu alloy nanorods using GRR. Transformation of $AuCu_3$ nanorods to hollow rods during GRR was monitored. Asymmetric Cu diffusion was revealed due to the difference in the Cu content at the two ends of the $AuCu_3$ nanorod precursors. The hollow Au-Cu nanorods were excellent catalysts for *p*-nitrophenol reduction with a k_{app}/m^2 value of 205, which was 5 times higher than solid alloy rods. Understanding of the hollow alloy structure formation mechanism opens up possibility to precisely control the internal structure of these nanoparticles for exciting applications.

Chapter 4 focuses on controlling the kinetics of oxidation in Au-Cu alloy nanorods during GRR by varying the $HAuCl_4$ precursor concentration. Changing kinetics resulted in either Au-Cu hollow rods or AuCu@Au core-shell spheroids. Interestingly, a critical intermediate state with a hollow junction and dumbbell shape was observed in the later case. Single particle spectroscopy together with electrodynamic simulations showed that varying the dimensions of the hollow part altered the plasmon resonance drastically, revealing that single particle LSPR can be used as an exquisite tool to probe the internal structure of the nanoscale junctions.

Chapter 5 focuses on optical interactions in metal-semiconductor hybrid systems. Ag-CdS hybrid structures with three different lengths of CdS part were fabricated by varying reaction time. The absorption and emission properties of the hybrid rods were further examined to understand the plasmon–exciton interactions. Optical studies revealed unique absorption properties due to mixed electronic states of Ag and CdS. Hybrid

nanorods also displayed photoluminescence owing to the trap state emissions from the CdS part, which is also dependent on the dimension of CdS.

1.7 References

1. K. D. Gilroy, A. Ruditskiy, H.-C. Peng, D. Qin and Y. Xia, *Chem. Rev.*, 2016, **116**, 10414-10472.
2. M. G. Blaber, M. D. Arnold and M. J. Ford, *J. Phys: Condens. Matter*, 2010, **22**, 143201.
3. M. Hu, J. Chen, Z.-Y. Li, L. Au, G. V. Hartland, X. Li, M. Marquez and Y. Xia, *Chem. Soc. Rev.*, 2006, **35**, 1084-1094.
4. E. M. Perassi, C. Hrelescu, A. Wisnet, M. Döblinger, C. Scheu, F. Jäckel, E. A. Coronado and J. Feldmann, *ACS Nano*, 2014, **8**, 4395-4402.
5. S. Sarina, E. R. Waclawik and H. Zhu, *Green Chemistry*, 2013, **15**, 1814-1833.
6. P. Chen, X. Zhou, N. M. Andoy, K.-S. Han, E. Choudhary, N. Zou, G. Chen and H. Shen, *Chem. Soc. Rev.*, 2014, **43**, 1107-1117.
7. V. Giannini, A. I. Fernández-Domínguez, S. C. Heck and S. A. Maier, *Chem. Rev.*, 2011, **111**, 3888-3912.
8. A. Walther and A. H. Muller, *Chem. Rev.*, 2013, **113**, 5194-5261.
9. S. E. Skrabalak, J. Chen, Y. Sun, X. Lu, L. Au, C. M. Cobley and Y. Xia, *Acc. Chem. Res.*, 2008, **41**, 1587-1595.
10. M. J. Mulvihill, X. Y. Ling, J. Henzie and P. Yang, *J. Am. Chem. Soc.*, 2009, **132**, 268-274.
11. N. E. Motl, A. F. Smith, C. J. DeSantis and S. E. Skrabalak, *Chem. Soc. Rev.* 2014, **43**, 3823-3834.
12. D. M. Alonso, S. G. Wettstein and J. A. Dumesic, *Chem. Soc. Rev.*, 2012, **41**, 8075-8098.
13. M. B. Cortie and A. M. McDonagh, *Chem. Rev.*, 2011, **111**, 3713-3735.
14. D. Kim, J. Resasco, Y. Yu, A. M. Asiri and P. Yang, *Nat. Commun.*, 2014, **5**, 4948
15. T. Krenke, E. Duman, M. Acet, E. F. Wassermann, X. Moya, L. Manosa and A. Planes, *Nat. Mater.*, 2005, **4**, 450-454.
16. N. Wang, Y. Han, Y. Xu, C. Gao and X. Cao, *Anal. Chem.*, 2014, **87**, 457-463.

17. S. E. Habas, H. Lee, V. Radmilovic, G. A. Somorjai and P. Yang, *Nat. Mater.*, 2007, **6**, 692-697.
18. B. Lim, M. Jiang, P. H. C. Camargo, E. C. Cho, J. Tao, X. Lu, Y. Zhu and Y. Xia, *Science*, 2009, **324**, 1302-1305.
19. C. L. Bracey, P. R. Ellis and G. J. Hutchings, *Chem. Soc. Rev.*, 2009, **38**, 2231-2243.
20. N. E. Motl, E. Ewusi-Annan, I. T. Sines, L. Jensen and R. E. Schaak, *J. Phys. Chem. C*, 2010, **114**, 19263-19269.
21. L. Shi, A. Wang, Y. Huang, X. Chen, J. J. Delgado and T. Zhang, *Eu. J. Inorg. Chem.*, 2012, 2700-2706.
22. Y. Liu and A. R. H. Walker, *Angew. Chem. Int. Ed.*, 2010, **49**, 6781-6785..
23. W. Chen, R. Yu, L. Li, A. Wang, Q. Peng and Y. Li, *Angew. Chem. Int. Ed.*, 2010, **49,** 2917-2921.
24. A. Henkel, A. Jakab, G. Brunklaus and C. Sönnichsen, *J. Phys. Chem. C*, 2009, **113**, 2200-2204.
25. S. E. Lohse and C. J. Murphy, *Chem. Mater.*, 2013, **25**, 1250-1261.
26. S. Chen, S. V. Jenkins, J. Tao, Y. Zhu and J. Chen, *J. Phys. Chem. C*, 2013, **117**, 8924-8932.
27. R. He, Y.-C. Wang, X. Wang, Z. Wang, G. Liu, W. Zhou, L. Wen, Q. Li, X. Wang, X. Chen, J. Zeng and J. G. Hou, *Nat. Commun*. 2014, **5**, 4327..
28. S. Linic, P. Christopher and D. B. Ingram, *Nat. Mater.*, 2011, **10**, 911-921.
29. S. Guo, S. Zhang, X. Sun and S. Sun, *J. Am. Chem. Soc.*, 2011, **133**, 15354-15357.
30. Y. Ding, F. Fan, Z. Tian and Z. L. Wang, *J. Am. Chem. Soc.*, 2010, **132**, 12480-12486.
31. A. I. Frenkel, V. S. Machavariani, A. Rubshtein, Y. Rosenberg, A. Voronel and E. A. Stern, *Phys. Rev. B*, 2000, **62**, 9364-9371.
32. T. Shibata, B. A. Bunker, Z. Zhang, D. Meisel, C. F. Vardeman and J. D. Gezelter, *J. Am. Chem. Soc.*, 2002, **124**, 11989-11996.
33. T. K. Sau and A. L. Rogach, *Adv. Mater.*, 2010, **22**, 1781-1804.

34. S. Thota, S. Chen, Y. Zhou, Y. Zhang, S. Zou and J. Zhao, *Nanoscale*, 2015, 7, 14652-14658.
35. X. Xia, Y. Wang, A. Ruditskiy and Y. Xia, *Adv. Mater.*, 2013, **25**, 6313-6333..
36. C. Chen, Y. Kang, Z. Huo, Z. Zhu, W. Huang, H. L. Xin, J. D. Snyder, D. Li, J. A. Herron, M. Mavrikakis, M. Chi, K. L. More, Y. Li, N. M. Markovic, G. A. Somorjai, P. Yang and V. R. Stamenkovic, *Science*, 2014, **343**, 1339-1343.
37. E. González, J. Arbiol and V. F. Puntes, *Science*, 2011, **334**, 1377-1380.
38. B. Goris, L. Polavarapu, S. Bals, G. Van Tendeloo and L. M. Liz-Marzán, *Nano Lett.*, 2014, **14**, 3220-3226.
39. M. H. Oh, T. Yu, S.-H. Yu, B. Lim, K.-T. Ko, M.-G. Willinger, D.-H. Seo, B. H. Kim, M. G. Cho, J.-H. Park, K. Kang, Y.-E. Sung, N. Pinna and T. Hyeon, *Science*, 2013, **340**, 964-968.
40. Y. Xia, W. Li, C. M. Cobley, J. Chen, X. Xia, Q. Zhang, M. Yang, E. C. Cho and P. K. Brown, *Acc. Chem. Res.*, 2011, **44**, 914-924.
41. Y. Yin, R. M. Rioux, C. K. Erdonmez, S. Hughes, G. A. Somorjai and A. P. Alivisatos, *Science*, 2004, **304**, 711-714.
42. S. Thota, Y. Zhou, S. Chen, S. Zou and J. Zhao, *Nanoscale*, 2017, DOI: 10.1039/C7NR00917H.
43. S. Thota, S. Chen and J. Zhao, *Chem. Commun.*, 2016, 52, 5593-5596.
44. U. Banin, Y. Ben-Shahar and K. Vinokurov, *Chem. Mater.*, 2014, **26**, 97-110.

Chapter 2. Structural Defects Induced Peak Splitting in Gold-Copper Bimetallic Nanorods during Growth by Single Particle Spectroscopy

2.1 Introduction

Bimetallic nanoparticles (NPs) often exhibit highly tunable electric, magnetic, optical and catalytic properties due to the synergetic interaction between the two metals[1-6], which are very different from those of the individual components. These unique features make them promising materials in many fields including electronics, biological, and energy applications[7-11]. Currently, many efforts have been made to synthesize bimetallic NPs with controlled distribution and morphology of individual components, in order to obtain desired properties[12, 13]. However, combining two components in one structure still present synthetic challenges, because it is difficult to synchronously control the nucleation and growth of two different metals due to their distinct kinetic and thermodynamic characteristics under the same reaction conditions[14]. Moreover, different lattice parameters of the two metals pose inherent difficulties in the synthesis and lead to structural defects in bimetallic NPs[15, 16].

Over the past two decades, a variety of bimetallic structures have been generated such as core@shell[17, 18], heterostructure[13, 19], and alloyed NPs[20]. In bimetallic alloy NPs, structural instabilities/defects are commonly observed during the alloy process[21]. The defects likely arise from lattice strain created by the mismatch of lattice parameters when combining the two metals. For example, in Au-Pd[22] and Au-Cu[23] alloy NPs, lattice strain builds up due to different atomic radii, leading to defects in the structure. Even in systems

like Au-Ag[24] alloy NPs, where the lattice constants are similar, vacancy sites at bimetallic interface before alloying evolve to the surface in alloying process, resulting in defects formation because of the difference in the lattice energy of the two metals. Detailed studies of these structural defects at the atomic level will help to overcome the synthetic challenges.

To reveal the structural defects, single particle methods are preferred, due to the inevitable structural heterogeneity in NP synthesis[25, 26]. Structures of single NPs are often directly measured by high-resolution transmission electron microscopy (HRTEM)[27-29]. An alternative, indirect single particle approach is dark field scattering. The scattering of metal NPs resulted from the collective oscillation of electrons induced by electromagnetic field, known as LSPR (localized surface plasmon resonance). Because the scattering of single metallic NPs is extremely sensitive to their geometry and composition[30-32], dark field scattering is suitable to monitor small structural changes during NP synthesis. For examples, atomic level changes in Au nanorods[33] or Ag nanospheres[34] during reactions have been detected with dark field scattering. Recently, reported new approach, scanning probe block copolymer lithography (SPBCL)[35, 36] for synthesizing multimetallic nanoparticles, could provide an excellent opportunity to study the detailed in-situ single particle growth process when combined with dark filed scattering technique.

In this work, we apply the simple and non-destructive dark-field scattering spectroscopy technique and electrodynamics simulations to investigate the structure and composition change of single Au-Cu alloy nanorod during synthesis, in conjunction with traditional

ensemble UV-Vis spectroscopy, X-ray Diffraction (XRD), and high angle annular dark field scanning transmission electron microscopy (HAADF-STEM) methods. The single particle scattering spectra of NPs acquired at varying reaction times display dramatically different spectral patterns from the corresponding ensemble UV-Vis spectra. Together with electrodynamics simulations, the single particle scattering study showed that the asymmetric elemental distribution and shape of the nanorods at earlier growth stage lead to split in the scattering peak of the nanorods. More importantly, small geometric defects in the nanorods composed of only several atomic layers dramatically varied the scattering spectral pattern of single nanorods. The atomic level defects in the nanorods revealed by the spectroscopy technique provide valuable information to the understanding of bimetallic NP growth.

2.2 Experimental Section

2.2.1 Chemicals

Gold (III) chloride trihydrate, copper (II) acetyl acetonate (97%), octadecylamine (90%), oleylamine (70%) were purchased from sigma Aldrich and used without any further purification. Tetradecylamine (95%) was obtained from TCI and used as received.

2.2.2 Synthesis of Au-Cu Bimetallic Nanorods

The gold copper bimetallic nanorods were synthesized following a method reported by Chen et al[37] with some modifications. Tetradecylamine (10 mmol, 2.1341 g), octadecylamine (10mmol, 2.6951 g) and gold (III) chloride trihydrate (0.05 mmol, 19.7 mg) were loaded into a flask under nitrogen protection at 160° C to form gold seeds. The

reaction temperature was increased to 180° C and copper (II) acetyl acetonate in 1 mL olelyamine was injected. The solution mixture was maintained at 180° C and samples were collected at different times (2, 5, 10 and 20 minutes) during the growth. The collected samples were cooled to 150° C and toluene was added, followed by centrifugation for 2 minutes (3300 rpm). They were dispersed in nonpolar solvents such as toluene and hexane and used for further characterization.

2.2.3 Dark Field Scattering

The collected bimetallic NP solution was highly diluted in toluene and drop coated onto a precleaned No.1 cover glass (Fisher Scientific). The sample was allowed to air dry for a few minutes and was mounted onto a Nikon Ti-u microscope with halogen lamp as unpolarized illumination source for optical studies. Dark field condenser (NA 0.85) was adjusted to focus at the specimen plane. A 100X NA 0.8 objective (variable NA 0.8-1.3) was used to collect the light scattered only from the sample. The collected signal was directed onto the entrance slit of a spectrograph (Isoplane SCT 320, Princeton Instruments) equipped with a CCD camera (PIXIS 1024 BR, Princeton Instruments). The obtained scattering spectra from the single particles were corrected by subtracting and dividing the background, collected from a nearby region without any particles.

2.2.4 Instrumentation

UV-Vis spectrometer (Cary 60, Agilent technologies) was used to measure the extinction spectra of the NPs. A Rigaku ultima IV power X-ray Diffractometer with Cu Kα radiation operated at a tube voltage of 40 KV and current of 44mA was used to obtain XRD patterns. TEM images were captured using a Tecnai T-12 operated at 120 KV.

HAADF-STEM image was obtained using JEOL 2010 microscope at an accelerating voltage of 200 KV.

2.2.5 Computational Methods

The discrete dipole approximation (DDA) method is used in the calculations[38]. The DDA method is a finite element method in which the target particle is divided into N polarizable cubes. The interactions between cubes are treated using dipole approximation. The method is accurate as long as the cube grid length is small enough. In the calculations, we used a grid length of 0.25 nm, which is close to the van der Waals diameter of gold and copper atoms for the convergence of the calculations. The dielectric constants of gold and copper are obtained from Palik's handbook[39]. The dielectric constants of the alloy are calculated by averaging dielectric constants of the two metals over their volumes. All the calculations are based on classical electrodynamics theory.

2.3 Results and Discussion

2.3.1 Structure and Composition of the Nanoparticles

To monitor the Au-Cu nanorod formation, we collected aliquots at 2, 5, 10, 20 minutes after the injection of Cu precursors. Figure 2.1A−1E show the STEM characterization of the products acquired. At the initial stage, 10 nm Au seeds were formed, as shown in Figure 2.1A. After injection of Cu precursors into the seed solution, quasi-nanorods of 18.2±1.6 nm in length are formed at 2 minutes reaction (Figure 2.1B) and grew into regular nanorod shape of 27.3±2.7 nm in length by 5 minutes (Figure 2.1C). And finally 36.5±4.1 nm long Au-Cu nanorods were obtained after 20 minutes of reaction (Figure

2.1E) and large area TEM shown in Figure 2.2. Different contrasts in STEM images clearly indicatedthe composition evolution process from bright spherical Au seeds to Au-Cu alloy nanorods. XRD results also demonstrated the composition transformation of the NPs via fcc Au phase to $AuCu_3$ phase (Figure 2.1F). In the XRD pattern of Au seeds (black line), three typical peaks were indexed as Au fcc phase (JCPDS: 04-0784). After the reaction of Au seeds with Cu precursor for 2 minutes, Au rich multiple fcc phases were formed as indicted by its broad XRD pattern (red line). For the 5-minute sample, the XRD pattern shifted towards Cu (JCPDS: 04-0836) rich multiple fcc phases (blue line).

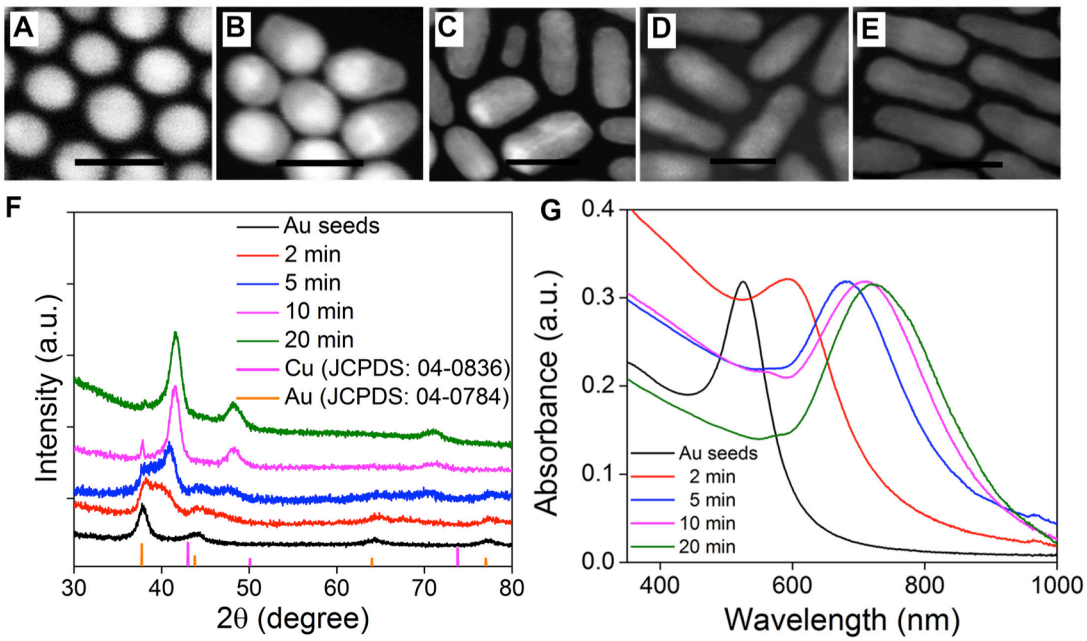

Figure 2.1. STEM images of samples: (A) Au seeds, and aliquots acquired at different reaction times after the injection of Cu precursors (B) 2 minutes, (C) 5 minutes, (D) 10 minutes, and (E) 20 minutes; (F) their corresponding XRD patterns and (G) UV-Vis-NIR spectra of the samples. All scale bars = 20 nm.

As the reaction proceeded to 10 minutes, the broad peaks in the XRD patterns of the 2- and 5-minute samples became narrow, indicating multiple phases turned into a single C

rich phase (pink line). After 20 minutes of reaction, pure $AuCu_3$ phase (JCPDS: 35-1357) of samples was observed, which is consistent with the STEM analysis. The corresponding UV-Vis-NIR spectra of the samples showed a red shift in the peak from 524 nm (Au

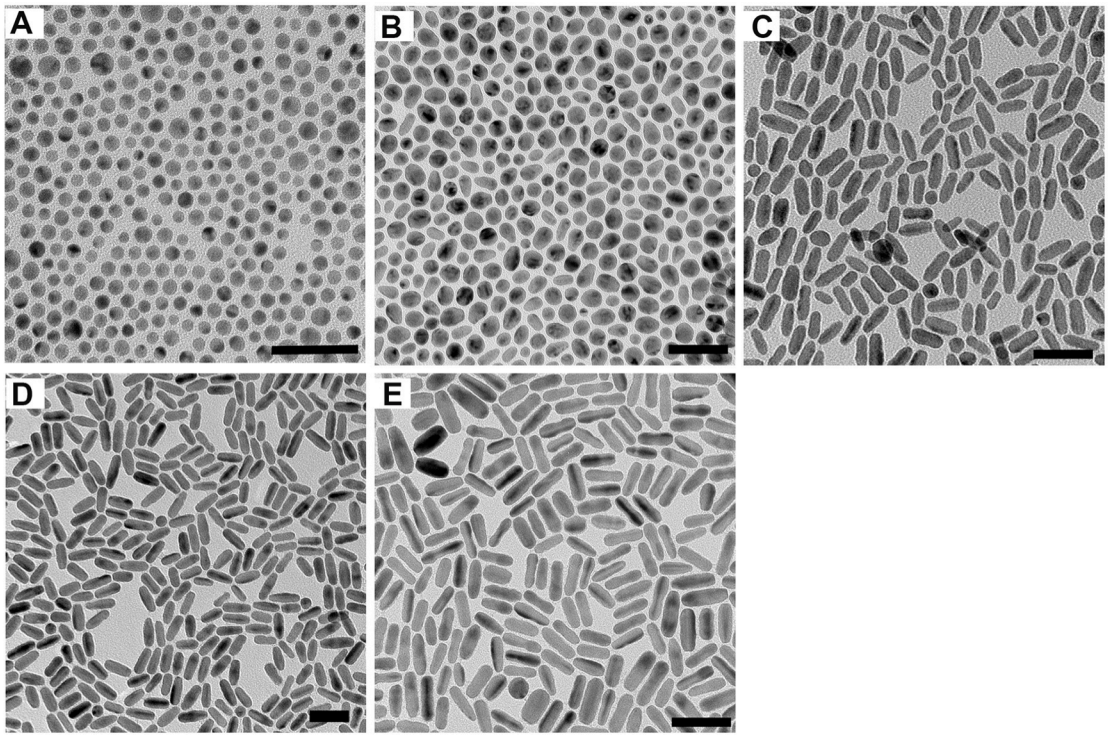

Figure 2.2 TEM images of the samples (A) Au seeds, and aliquots acquired at different reaction times after injection of copper precursor (B) 2 minutes (C) 5 minutes (D) 10 minutes and (E) 20 minutes. Scale bar = 50 nm.

seeds) to 722 nm ($AuCu_3$ nanorods), as shown in Figure 2.1G. The structural and composition changes in the Au-Cu nanorods growth process are consistent with previous studies[37]. However, the detailed structural change at the single particle level during the growth process cannot be easily resolved from these methods.

2.3.2 Single Particle Scattering Spectroscopy

Conventional optical methods measure the average signal from a large number of NPs,

which only disclose macroscopic information. In order to look into the reaction at the single NP level, 100-120 NPs from each sample collected at 2, 5, 10 and 20 minutes were analyzed by dark field scattering spectroscopy. Interestingly, the single NPs displayed

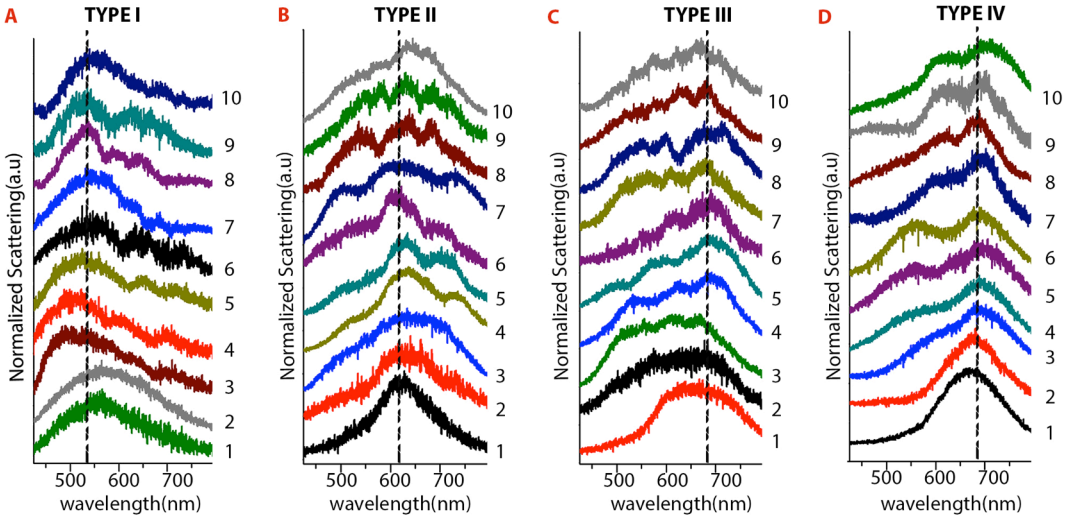

Figure 2.3 Single nanoparticle dark-field scattering spectra of Au-Cu alloy nanoparticles. The samples were acquired at different reaction times after injecting the copper precursors. (A) spectral type I contains nanoparticles from 2 minutes reaction, (B) spectral type II contains nanoparticles from 2 and 5 minutes reaction, (C) spectral type III contains nanoparticles from 5 and 10 minutes reaction and (D) spectral type IV contains nanoparticles from 10 and 20 minutes reaction.

distinct spectral features different from the ensemble and also from each other, especially in the peak patterns. The NPs obtained from different reaction times were broadly classified into four types as shown in Figure 2.3 based on the scattering maximum of the major peak. Ten spectra, from each type were selected randomly from different regions on the glass substrate to represent all major spectral trends observed, as shown in Figure 2.3(A-D). Nanoparticles with the major peak around 540 nm, 620 nm and 680 nm were classified as type I, II and III, respectively. All the NPs of the three spectral types

were obtained from 2, 5 and 10-minute samples. The continuous red shift in the major peak clearly demonstrates the transformation of the NP shape from spherical Au seeds into Au-Cu alloy rods, after addition of the Cu precursor. Quite surprisingly, very few NPs of these types (I, II, III) have scattering spectra with a single peak (Figure 2.3A-C, spectra 1-2). Instead, majority population showed multiple peak patterns (Figure 2.3A-C, spectra 3-10). The multiple peak features are clearly resolved into three peak patterns for some NPs (4-8 of 2.3A-C). The peaks are around 550±7 nm, 615±13 nm and 693±16 nm with varying relative intensities. The multiple peak patterns are different from what has been found in the scattering spectra of perfect single Au nanorods, where only a single peak from the longitudinal mode of the rods was dominant[40, 41]. The NPs showing a major peak around 690-700 nm, with an additional peak to the blue of the main peak are considered type IV, as shown in Figure 2.3D. The number of scattering peaks of single NPs decreases as the reaction time proceeds. The reaction was completed after 20 minutes as no further changes in the spectral features was observed.

The distribution of the NPs into varying growth stages from the 2,5,10 and 20 minute-samples are listed in Table 1. As Table 1 shows, the samples acquired at the same reaction time contain NPs in two growth stages (except for the 20-minute sample). In addition, the fraction of NPs in a certain growth stage varies significantly with growth time. For example, in the 2-minute sample, 71% of the studied NPs were in growth stage I, while 29% were in growth stage II. In contrast, in the 5-minute sample, none of the observed NPs were in growth stage I; only 38% were in growth stage II and 62% were in growth stage III. The quantitative analysis of the NP distribution in varying growth stages showed that as the reaction progressed, more of the NPs were found to be in later growth

	Type I	Type II	Type III	Type IV
2 minutes	71%	29%		
5 minutes		38%	62%	
10 minutes			26%	74%
20 minutes				100%

Table 2.1. Population distribution of nanoparticles of different spectral types

stages and they all converted to the final product, eventually. The single particle measurements revealed that NPs acquired at same reaction times were not necessarily in the same growth stages, showing the variation in the reaction kinetics at the single particle level.

2.3.3 Structural Defects Revealed by Single Particle Scattering Patterns

The spectral changes of the NPs acquired at different reaction times are associated with the structural and composition change of the NPs during the reaction. The STEM study showed that quasi-rod structure was formed at the beginning of Au-Cu nanorod growth. In order to understand the origin of the scattering peaks of these quasi-rods, discrete dipole approximation (DDA) calculations[38] were performed. From Figure 2.4B, the Au seed preserves its spherical shape, while Cu is deposited on one side of the Au seed. Therefore, in the theoretical modeling, we constructed a NP of similar structure with an Au sphere of 10 nm diameter being on one side, and a cone like Cu structure on the other side (as seen in Figure 2.4A). The calculated spectra of the transverse mode show one resonance peak at the wavelength close to that of the Au seed, ~ 520 nm. On the contrary, the longitudinal mode displays two resonance peaks as shown in Figure 2.4C. The dipole

peak of the longitudinal mode is at ~ 593 nm and a quadrupole mode appears at ~ 530 nm as shown in Figure 2.5. The appearance of the quadrupole mode in such a short rod is due

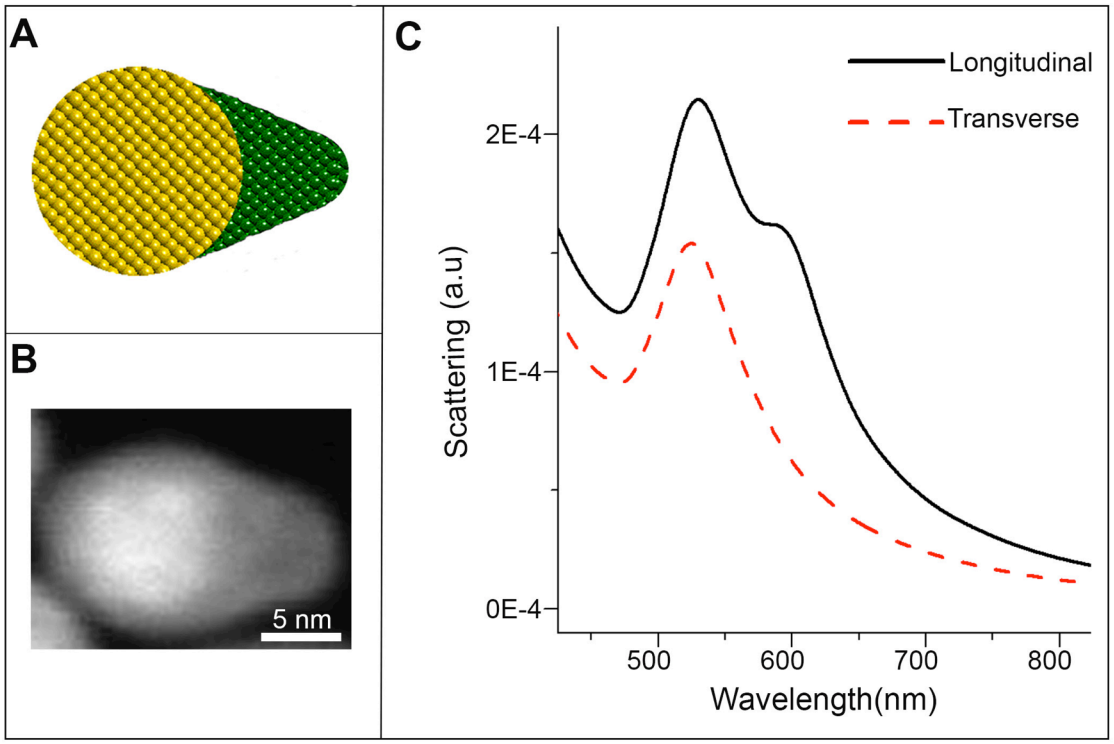

Figure 2.4. (A) Scheme of a quasi-rod particle. An Au sphere of 10 nm diameter is on one side (yellow) and cone-like Cu particle with d = 2 nm is on the other side (green). (B) STEM image of a quasi-rod. (C) Scattering spectra of the transverse mode (red) with a peak at 520 nm and longitudinal mode (black) mode with a peak at 530 nm and a shoulder at 593 nm, of the quasi-rod.

to the asymmetric shape of the quasi rod. The field distributions in the quasi-rod as shown in Figure 2.5 indicate the quadrupole mode might be an anti-bonding mode of coupling between the Au and Cu NPs. Notice that the scattering efficiency of the transverse mode is much smaller than that of the longitudinal mode; the longitudinal mode dominates the scattering spectrum. When varying the size of the Cu-cone in the quasi-rod, the relative intensity of the peaks changes while the peak position is

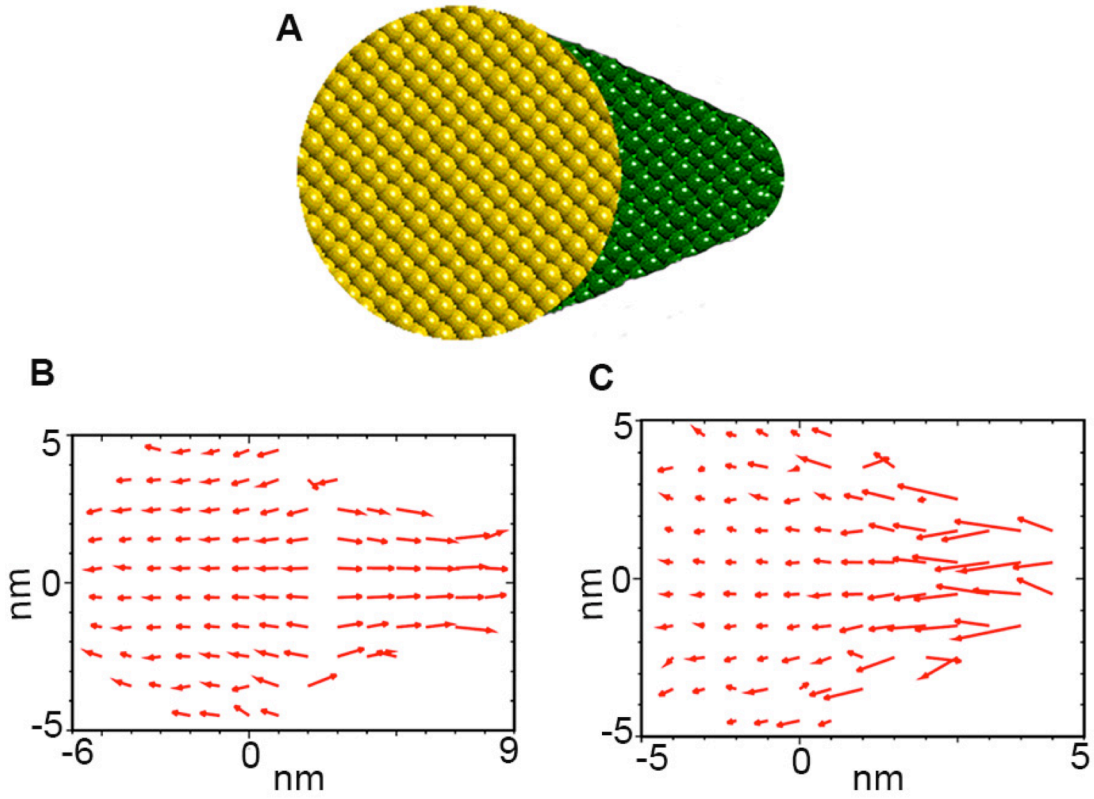

Figure 2.5. Induced polarizations in a quasi-rod particle. The amplitude of each vector is the modulus of the complex polarization. (A) Scheme of quasi-rod. (B) Induced polarization at 540 nm. The distribution of the polarizations shows that it is the quadrupole mode. (C) Induced polarization at 595 nm. The distribution of the polarizations shows that it is the dipole mode.

maintained as shown Figure 2.6. The low intensity peaks at wavelengths over 600 nm shown in NPs of spectral type I may be from the longitudinal dipole peak of longer quasi-rods. In addition, if small structural defects exist in the rods (as discussed below), the dipole peak will further split, resulting in multiple weak peaks above 600 nm. Overall, the asymmetric Au-Cu rod has a main peak at ~ 540 nm and a shoulder at ~ 600 nm, consistent with the observed scattering spectra in type I.

After the Au-Cu quasi-rods were formed, the alloying process continued to proceed and

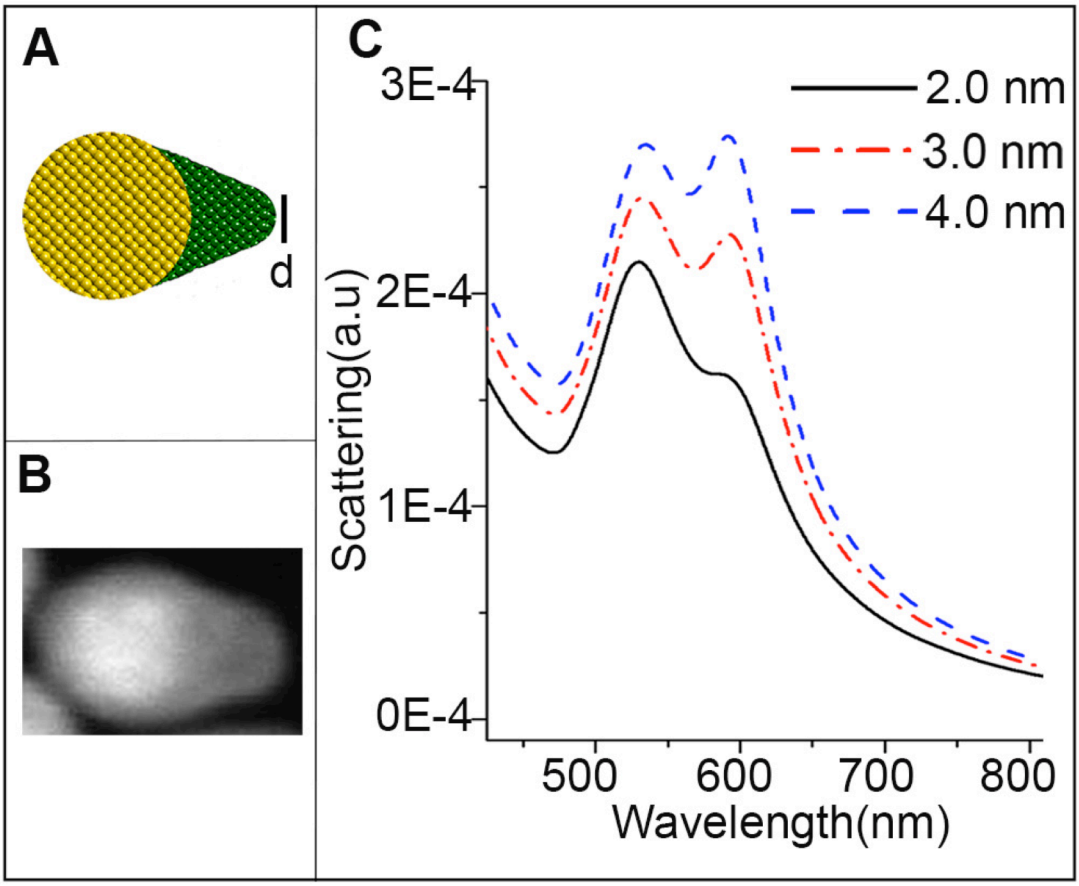

Figure 2.6. (A) Scheme of the quasi-rod. Yellow represents Au and green represents Cu. (B) STEM image of a representative quasi-rod particle. (C) Scattering spectra of the quasi rod when it is excited longitudinally, with tip diameters of 2 nm (black) 3nm (red) and 4 nm (blue). The Au "head" diameter is fixed at 10 nm. All the scattering spectra show two peaks at 540 nm and 595 nm

the NPs grew into regular rod shape. As mentioned above, only one scattering peak was found in single Au nanorods[40, 41], whereas in our experimental study of single Au-Cu alloy nanorods, multiple scattering peaks were observed. In the calculations, we firstly examined the effect of the change in the Au/Cu ratio and in the distribution of Au and Cu

atoms in the NPs during growth. Specifically, since the composition of the nanorods changes gradually during the reaction, we varied the fraction of Au and Cu in a nanorod

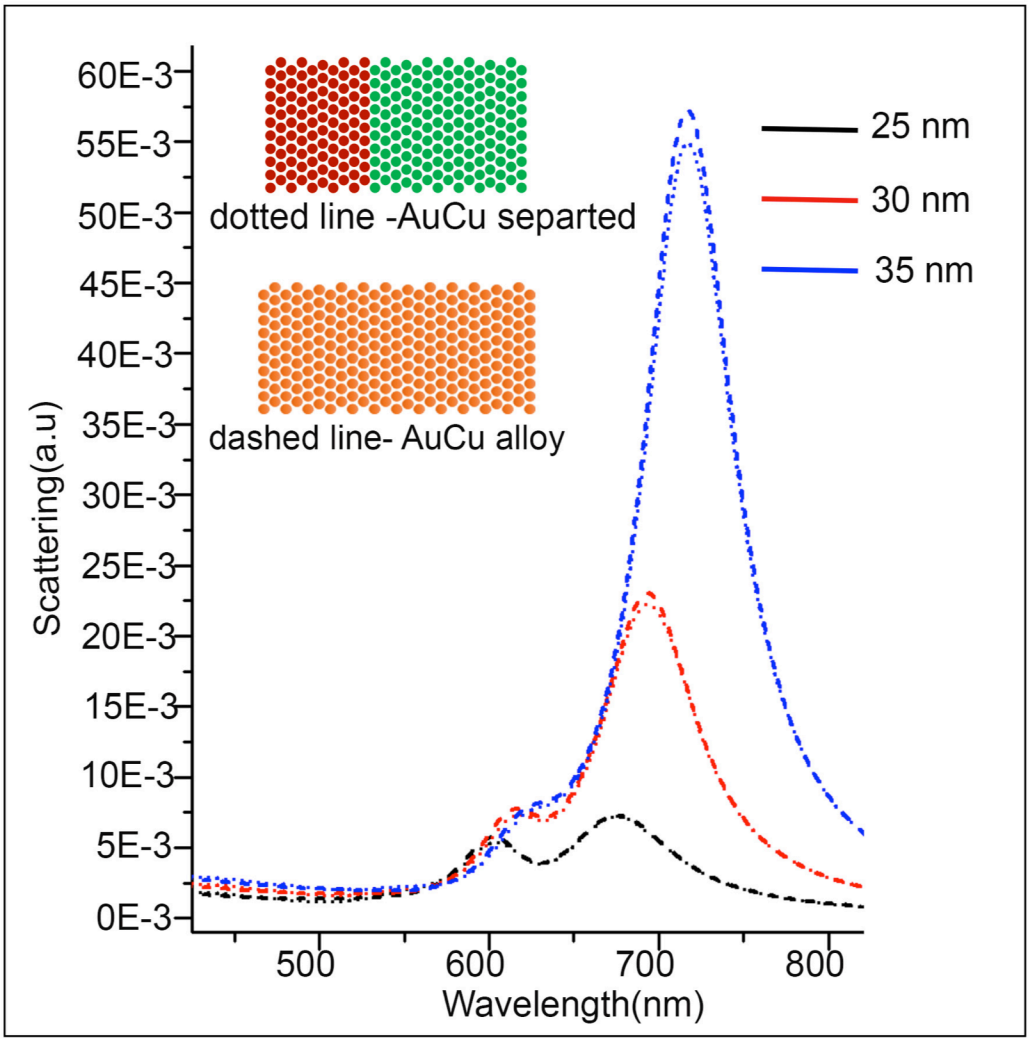

Figure 2.7. Schemes and calculated single particle scattering spectra of nanorods where Au and Cu were separated (dotted lines) or uniformly mixed with a 1:3 ratio (dashed lines). The lengths of the nanorods are 25 nm (black), 30 nm (red) and blue (35 nm). The calculated spectra are similar, indicating that composition has no significant effect on single particle scattering because the dielectric functions of gold and copper are similar.

using their respective dielectric constants for their occupied volumes. From the

calculations, we observed a change in the scattering peak position when varying the NP composition, but not the split peak pattern. We also compared the spectra when the Au and Cu are well mixed (alloyed) or separated for a given composition and found only slight difference in the spectra as seen in Figure 2.7. This is because that Au and Cu have similar dielectric functions above 550 nm where the resonance wavelengths are located [39, 42]. In the calculations, neither the composition nor the atom distribution in the NPs leads to multiple peaks in the scattering spectra, observed experimentally. Secondly, we considered the effect of glass substrate since the split peak was predicted when a spherical particle was located on a substrate with index of refraction greater than 2[43]. The index of refraction of the glass substrate used in the experiment is about 1.5. When the substrate is included in the calculations, it only red shifts the resonance peak without changing the spectral pattern. Therefore, the substrate effect was treated with effective medium theory[44, 45] in the following simulations. We also examined the change in the size of the NPs and aspect ratios; none of them would produce scattering peaks as shown in the experiments.

We notice that in the alloy NP synthesis, it is hard to form defect-free crystals because the two metals in their pure state have different properties such as atom size, reduction potential, lattice constant and surface energies. These defects may consist of only a few atoms, not easily be detected in normal TEM studies. Since the single particle optical technique is extremely sensitive to the NP geometry, atomic level defects in the Au-Cu nanorods could cause unusual scattering patterns.

To examine the effect of geometric defects in the nanorods on their optical spectra, we calculated the scattering spectra of a 20 nm long Au-Cu alloy nanorod without and with

different degrees of defect. To account for the unpolarized excitation light used in the

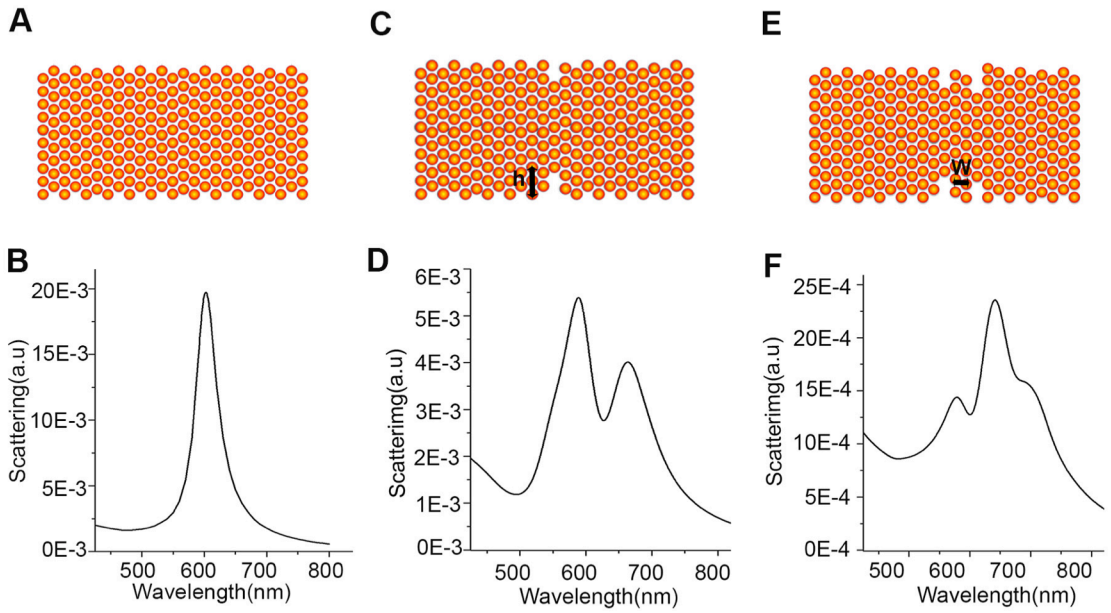

Figure 2.8. Schemes (A, C and E) and calculated scattering spectra (B, D, and F) of an Au-Cu alloy rod without and with defects. (A-B) Scheme and corresponding scattering spectrum of a rod without defect. (C-D) Scheme and corresponding scattering spectrum of a rod with one well-like defect where the width of the defect is 0.5 nm and the height (h) is 1.25 nm. (E-F) Scheme and corresponding scattering spectrum of a rod with two well-like defects where the defects are 1.5 nm and 1.0 nm in height, and 0.5 nm in width. The defects are separated by a distance (w) of 1.0 nm.

experiments, the scattering spectra presented in Figures 2.8 and 2.9 are averaged over different polarizations. For a defect free nanorod as shown in Figure 2.8A, only a single scattering peak from longitudinal mode of the rod was observed in the calculated spectrum (as shown in Figure 2.8B). When one well-like defect or two well-shaped defects next to each other were introduced to the rods, peak splitting was observed in the scattering spectra. HRTEM images are available in Figure 2.10, showing the kink defects on the surface of the nanorods. For an Au-Cu alloy nanorod with one 0.5 nm wide well like defect (as shown in Figure 2.8C), its scattering spectrum is extremely sensitive to

the well depth. A change of the well depth from 0.75 to 1.0 nm, which corresponds to

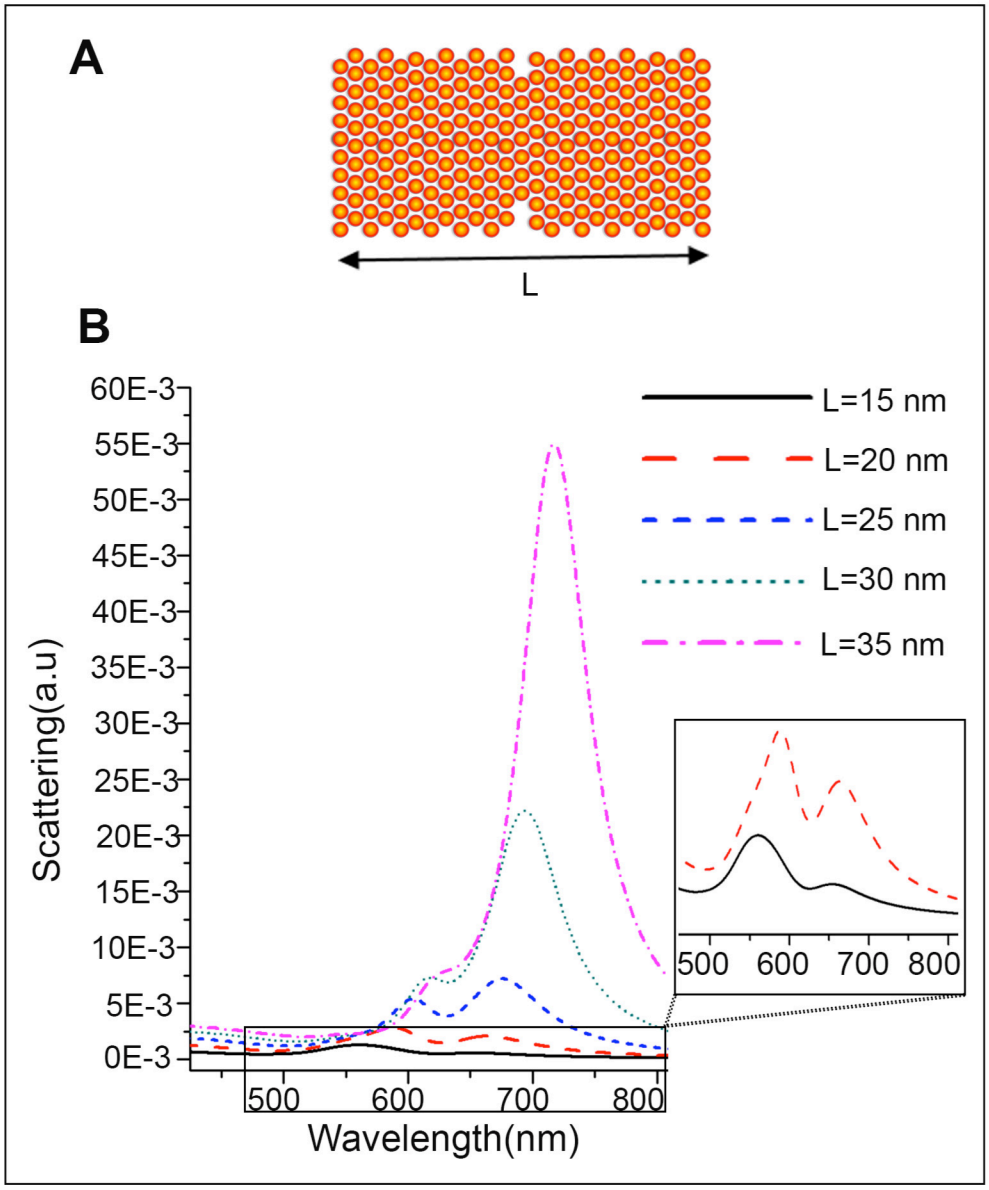

Figure 2.9. (A) Schematic illustration of a rod with a well-like defect and (B) scattering spectra for the rods of varying lengths. Black: L = 15 nm, Red: L = 20 nm, Blue: L = 25 nm, Sea Green: L = 30 nm, Pink: L = 35 nm.

only one layer of atoms, leads to a split in single longitudinal dipole peak into a dipole peak and an octopole peak (as seen in Figure 2.8D, Figure 2.11 and 2.12). The defect

separates the nanorod into two parts, and the plasmonic coupling between them promotes the generation of octopole peak in such a short rod. For a nanorod with two well-shaped

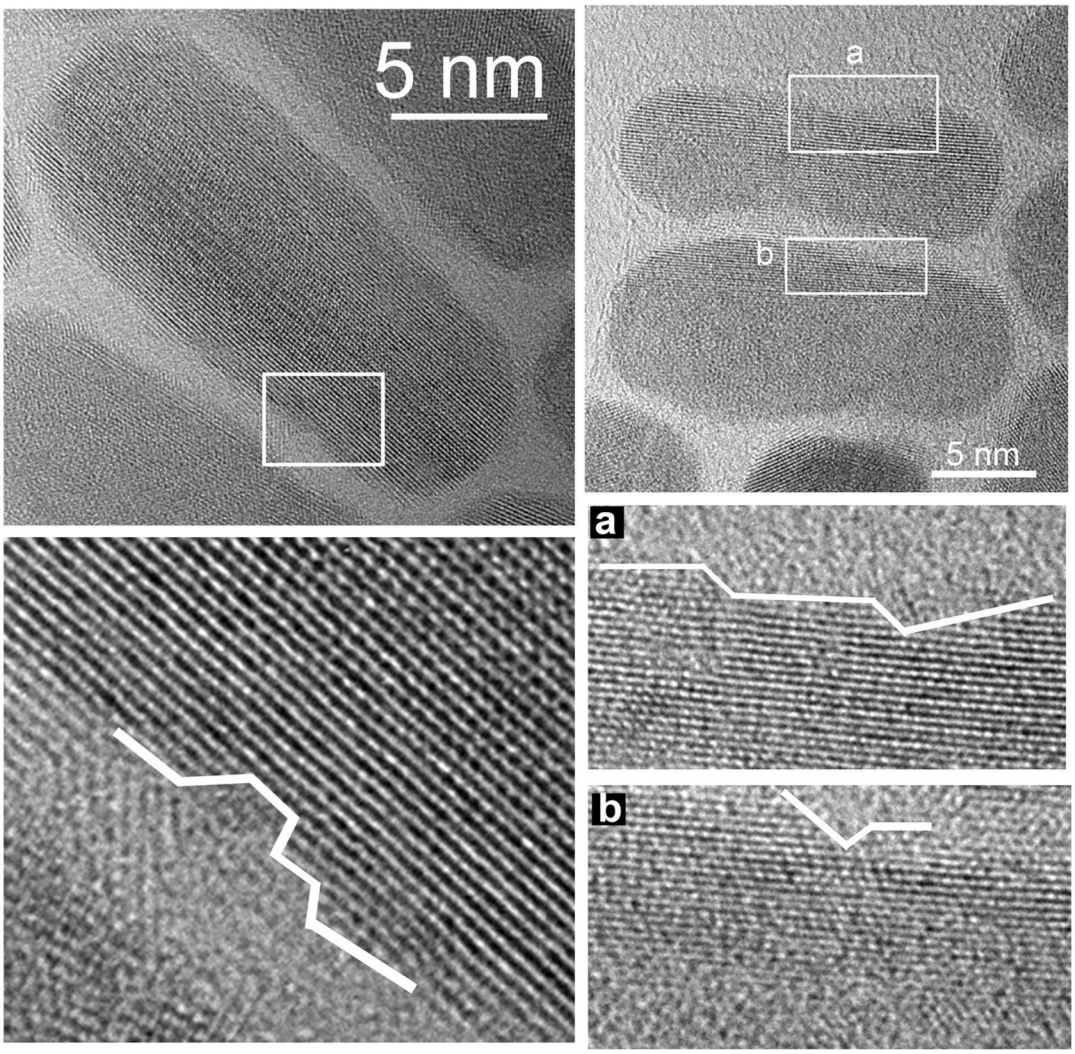

Figure 2.10. HRTEM images of rods with defects. Defects of different shapes and sizes are highlighted in the images. For example (a) and (b) show rods with two defects adjacent to each other and a single defect respectively.

defects arranged close to each other (as shown in Figure 2.8E), the number of the scattering peaks of the nanorod becomes three. The peak at the longest wavelength corresponds to the dipole mode while the one at the shortest wavelength corresponds to the octopole peak. The peak in between the two is a mixture of the dipole

and octopole modes and can hardly be classified. We also attempted structures with

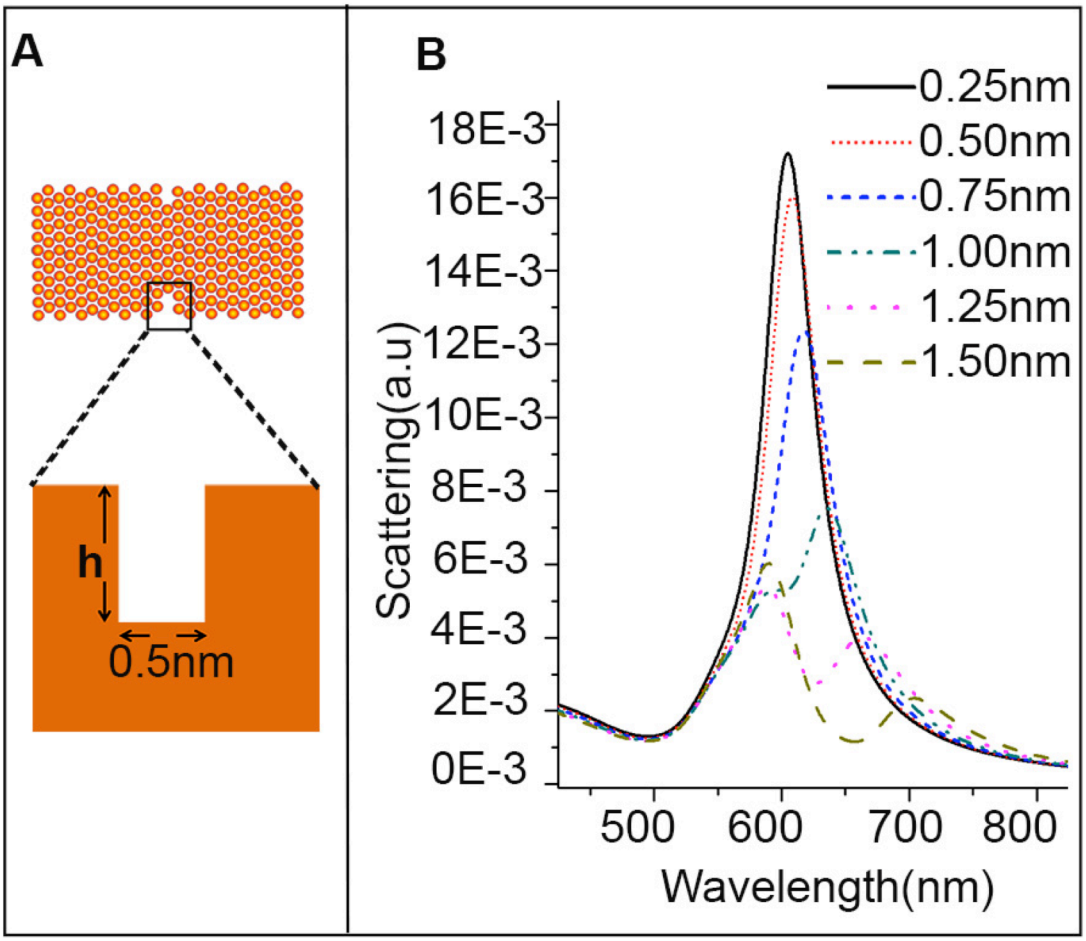

Figure 2.11. (A) Scheme of an Au-Cu alloy nanorod with defect. The diameter of the rod = 10 nm and the length = 20 nm. (B) Scattering spectra of the rod with defect of width 0.5 nm and varying height h = 0.25 nm (black), 0.50 nm (red), 0.75 nm (blue), 1.00 nm (sea green), 1.25 nm (pink) and 1.50 nm (light green). Defect causes the splitting in the longitudinal mode of the rod as its depth increases from 0.75 nm to 1 nm. The splitting results in two peaks, one around 600 nm and one greater than 650 nm.

defects separated from each other, with similar well defects but different depths, and also structures with asymmetric defects. Multiple peak patterns in the scattering spectra were obtained in each case and splitting was more obvious (see Figure 2.13 and 2.14). The

evidence provided by HRTEM and DDA modeling suggests that small structural defects

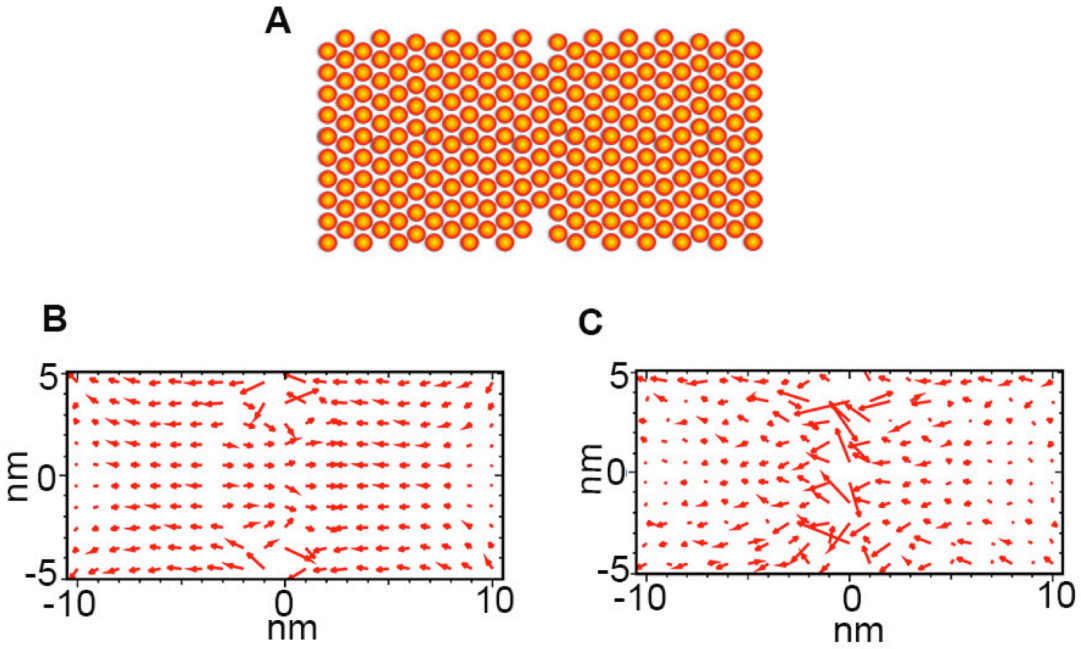

Figure 2.12. Induced polarizations in the Au-Cu alloy nanorod with a defect. (A) Scheme of the nanorod. The diameter of the rod = 10 nm and the length = 20 nm. The depth of the defect = 1 nm. (B) Induced polarization at 595 nm. The distribution of the polarizations shows that it is the octopole mode. (C) Induced polarization at 665 nm. The distribution of the polarizations shows that it is the dipole mode.

in the nanorods could induce peak splitting. A correlated structural and optical study[46-48] of single Au-Cu nanorod will be pursued in the future to further enhance the study. As the reaction proceeds, the number of defects decreases due to the formation of nanorods with higher crystallinity. In the optical study, more NPs with a single or two scattering peaks were observed in the NPs acquired at longer reaction times (type IV), in agreement with the theoretical studies. A control experiment when the nanorods were annealed at 280 ºC after 20 minutes reaction show that 50% of the nanorods possess a single scattering peak, compared to 20% before annealing as shown in representative spectra in

Figure 2.15. A quantitative analysis on the number of particles showing multiple and

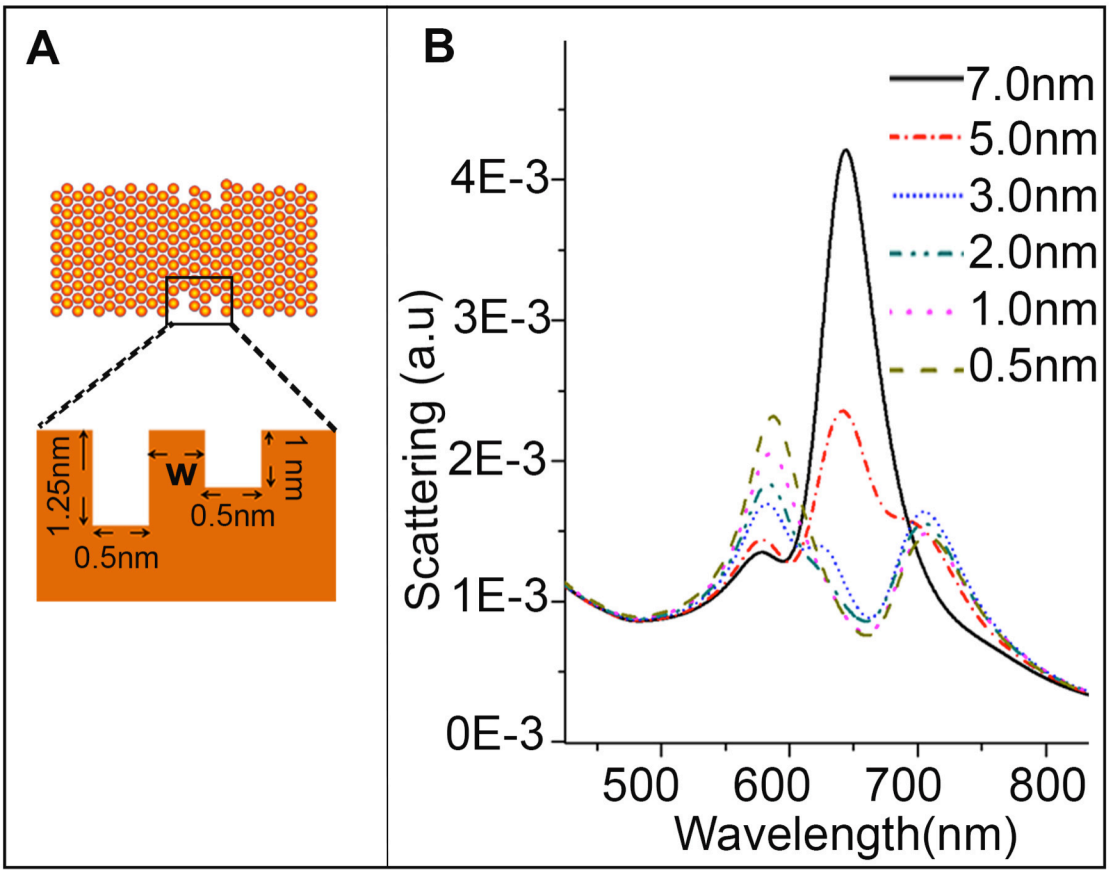

Figure 2.13. (A) Scheme of an Au-Cu alloy nanorod with two defects close to each other. The diameter of the rod = 10 nm and the length = 20 nm. (B) Scattering spectra of the rod with two defects of depth=1.25nm and 1nm, and width of 0.5 nm each separated by *w* = 7.0 nm (black), 5.0 nm (red), 3.0 nm (blue), 2.0 nm(sea green), 1.0 nm (pink) and 0.5 nm (light green). As *w* is reduced from 7 to 5 nm, the scattering spectrum of the rod changes from a two-peak pattern to a three-peak pattern.

single peaks for different samples shows the number of scattering peaks of the nanorods decreases with reaction time as shown in Table 2). This proves the geometric defects are indeed the origin of the multiple peak patterns. With the understanding of the multiple scattering peaks, we also tried to investigate the origin of the red shift in

the main scattering peak with increasing reaction time, which was observed in both the single particle and ensemble measurements. To understand this, in the modeling, we varied the length of the Au-Cu alloy nanorod while keeping a well-like defect of 0.5 nm

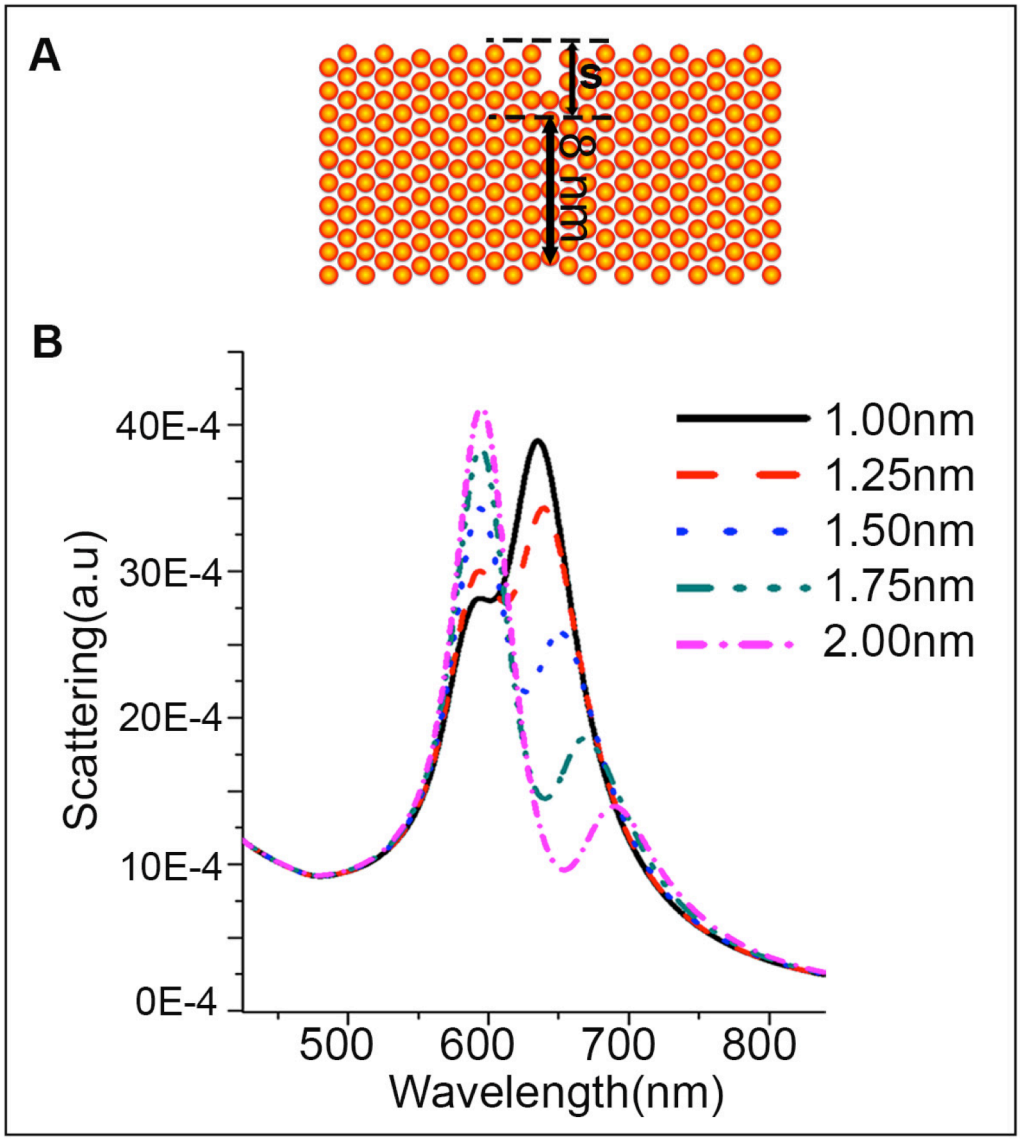

Figure 2.14. (A) Scheme of an Au-Cu alloy nanorod with asymmetric defects. The diameter of the rod = 10 nm and the length = 20 nm. (B) Scattering spectra of the rod obtained by shifting the central disk of width 8 nm, to one side by 0 nm (black), 0.25 nm (red), 0.50 nm (blue), 0.75 nm (sea green), and 1.00 nm (pink) between two defects of 0.5 nm width and 1.0 nm depth.

	Single peak	Two peaks	Multiple peaks (greater than 2 peaks)
Type I	16%	-	84%
Type II	11%	-	89%
Type III	2%	-	98%
Type IV	20%	80%	-
280° C	50%	50%	-

Table 2.2. Population distribution of nanoparticles based on peak patterns

and 1.25 nm in depth (see Figure 2.9A). The calculated spectra (in Figure 2.9B) show

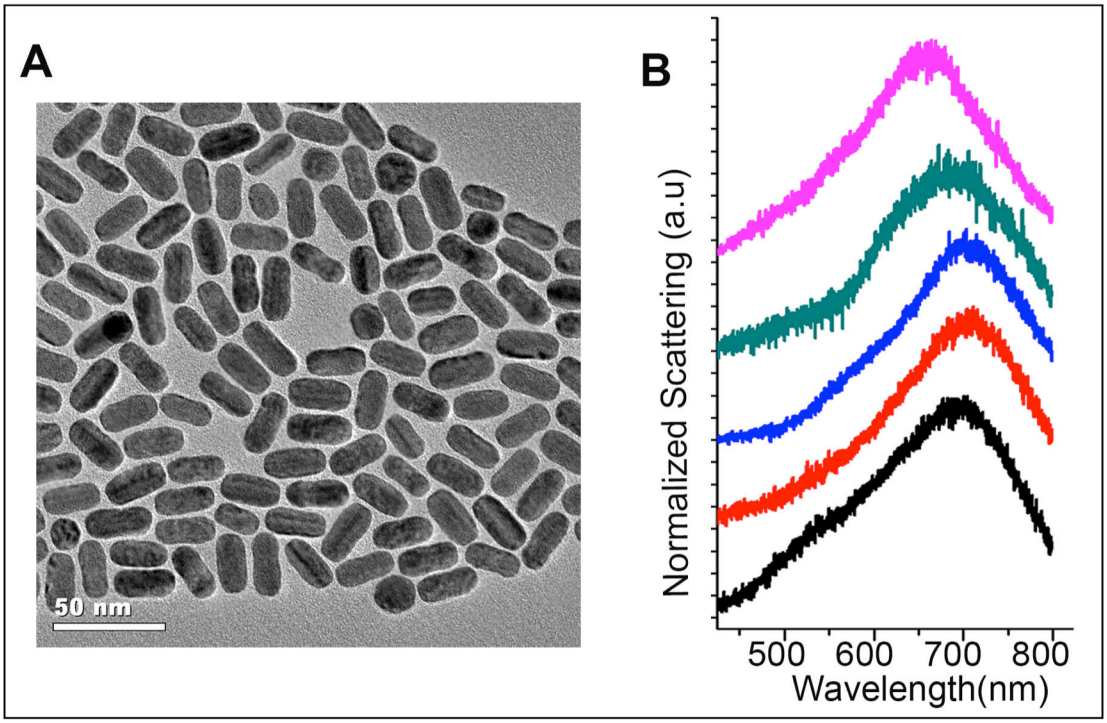

Figure 2.15. (A) TEM image of the annealed nanorods (B) Single nanoparticle dark field scattering spectra of the Au-Cu alloy nanorods annealed at 280° C for 20 minutes. They show only a single scattering peak from the longitudinal mode of the rod, indicating that the defects are reduced.

that the dipole peak of the longitudinal mode red shifts with increasing aspect ratio of the rod, which is expected and consistent with the experimental measurements[49, 50]. The peak intensity of the dipole mode relative to that of the octopole keeps growing which is also in agreement with the measured single particle scattering spectra.

2.3.4 Possible Mechanisms of Defect Formation

The exact mechanism of defect formation is unknown. We propose here two possible reasons. One is due to the alloy process. Bimetallic alloy NP formation involves diffusing and mixing of two metals. In the alloy process, the crystal structures of the bimetallic NP also change. Since the two metals in their pure state have different properties such as atom size, reduction potential, lattice constant, surface energies, it is challenging for them to form perfect crystals. In our study, as discussed previously, the Cu atoms were deposited on one side of the Au seed before Au and Cu diffused into stable alloy phase. In the diffusing process, the vacancy sites at bimetallic interface before alloying evolve to the surface causing defects mostly on the surfaces of the NPs[24]. As the reaction proceeds, the alloy phase becomes stable $AuCu_3$ and the Au-Cu nanorods also get annealed. Therefore, fewer defects were found in the nanorods at later growth stages.

Another possible reason is that there were unreacted gold precursors ($HAuCl_4$) in the solution while Au-Cu alloy NPs were forming. Because the reduction potential of $AuCl_4^-$ /Au (0.99 V vs SHE) is more positive than of $CuCl_2$/Cu (-0.394 V vs SHE), Cu-rich nanorods can serve as a reduction materials for reaction, being oxidized by $HAuCl_4$ according to

$$3Cu(s) + 2HAuCl_4(aq) \rightarrow 3CuCl_2(s) + 2HCl + 2Au(s)$$

Therefore, the unreacted Au precursor can replace Cu atom from the nanorod surface[51, 52], causing structural defects to form in the nanorods. But the concentration of the Au precursor is not high enough to etch or remove large number of Cu atoms from the centre of the rod, which would result in hollow rod structures. In the experimental condition, we believe only the Cu atoms on the surface of the rods could be replaced by Au atoms, possibly the reason why the kinks are formed on the surface. With increasing reaction time, the concentration of unreacted Au precursors was reduced thus less likely to further remove Cu atoms from the nanorod.

2.4 Conclusions

In summary, single particle scattering spectroscopy was applied to study the growth of single Au-Cu alloy nanorod during synthesis. The single particle scattering spectra have multiple scattering peaks induced by small structural defects and asymmetry in the nanorod geometry. We demonstrated that the single particle scattering spectroscopy can reveal structural defects caused by only a few atoms with the aid of DDA simulations, showing the extreme sensitivity of the optical technique to the NP structure. This method can be applied to study microscopic structural changes at single particle level in alloy systems during synthesis, which significantly affects the properties of the alloy NPs, such as their optical and surface catalytic properties.

2.5 Reference

1. M. B. Cortie and A. M. McDonagh, *Chem. Rev*, 2011, **111**, 3713-3735.
2. M. K. Debe, *Nature*, 2012, **486**, 43-51.
3. B. Lim, M. Jiang, P. H. C. Camargo, E. C. Cho, J. Tao, X. Lu, Y. Zhu and Y. Xia, *Science*, 2009, **324**, 1302-1305.
4. M. G. Blaber, M. D. Arnold and M. J. Ford, *J. Phys: Condens. Mat*, 2010, **22**, 143201.
5. A. L. Schmucker, N. Harris, M. J. Banholzer, M. G. Blaber, K. D. Osberg, G. C. Schatz and C. A. Mirkin, *ACS Nano*, 2010, **4**, 5453-5463.
6. T. Krenke, E. Duman, M. Acet, E. F. Wassermann, X. Moya, L. Manosa and A. Planes, *Nat. Mater.*, 2005, **4**, 450-454.
7. D. M. Alonso, S. G. Wettstein and J. A. Dumesic, *Chem. Soc. Rev.*, 2012, 41, 8075-8098.
8. D. Kim, J. Resasco, Y. Yu, A. M. Asiri and P. Yang, *Nat. Commun.*, 2014, **5**. doi: 10.1038/ncomms5948.
9. N. Wang, Y. Han, Y. Xu, C. Gao and X. Cao, *Anal. Chem.*, 2014, **87**, 457-463.
10. S. Guo, S. Zhang, X. Sun and S. Sun, *J. Am. Chem. Soc.*, 2011, 133, 15354-15357.
11. R. He, Y.-C. Wang, X. Wang, Z. Wang, G. Liu, W. Zhou, L. Wen, Q. Li, X. Wang, X. Chen, J. Zeng and J. G. Hou, *Nat. Commun.*, 2014, **5**. doi: 10.1038/ncomms5327.
12. T. K. Sau and A. L. Rogach, *Adv. Mater.*, 2010, **22**, 1781-1804.
13. A. Walther and A. H. Muller, *Chem. Rev.*, 2013, **113**, 5194-5261.
14. D. Wang and Y. Li, *Adv. Mater.*, 2011, **23**, 1044-1060.
15. J. A. Rodriguez and D. W. Goodman, *Science*, 1992, **257**, 897-903.
16. J. Wu, P. Li, Y.-T. Pan, S. Warren, X. Yin and H. Yang, *Chem. Soc. Rev.*, 2012, **41**, 8066-8074.
17. M. Grzelczak, B. Rodríguez-González, J. Pérez-Juste and L. M. Liz-Marzán, *Adv. Mater.*, 2007, **19**, 2262-2266.

18. F. Tao, M. E. Grass, Y. Zhang, D. R. Butcher, J. R. Renzas, Z. Liu, J. Y. Chung, B. S. Mun, M. Salmeron and G. A. Somorjai, *Science*, 2008, **322**, 932-934.
19. Y. Yang, W. Wang, X. Li, W. Chen, N. Fan, C. Zou, X. Chen, X. Xu, L. Zhang and S. Huang, *Chem. Mater.*, 2012, **25**, 34-41.
20. Z. Quan, Y. Wang and J. Fang, *Acc. Chem. Res.*, 2012, **46**, 191-202.
21. W. J. Huang, R. Sun, J. Tao, L. D. Menard, R. G. Nuzzo and J. M. Zuo, *Nat. Mater.*, 2008, **7**, 308-313.
22. Y. Ding, F. Fan, Z. Tian and Z. L. Wang, *J. Am. Chem. Soc.*, 2010, **132**, 12480-12486.
23. A. I. Frenkel, V. S. Machavariani, A. Rubshtein, Y. Rosenberg, A. Voronel and E. A. Stern, *Phys. Rev. B*, 2000, **62**, 9364-9371.
24. T. Shibata, B. A. Bunker, Z. Zhang, D. Meisel, C. F. Vardeman and J. D. Gezelter, *J. Am. Chem. Soc.*, 2002, **124**, 11989-11996.
25. L. Shi, C. Jing, W. Ma, D.-W. Li, J. E. Halls, F. Marken and Y.-T. Long, *Angew. Chem. Intl. Ed.*, 2013, **52**, 6011-6014.
26. P. Chen, X. Zhou, N. M. Andoy, K.-S. Han, E. Choudhary, N. Zou, G. Chen and H. Shen, *Chem. Soc. Rev.*, 2014, **43**, 1107-1117.
27. B. T. Sneed, C. N. Brodsky, C.-H. Kuo, L. K. Lamontagne, Y. Jiang, Y. Wang, F. Tao, W. Huang and C.-K. Tsung, *J. Am. Chem. Soc.*, 2013, **135**, 14691-14700.
28. H. L. Xin, S. Alayoglu, R. Tao, A. Genc, C.-M. Wang, L. Kovarik, E. A. Stach, L.-W. Wang, M. Salmeron, G. A. Somorjai and H. Zheng, *Nano Lett.*, 2014, **14**, 3203-3207.
29. B. T. Sneed, C.-H. Kuo, C. N. Brodsky and C.-K. Tsung, *J. Am. Chem. Soc*, 2012, **134**, 18417-18426.
30. N. J. Halas, S. Lal, W.-S. Chang, S. Link and P. Nordlander, *Chem. Rev.*, 2011, **111**, 3913-3961.
31. V. Giannini, A. I. Fernández-Domínguez, S. C. Heck and S. A. Maier, *Chem. Rev.*, 2011, **111**, 3888-3912.
32. M. A. van Dijk, M. Lippitz and M. Orrit, *Acc. Chem. Res.*, 2005, **38**, 594-601.
33. C. Novo, A. M. Funston and P. Mulvaney, *Nat. Nano.*, 2008, **3**, 598-602.

34. J. G. Smith, Q. Yang and P. K. Jain, *Angew. Chem. Intl. Ed.*, 2014, **53**, 2867-2872.
35. P.-C. Chen, G. Liu, Y. Zhou, K. A. Brown, N. Chernyak, J. L. Hedrick, S. He, Z. Xie, Q.-Y. Lin, V. P. Dravid, S. A. O'Neill-Slawecki and C. A. Mirkin, *JACS.*, 2015, DOI: 10.1021/jacs.5b05139.
36. G. Liu, D. J. Eichelsdoerfer, B. Rasin, Y. Zhou, K. A. Brown, X. Liao and C. A. Mirkin, *PNAS.*, 2013, **110**, 887-891.
37. S. Chen, S. V. Jenkins, J. Tao, Y. Zhu and J. Chen, *J. Phys. Chem. C*, 2013, **117**, 8924-8932.
38. T. B. Draine, *The Astrophys. J.*, 1988, **333**, 848-872.
39. E. D. Palik, *Handbook of optical constants of solids*, Academic Press, Boston, 1988.
40. H. Chen, L. Shao, Q. Li and J. Wang, *Chem. Soc. Rev.*, 2013, **42**, 2679-2724.
41. L. S. Slaughter, Y. Wu, B. A. Willingham, P. Nordlander and S. Link, *ACS Nano*, 2010, **4**, 4657-4666.
42. A. Bansal and S. S. Verma, *AIP Advances*, 2014, **4**, 057104.
43. J. Lermé, C. Bonnet, M. Broyer, E. Cottancin, D. Manchon and M. Pellarin, *J. Phys. Chem. C*, 2013, **117**, 6383-6398.
44. X. Tian, Y. Zhou, S. Thota, S. Zou and J. Zhao, *J Phys. Chem. C*, 2014, **118**, 13801-13808.
45. M. Wang and N. Pan, *Mater. Sci. Eng. R.*, 2008, **63**, 1-30.
46. E. M. Perassi, C. Hrelescu, A. Wisnet, M. Döblinger, C. Scheu, F. Jäckel, E. A. Coronado and J. Feldmann, *ACS Nano*, 2014, **8**, 4395-4402.
47. A. Grubisic, V. Schweikhard, T. A. Baker and D. J. Nesbitt, *ACS Nano*, 2013, **7**, 87-99.
48. Q. Wei, H. Qi, W. Luo, D. Tseng, S. J. Ki, Z. Wan, Z. Göröcs, L. A. Bentolila, T.-T. Wu, R. Sun and A. Ozcan, *ACS Nano*, 2013, **7**, 9147-9155.
49. S. Link and M. A. El-Sayed, *J. Phys. Chem. B*, 1999, **103**, 8410-8426.
50. L. Vigderman and E. R. Zubarev, *Chem. Mater.*, 2013, **25**, 1450-1457.
51. Y. Sun and Y. Xia, *Science* 2002, **298**, 2176-2179.

52. C. W. Yen, M. A. Mahmoud and M. A. El-Sayed, *J. Phys. Chem. A* 2009, **113**, 4340-4345.

Chapter 3. An Unconventional Mechanism of Hollow Nanorod Formation: Asymmetric Cu Diffusion in Au-Cu Alloy Nanorods during Galvanic Replacement Reaction

3.1 Introduction

Remarkable progress has been made in creating bimetallic hollow nanostructures from monometallic nanoparticle templates using galvanic replacement reaction (GRR) in the last decade.[1-8] Many sophisticated hollow nanostructures have been fabricated and widely used in catalysis, optical and biomedical applications.[9-13] Since the pioneer work by Xia and coworkers,[14] GRR mechanism between metal salts and monometallic nanoparticle precursors has been extensively studied. Not only monometallic nanoparticles, a few bimetallic core-shell nanostructures have also been used as the starting materials, in which either the core or the shell can be selectively etched during GRR to form hybrid nanostructures.[15-17] Etching reaction in these systems happens in segregated single element domain, which mechanism is similar to that of the monometallic systems. However, little is known about GRR using alloy nanoparticles as templates, where the reactivity of the metals in the alloy is different from that of the metal in the pure phase. This difference can potentially lower the GRR rates, allowing the diffusion of atoms at the boundary between different metals (Kirkendall effect)[18, 19] to play a more significant role in determining the hollow structure formation.[20, 21] Moreover, the diffusion of atoms in the alloy nanoparticles can be affected by the distribution of elements and the alloy phase changes during GRR.[6] In an attempt to understand the sophisticated processes,

GRR is performed between $AuCu_3$ alloy nanorods (NRs) and $HAuCl_4.3H_2O$. In the reaction intermediates, preferential diffusion of Cu atoms to one end of the NR was observed, which was originated from the difference in the metal composition at the two ends of the NR template. The mechanism was unconventional due to complex effects of dealloying, diffusion and oxidation, which was not observed before in monometallic systems. Both GRR and Kirkendall effect were found to be crucial for the hollow Au-Cu alloy NR formation. The hollow Au-Cu NRs were demonstrated as excellent catalysts for *p*-nitrophenol reduction with a k_{app}/ m^2 value of 205.

3.2 Experimental Section

3.2.1 Chemicals

Gold (III) chloride trihydrate (99%), copper (II) acetyl acetonate (97%), octadecylamine (90%), oleylamine (70%), *p*-nitrophenol (99%), sodium borohydride ($NaBH_4$, 98%) and methoxypoly (ethylene glycol) amine (PEG-NH_2) (MW=5000) were purchased from Sigma Aldrich and used without any further purification. Tetradecylamine (95%) was obtained from TCI and used as received.

3.2.2 Synthesis of $AuCu_3$ Alloy Nanorods

Monodisperse $AuCu_3$ alloy nanorods with aspect ratio of 1:3 (34.2 nm in length and 11.1 nm in diameter) were obtained following a protocol developed by Chen et. al[30] with slight modifications. The samples obtained from a single batch synthesis were used as sacrificial templates for a set of galvanic replacement reactions in order to maintain the same experimental conditions.

3.2.3 Galvanic Replacement Reaction

In a typical galvanic replacement reaction, 1 mL of 0.30 mg/mL $AuCu_3$ rod sample in toluene was added to a small glass vial. Then 0.20 mL of oleylamine was introduced into the vial while being magnetically stirred followed by the addition of freshly prepared gold precursor solution. The gold precursor was prepared by adding 1.0 mg of $HAuCl_4$ salt to 1.0 mL of chloroform. The reaction was monitored for different reaction times. In order to obtain the intermediate, the reaction was arrested by adding excess ethanol and immediately centrifuging the mixture for 5 minutes at 7000 rpm to remove the unreacted gold precursor. Then precipitate was washed in toluene and chloroform twice by centrifuging at 12000 rpm for 10 minutes to remove excess ligands in the solution and was used for further characterization.

3.2.4 Phase Transfer Reaction

PEG-NH_2 (10 mg) was dissolved in 15 mL chloroform in a 25 mL round bottomed flask and degased with nitrogen for 10 min. 2.0 mL of Au-Cu hollow rod sample (~2.0-3.0 mg/mL concentration) in toluene was added to the flask drop wise and reaction was allowed to continue for 15 hrs under nitrogen environment in dark. After the reaction, products were separated by precipitating, using 10 mL hexane and centrifuging at 12000 rpm for 20 min, followed by washing with ethanol and water and finally dispersing them in water. The same procedure was applied to $AuCu_3$ solid rod sample.

3.2.5 Catalytic Reaction

p-nitrophenol (1.4 mM) and $NaBH_4$ (0.42 M) stock solutions were prepared in DI water. 3.5 mL DI water was mixed with 0.25 mL *p*-nitrophenol and 0.50 mL $NaBH_4$. 0.20 mL of phase-transferred Au-Cu nanorods were added to this mixture. The final concentration of *p*-nitrophenol is $7.8*10^{-5}$ M and $NaBH_4$ is $4.67*10^{-2}$ M. The approximate amount of catalyst was determined to be $3.0*10^{11}$ rods /mL for solid rods and $9.0*10^{10}$ rods/mL for hollow rods. 1mL of this mixture was immediately transferred to a cuvette and was monitored using UV-VIS spectrometer. Inductively Coupled plasma -Mass Spectrometry (ICP-MS) was used to determine gold concentration in both phase transferred solid and hollow rod samples of same concentration (1.0 mg/ mL). It was found hollow rods have ~3.4 times more gold compared to solid rods. The concentration of Au in solid rods was determined to be 14390 μg/L while it was 48460 μg/L for hollow rod sample. Therefore, hollow rod sample was diluted accordingly to make sure both of the catalysts have the same gold concentration.

3.2.6 Instrumentation

UV-Vis spectrometer (Cary 60, Agilent technologies) was used to measure the extinction spectra of the nanoparticles and the absorbance of *p*-nitrophenol. A Rigaku ultima IV power X-ray diffractometer with Cu Kα radiation operated at a tube voltage of 40 KV and current of 44 mA was used to obtain the XRD patterns. TEM images were captured using a Tecnai T-12 operated at 120 KV. High angle annular dark field-scanning transmission elctron microscopy (HAADF-STEM) images and Energy dispersive x-ray (EDX) elemental mapping was performed using FEI -Talos microscope at an accelerating voltage of 200 KV.

3.3 Results and Discussion

3.3.1 Structural Characterization

In this study, $AuCu_3$ alloy NRs, oleylamine and $HAuCl_4.3H_2O$ were mixed at room temperature and allowed to react for desired time. Transmission electron microscopy

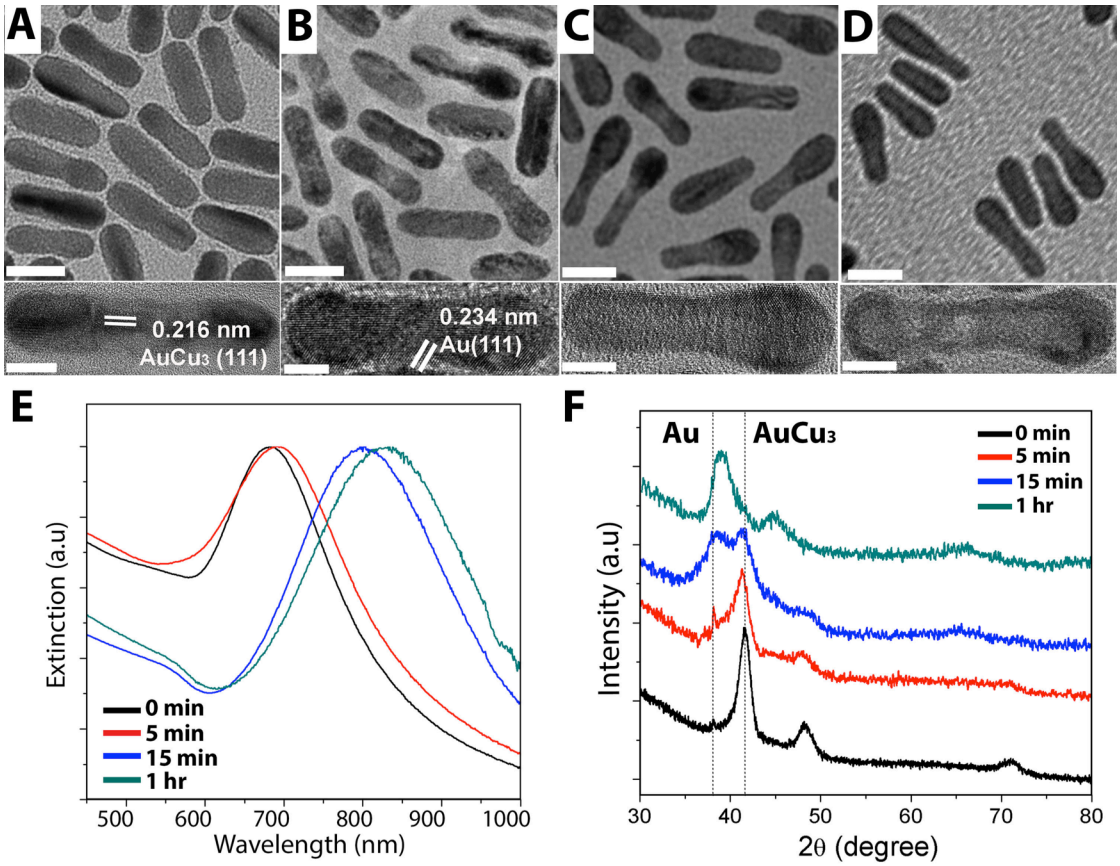

Figure 3.1. TEM images of the samples (A) $AuCu_3$ rods, and aliquots collected at 5 min (B), 15 min (C), and 1 hr (D) after injection of Au precursor. Bottom panels are the high resolution images. Scale bar = 20 nm for top panels and 5 nm for bottom panels. (E) Corresponding UV-Vis-NIR spectra and (F) XRD patterns of the samples.

(TEM) image in Figure 3.1A shows the NR templates are 11.1 ± 1.4 nm in diameter and 34.2 ± 4.0 nm in length. The lattice spacing of 0.216 nm corresponds to the (111) planes of $AuCu_3$ in the longitudinal direction of the NR from the high resolution TEM

(HRTEM) image (see bottom image of Figure 3.1A). After addition of gold precursor, samples were acquired at 5 min, 15 min and 1 hr reaction times. The 5 min sample shows

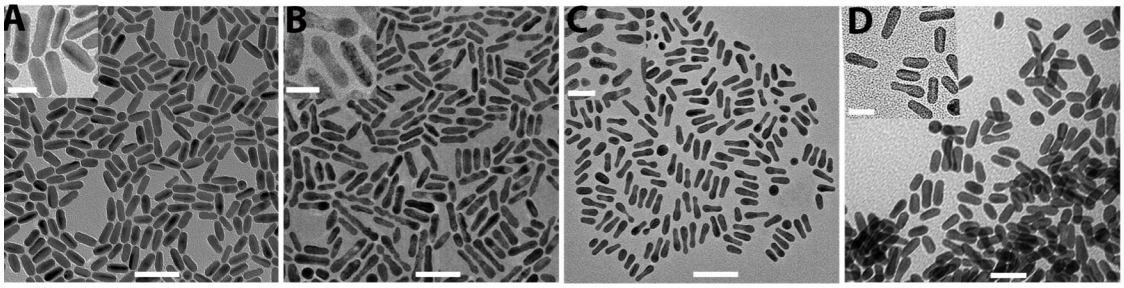

Figure 3.2. TEM images of the samples (A) $AuCu_3$ rods, and aliquots acquired at different reaction times after the injection of gold precursor (B) 5 min (C) 15 min (D) 1 hr. Scale bar = 50 nm. The scale bar in the insets = 20 nm.

no significant morphological change from the template (Figure 3.1B). But by close examination of the HRTEM image (Figure 3.1B, bottom panel), a thin Au layer of ~1.3 ± 0.2 nm was found to be deposited on the NR surface, with a lattice spacing of 0.234 nm, corresponding to Au (111) plane. In contrast, the morphology of the NRs in samples acquired at 15 min and 1 hr reaction times (see Figure 3.1C and 3.1D) was found to be different from the initial NRs. Interestingly, the 15 min sample showed a dark phase on one end with increased diameter (12.3 ± 0.3 nm) compared to other end, and also the starting material. After 1 hr reaction, hollow NRs were formed, as clearly seen in the bottom panel of Figure 3.1D. Large area TEM images are available are shown in Figure 3.2 for all the four samples. During the reaction, the extinction peak of the samples (Figure 3.1E) gradually red shift from 690 nm to 840 nm, due to the formation of hollow structures.[22] The X-ray diffraction (XRD) pattern of initial sample (black line, Figure 3.1F) has an fcc $AuCu_3$ phase (ICDD: 01-073-2643). For the 5 min sample (red line), an additional peak close to the pure fcc Au phase (ICDD: 01-071-4614) appeared at 37.9º,

due to the deposition of the thin layer of Au on the surface of the NR. This additional peak shifts towards higher degree and becomes broad indicating multiple Au rich Au-Cu phases in the 15 min sample (blue line in Figure 3.1F). The XRD pattern of the finalhollow NR can be indexed as fcc Au_3Cu alloy phase (ICDD: 01-071-5023). The morphological, optical and composition analysis showed that hollow alloy Au-Cu NRs were generated after the GRR.

3.3.2 Elemental Analysis

In order to understand the mechanism of the hollow alloy NRs formation, scanning

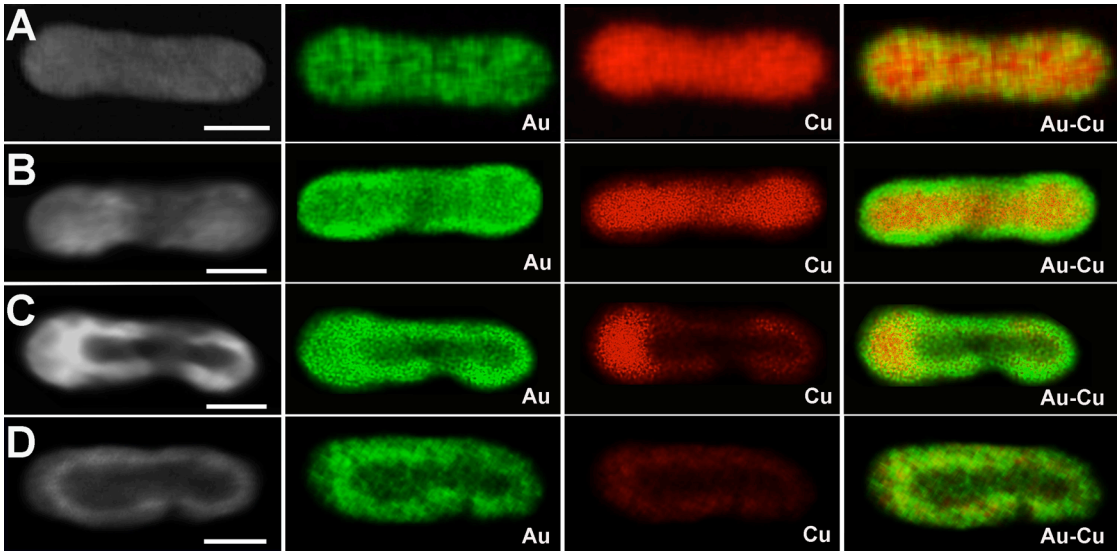

Figure 3.3 EDX elemental mapping images of samples obtained at different reaction times during galvanic replacement reaction (A) 0 min, (B) 5 min, (C) 15 min and (D) 1 hr. Green represents Au and red represents Cu in the images. Scale bar = 10 nm.

transmission electron microscopy (STEM) and Energy dispersive X-ray (EDX) analysis were performed. The results are summarized in Figure 3.3 and additional images are available in Figures 3.4, 3.5 and 3.6. The EDX mapping images of the initial $AuCu_3$ alloy NR sample (see Figure 3.3A) clearly demonstrated the presence of both Au and Cu along

the NR and rich in Cu, consistent with the XRD data in Figure 3.1F. The EDX mapping images of the intermediate obtained at 5 min of reaction (Figure 3.3B) showed again that

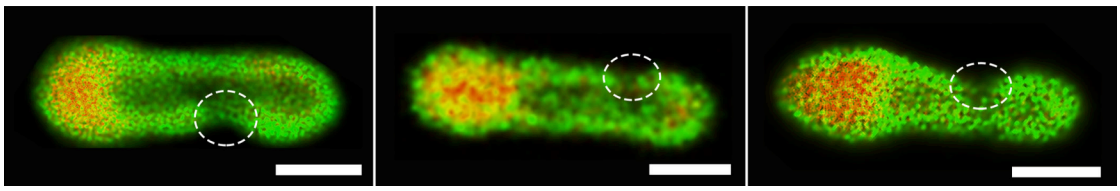

Figure 3.4. EDX elemental mapping of nanorodss acquired at 15 min of reaction. The white circles denote the holes formed in the rods. The Cu at the end close to the hole has dissolved. The diameter of the other end has increased and showed a Cu rich phase. Scale bar = 10 nm.

a thin layer of Au was deposited on surface of the NR. This is because of the replacement of Cu atoms on the surface of the rod by the reduced Au atoms. Close examination of the images revealed that the Au layer was not continuous, but had some openings. The EDX mapping images of the intermediate obtained at 15 min of reaction showed that the diameter of one end of the rod increased, and the center of the rod became hollow (see Figure 3.3C and Figure 3.4). Moreover, Cu atoms, which were uniformly distributed in

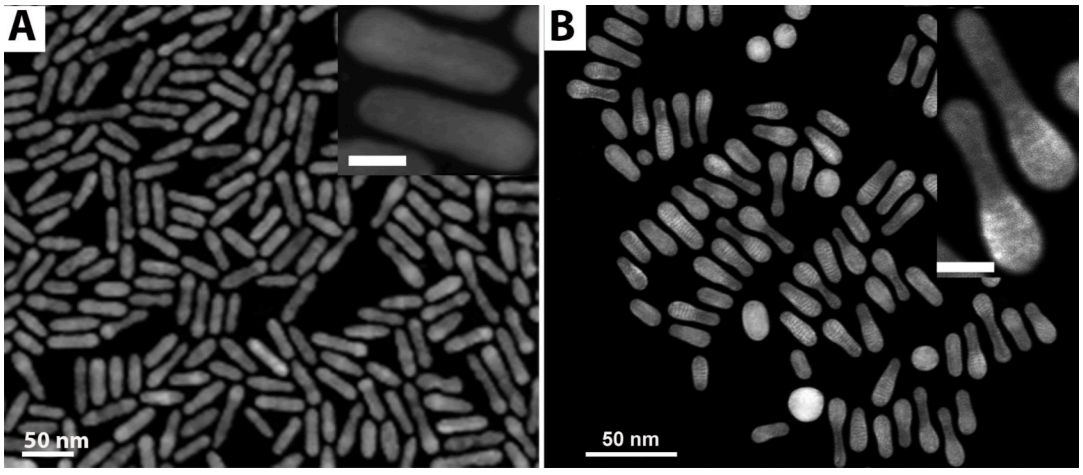

Figure 3.5. Comparison between the initial nanorod templates (A) and the 15-min sample (B). The insets clearly indicate transformation from regular rod to asymmetric structure with increased diameter of one end. The scale bar in the insets = 10 nm.

the initial NR, were found to mainly accumulate at one end of the NR; whereas Au atoms were evenly distributed at the ends and along the walls of the NR. The uneven distribution of Cu in the rod gave rise to the complex Au rich Cu phases in the XRD

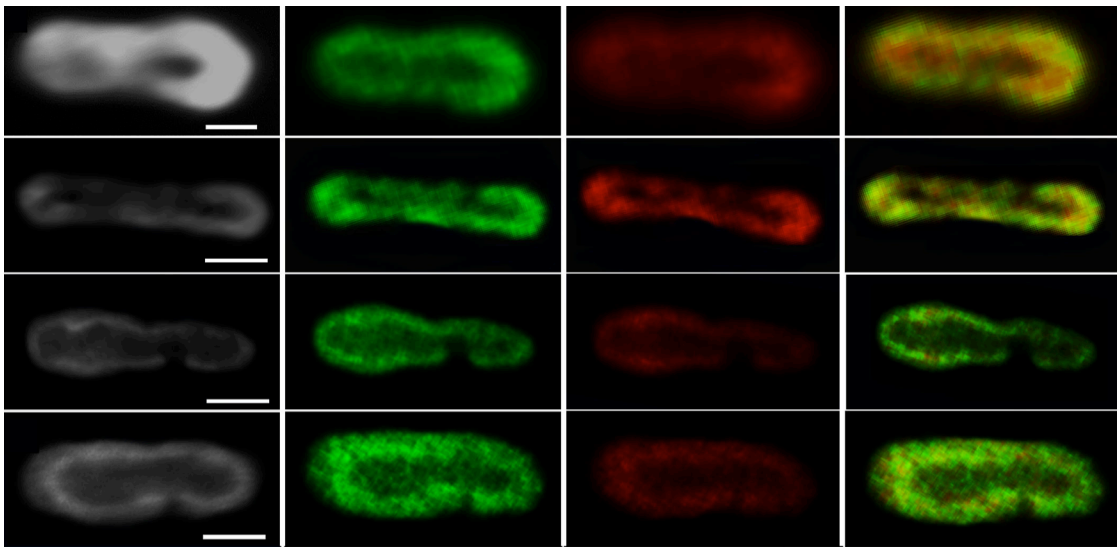

Figure 3.6. EDX elemental mapping of hollow rods obtained after 1-hr reaction. The mapping images show that the rods are hollow with uniform alloy composition in the walls. Scale bar = 10 nm.

pattern (blue line) in Figure 3.1F. Holes were also observed on the walls of NR. And in most cases, the holes were found close to one end of the NR as seen in Figure 3.4. The increase in the diameter of the Cu rich end of the NR indicates that Cu atoms had migrated from the center of the NR to the end, leading to lattice expansion (Figure 3.4 and 3.5). Not only to the end, the Cu atoms also migrated to the surface of the NR, forming the alloy walls. In the final hollow NRs, Au and Cu atoms were uniformly distributed acrosst he entire rod, showing a single Au rich Au-Cu alloy phase was present, consistent with XRD data (green line) in Figure 3.1F. This was further confirmedby mapping other hollow rod samples as shown in Figure 3.6, which display a

rich Au phase and compared to Cu. The elemental mapping studies demonstrated the transformation of solid $AuCu_3$ rod to hollow Au_3Cu structure, and revealed interesting intermediate steps where Cu atoms asymmetrically diffused to one end of the NR

3.3.3 Mechanism

The discovery of the unusual reaction intermediates suggests that multiple processes are involved in the formation of hollow Au-Cu NRs. Distribution of elements needs to be considered in the alloy system in addition to crystal facets and surface ligands, which are known to affect GRR in monometallic systems[1]. From the experimental data, the hollow NR formation mechanism is proposed, and the important steps are illustrated in Scheme 1. At the beginning of the GRR (step1), Cu atoms on the surface of NR react with the Au

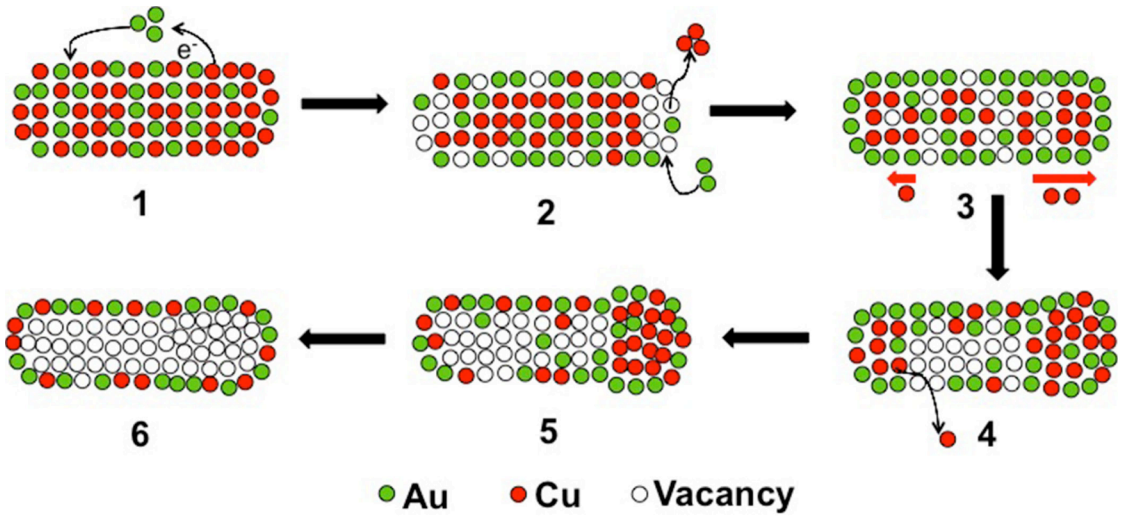

Scheme 3.1. Mechanism of hollow Au-Cu nanorod formation

precursor, dealloying from the fcc $AuCu_3$ phase and get oxidized, forming vacancies in the NR. This dealloying process is analogous to that occurred at later stages of the GRR in monometallic nanoparticles when the walls become alloy. Selective removal of one of the components from this alloy wall results in porosity of the walls. In our case, although

vacancy formation happens on the entire surface of the rod, it is expected to be faster at the ends compared to sides, due to the higher reactivity of ends[23, 24] (step 2).

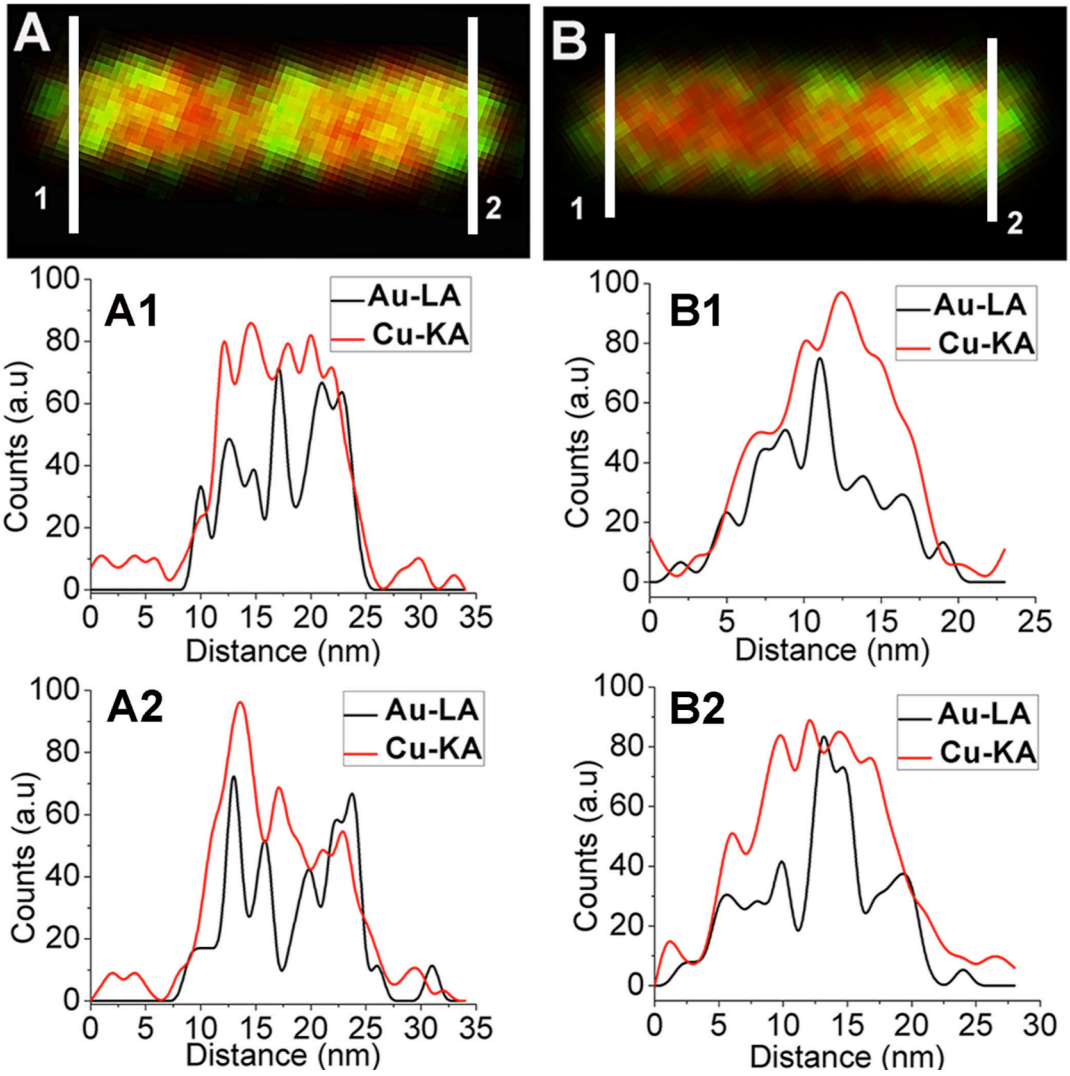

Figure 3.7. Line scans performed on the two ends of the initial $AuCu_3$ alloy rods A and B. The line scans 1 and 2 performed transversely on each end of the rod clearly show that the two ends have unequal distribution of Cu (red line).

Simultaneously, Au precursor gets reduced and Au atoms are epitaxially deposited all over the NR (step 3), forming the intermediate structure observed in Figure 3B. The Au layer is not uniform and has some openings likely because the stoichiometric ratio of Au

and Cu is 2:3 ($3Cu(s) + 2HAuCl_4(aq) \rightarrow 3CuCl_2(s) + 2HCl + 2Au(s)$).[25] The epitaxially deposited thin Au layer protects the Cu atoms in the NR from further oxidation. The already formed holes serve as the access pointfor the Cu atoms inside to get further oxidized and dissolved.[1, 14] Also, dealloying reduces the rate of the galvanic replacement, which allows the Cu atoms to diffuse to the vacant sites due to Kirkendall

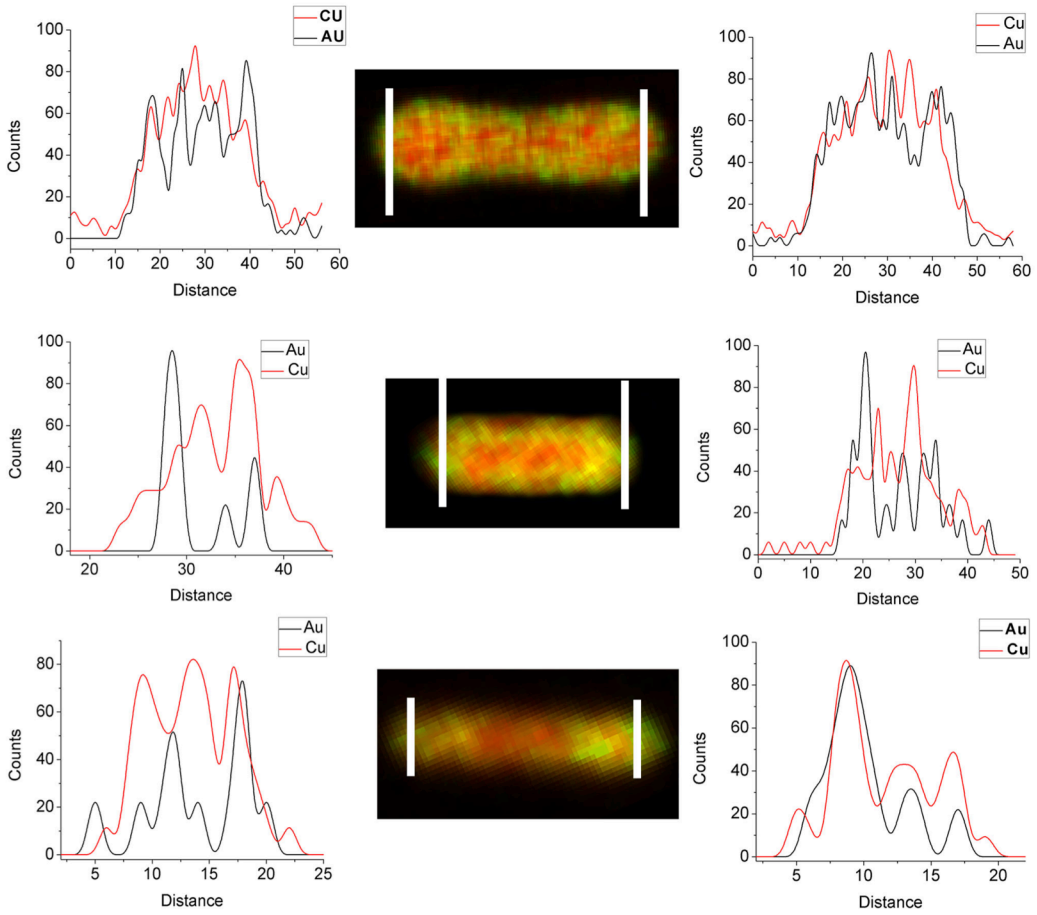

Figure 3.8. Additional line scans performed on two ends of the initial $AuCu_3$ alloy rods. The line scans clearly indicate two ends have unequal distribution of copper (red line).

effect[20] before they get oxidized through the hole. Because more vacancies are formed at the ends of the rod compared to sides (in step 2), there is preferential migration of Cu towards the ends where vacancies migrate to the center (step 4). However, from Figure

1C and 3C, the diffusion of Cu atoms is asymmetrically towards one end of the rod. To understand the origin of the asymmetric diffusion of Cu, the elemental distribution of the ends of the initial $AuCu_3$ NRs was analysed from EDX line scans across the rods as shown in Figure 3.7 and 3.8. The analysis shows that the Cu content at one end of the samerod is often higher than the other end. During initial GRR process, the end with more Cu will be depleted faster compared to the other end, leaving more vacancies at that end. The vacancies in other parts of the NR tend to diffuse together to that end resulting in hollowness in the NR. Similar phenomenon was observed in the GRR between Ag wire and gold salt.[1] Meanwhile, the depletion of Cu drives the Cu atoms close by to migrate fast to the vacancies, resulting in an increased diameter of the end, and enrichment of Cu at the end compared to the rest of the rod (step 5). Also, notice that the holes are often formed close to one end of the NR (Figure 3C and Figure 4). The Cu

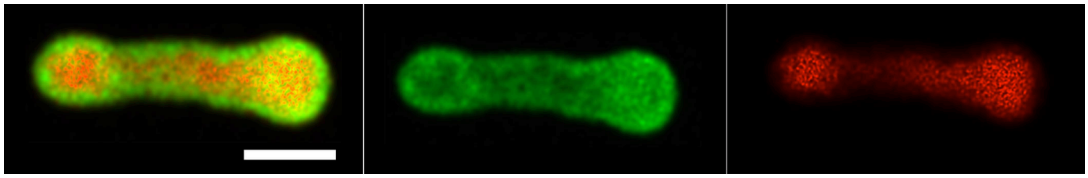

Figure 3.9. EDX elemental mapping images of an intermediate obtained at 15 mins of reaction, in which copper is migrating to both the ends of the rod. Scale bar=10 nm.

atoms close to the holes are dissolved prior to diffusion to the end, leading to a hollow end. In rare cases, diffusion of Cu atoms to both ends was observed; proving again Cu distribution was not uniform at the ends for the NR precursors as shown in Figure 3.9. Following the formation of asymmetric hollow structure, the Cu atoms were further depleted from the NR as the reaction progressed. In the meantime, both Au and Cu atoms migrate to the walls of the NRs (step 6), forming the final hollow Au-Cu alloy NRs

Notice GRR is much faster than diffusion, which is why Kirkendall effect is not significant in the formation of many hollow nanostructures using monometallic templates. However, the oxidation of Cu in $AuCu_3$ alloy is expected to be much slower than that in pure Cu. In addition, the presence of olelyamine in reaction can also slow down the GRR.[26] For the system under investigation, GRR and Kirkendall effect are both crucial in the process and responsible for the unique intermediate formation.

3.3.4 Catalytic Activity

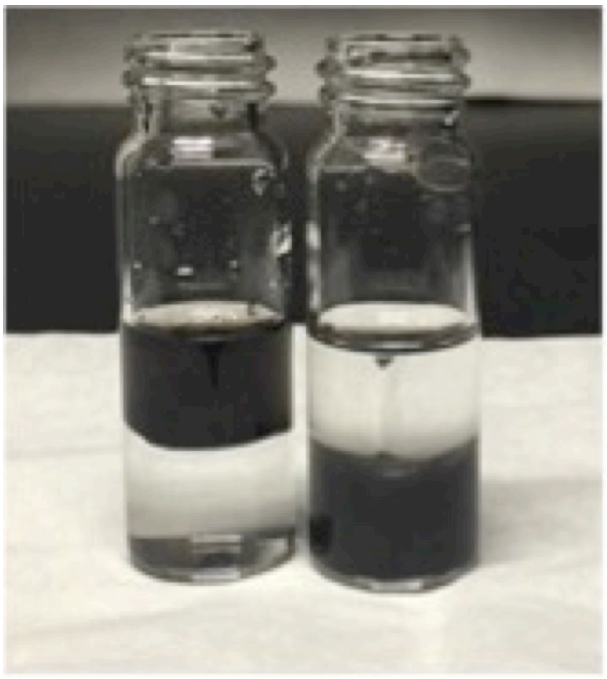

Figure 3.10. Photograph of Au-Cu nanorods in oil phase on the left and in water on the right after the phase-transfer.

Hollow nanostructures are known to exhibit great catalytic activities.[1] In this study, the alloy hollow NRs was used to catalyze *p*-nitrophenol reduction reaction with $NaBH_4$. Ligand exchange was performed to transfer the hollow Au-Cu NRs from toluene to water as shown in Figure 3.10. The absorbance of p-nitrophenol at 400 nm was monitored and a gradual reduction was observed over time, as shown in Figure 3.11A and 3.11B. The reaction was considered to be

pseudo first order since $NaBH_4$ concentration was in excess. The catalytic performance of the hollow NRs was compared with $AuCu_3$ solid rods. The gold concentration in both samples was kept constant, as determined by inductively

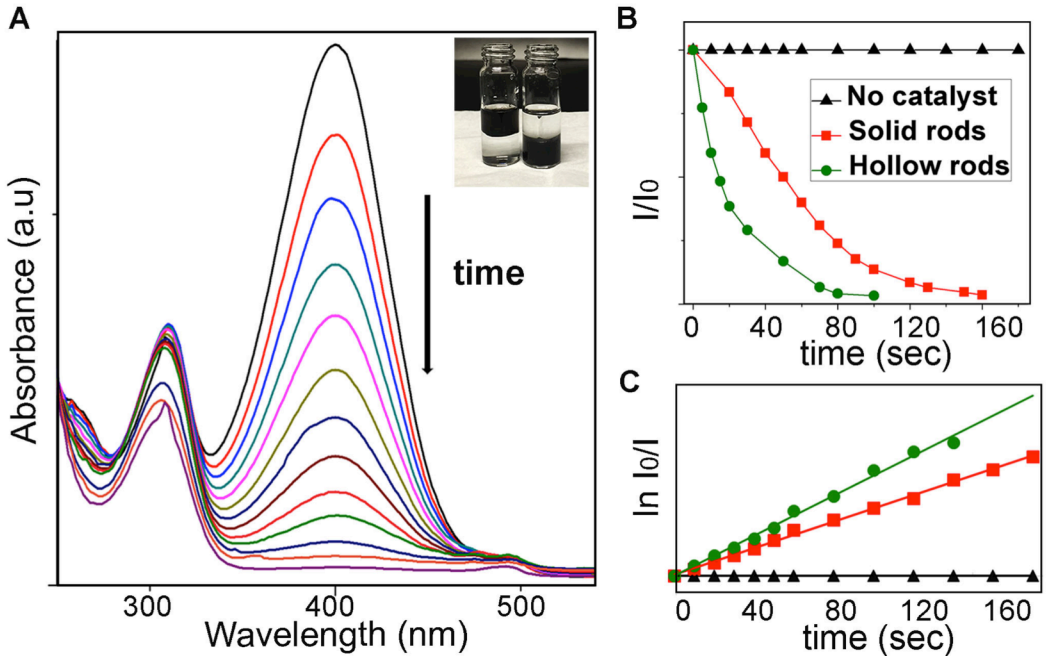

Figure 3.11. *P*-nitrophenol reduction reaction. (A) Absorption spectra of *P*-nitrophenol during reduction with Au-Cu hollow nanorods. The absorbance at 400 nm gradually decreases with time due to the conversion of *P*-nitrophenol to *P*-aminophenol. (B) Plot of the normalized concentration of *P*-nitrophenol versus time in the absence and presence of catalysts. (C) Corresponding fitting of the natural log of the normalized concentration versus time.

coupled plasma mass spectrometry as described in experimental section. The apparent reaction constant (k_{app}) value for the hollow rods (k_{app} = 0.0257 sec^{-1}) is 1.5 times of that of the solid rods (k_{app} =0.0169 sec^{-1}). In addition, we normalized k_{app} to the surface area of the catalysts. The (k_{app}/m^2) value of solid rods is 41, while that of the hollow rods is 205, much higher than previously reported

values.[27,28] The high catalytic efficiency of the Au-Cu hollow rods is due to several contribution factors. The Au-Cu alloy composition together with the specific crystal facets of the rod provides optimal binding of p-phenol to the surface.[27,28] The hollow internal structure and the higher number of Au atoms exposed increases the active surface available for the catalytic reaction to occur.[29]

3.4 Conclusion

To summarize, hollow Au-Cu alloy NRs were obtained by GRR between $AuCu_3$ alloy NRs and $HAuCl_4.3H_2O$ at room temperature. The TEM and XRD studies of the reaction intermediates and final products showed a gradual change in the morphology and composition of the NRs. Elemental mapping analysis revealed preferential diffusion of Cu atoms to one end of the NR during reaction, originated from the difference in the Cu content at the two ends of the $AuCu_3$ alloy NR templates. It is discovered that GRR and Kirkendall effect are both crucial for the formation of the hollow rod with excellent catalytic activity. The understanding of the reaction mechanisms of GRR using metal alloy nanoparticle as templates is critical to the fabrication of hollow structures with unique morphology, composition and promising applications.

3.5 Reference

1. X. Xia, Y. Wang, A. Ruditskiy and Y. Xia, *Adv. Mater.*, 2013, **25**, 6313-6333.
2. Y. Sun and Y. Xia, *Science*, 2002, **298**, 2176-2179.
3. S. E. Skrabalak, J. Chen, Y. Sun, X. Lu, L. Au, C. M. Cobley and Y. Xia, *Acc. Chem. Res.*, 2008, **41**, 1587-1595.
4. Y. Sun, B. T. Mayers and Y. Xia, *Nano Lett.*, 2002, **2**, 481-485.
5. H. Jing and H. Wang, *Chem. Mater.*, 2015, **27**, 2172-2180.
6. E. González, J. Arbiol and V. F. Puntes, *Science*, 2011, **334**, 1377-1380.
7. M. H. Oh, T. Yu, S.-H. Yu, B. Lim, K.-T. Ko, M.-G. Willinger, D.-H. Seo, B. H. Kim, M. G. Cho, J.-H. Park, K. Kang, Y.-E. Sung, N. Pinna and T. Hyeon, *Science*, 2013, **340**, 964-968.
8. G. S. Métraux, Y. C. Cao, R. Jin and C. A. Mirkin, *Nano Lett.*, 2003, **3**, 519-522.
9. M. Chandra, A.-M. Dowgiallo and K. L. Knappenberger, *J. Am. Chem. Soc.*, 2010, **132**, 15782-15789.
10. L. Zhang, L. T. Roling, X. Wang, M. Vara, M. Chi, J. Liu, S.-I. Choi, J. Park, J. A. Herron, Z. Xie, M. Mavrikakis and Y. Xia, *Science*, 2015, **349**, 412-416.
11. C. Chen, Y. Kang, Z. Huo, Z. Zhu, W. Huang, H. L. Xin, J. D. Snyder, D. Li, J. A. Herron, M. Mavrikakis, M. Chi, K. L. More, Y. Li, N. M. Markovic, G. A. Somorjai, P. Yang and V. R. Stamenkovic, *Science*, 2014, **343**, 1339-1343.
12. Y. Xia, W. Li, C. M. Cobley, J. Chen, X. Xia, Q. Zhang, M. Yang, E. C. Cho and P. K. Brown, *Acc. Chem. Res.*, 2011, **44**, 914-924.
13. M. S. Yavuz, Y. Cheng, J. Chen, C. M. Cobley, Q. Zhang, M. Rycenga, J. Xie, C. Kim, K. H. Song, A. G. Schwartz, L. V. Wang and Y. Xia, *Nat. Mater.*, 2009, **8**, 935-939.
14. Y. Sun and Y. Xia, *J. Am. Chem. Soc.*, 2004, **126**, 3892-3901.
15. X. Guo, Q. Zhang, Y. Sun, Q. Zhao and J. Yang, *ACS Nano*, 2012, **6**, 1165-1175.
16. X. Guo, W. Ye, H. Sun, Q. Zhang and J. Yang, *Nanoscale*, 2013, **5**, 12582-12588.
17. Y. Khalavka, J. Becker and C. Sönnichsen, *Journal of the American Chemical Society*, 2009, **131**, 1871-1875.

18. W. Wang, M. Dahl and Y. Yin, *Chem. Mater.*, 2013, **25**, 1179-1189.
19. Y. Yin, R. M. Rioux, C. K. Erdonmez, S. Hughes, G. A. Somorjai and A. P. Alivisatos, *Science*, 2004, **304**, 711-714.
20. Y. Liu and A. R. Hight Walker, *ACS Nano*, 2011, **5**, 6843-6854.
21. D. Thiry, L. Molina-Luna, E. Gautron, N. Stephant, A. Chauvin, K. Du, J. Ding, C.-H. Choi, P.-Y. Tessier and A.-A. El Mel, *Chem. Mater.*, 2015, **27**, 6374-6384.
22. J. B. Jackson and N. J. Halas, *J. Phys. Chem. B*, 2001, **105**, 2743-2746.
23. C.-K. Tsung, X. Kou, Q. Shi, J. Zhang, M. H. Yeung, J. Wang and G. D. Stucky, *J. Am. Chem. Soc.*, 2006, **128**, 5352-5353.
24. M. N. O'Brien, M. R. Jones, K. A. Brown and C. A. Mirkin, *J. Am. Chem. Soc.*, 2014, **136**, 7603-7606.
25. S. Thota, S. Chen, Y. Zhou, Y. Zhang, S. Zou and J. Zhao, *Nanoscale*, 2015, **7**, 14652-14658.
26. S. Mourdikoudis and L. M. Liz-Marzán, *Chem. Mater.*, 2013, **25**, 1465-1476.
27. R. He, Y. C. Wang, X. Wang, Z. Wang, G. Liu, W. Zhou, L. Wen, Q. Li, X. Wang, X. Chen, J. Zeng and J. G. Hou, *Nature Comm.*, 2014, **5**, 4327-4337.
28. M. Hajfathalian, K. D. Gilroy, A. Yaghoubzade, A. Sundar, T. Tan, R. A. Hughes and S. Neretina, *J. Phys. Chem. C*, 2015, **119**, 17308-17315.
29. S. V. Jenkins, S. Chen and J. Chen, *Tetrahedron Lett.*, 2015, **56**, 3368-3372.
30. Chen, S.; Jenkins, S. V.; Tao, J.; Zhu, Y.; Chen, J. *J. Phys. Chem. C* **2013**, *117*, 8924-8932.

Chapter 4. Formation of Bimetallic Dumbbell Shaped Particle with a Hollow Junction during Galvanic Replacement Reaction

4.1 Introduction

Multimetallic nanoparticles possess numerous functionalities on a single platform.[1-4] Fine tuning of their morphology and composition via synthetic methods generates nanostructures with promising applications in many areas including electronics, photonics, sensing, medical diagnostics and catalysis.[4-11] However, precise control of the structure of multimetallic nanoparticles at the atomic level is still a synthetic challenge, due to differences in the lattice parameters and physical properties of the individual components.[4, 12, 13] Instead of direct control of the structure during synthesis, post-synthetic structural modification of pre-prepared nanoparticle templates is an alternative strategy.[14-17] Among these methods, galvanic replacement reaction (GRR) is the most widely employed technique to create multimetallic nanoparticles with complex morphologies. GRR occurs between two metallic species of different redox potentials. At the nanoscale, metal atoms in a nanoparticle can be oxidized and dissolved by metal ions of higher redox potential, which get reduced and deposited onto the nanoparticle.[18-20] Pioneered by Sun and Xia,[21] GRR has been applied in monometallic systems to transform their structure from solid nanoparticles to hollow nanoparticles like nanocages, nanoframes and so on.[22-27]

Although GRR has been extensively studied in many monometallic systems, the investigation of GRR mechanisms for metal alloy nanoparticles only started a couple

years ago.[15, 26-27] Understanding GRR in multimetallic systems is critical to control corrosion in metal alloys and thus protect these systems from oxidation. The GRR rate is often fast in monometallic nanosystems, where high precursor concentration often leads to breaking of the nanoparticles into small pieces.[18, 28] In addition, the diffusion of atoms[29] is less likely to occur during the course of the reaction due to the fast GRR rate and low reaction temperature (often room temperature). Puntes and co-workers showed that when the rate of replacement reaction is reduced by employing proper ligands, the Kirkendall effect becomes significant and more sophisticated nanostructures can be fabricated.[22] GRR in bimetallic systems involves more complex processes such as dealloying,[14, 15, 30] surfaces and inner atoms diffusion and dissolution. In order to reveal these complex dynamics in situ single particle level measurements are essential, due to unavoidable heterogeneity in the initial templates.[31-33] Single particle dark field scattering have been used to monitor structural and composition changes by tracking localized surface plasmon resonance (LSPR) of the nanoparticle during reaction.[34, 35] Together with scanning transmission electron microscopy- energy dispersive X-ray spectroscopy (STEM-EDS) measurements, reaction mechanisms and critical intermediate states were revealed by in situ dark field scattering studies as demonstrated previously. [36, 37]

In this study, we use Au-Cu alloy nanorods and $HAuCl_4$ as a model system to demonstrate how manipulating oxidation rates can affect the morphologies of the nanoparticles during GRR. That is, when $HAuCl_4$ precursor concentration is varied during GRR, AuCu alloy nanorods transform into hollow rods or break at the center into AuCu@Au spheroids. The breaking of the nanorod results in an intermediate state, in which the nanorod has an asymmetric dumbbell shape with a hollow junction in the

middle. In situ single particle scattering trajectories and STEM-EDS studies suggest that a critical reason for the formation of the hollow junction was tip preferential GRR at the initial stages. Tip preferential GRR occurs due to the penta twinned structure and high curvature at the tips of the nanorod template, yielding a faster GRR at the tips of the nanostructure. Further electrodynamic simulations revealed that by adjusting the hollowness of the junction, plasmon resonance of the dumbbell particle can be tuned from visible to near infrared and different plasmon modes arise due to the conductive coupling between the two ends. The plasmonically active intermediates provide an excellent platform to study the conductive plasmonic coupling between two components connected by a conductive but hollow junction.

4.2 Experimental Section

4.2.1 Chemicals

Copper (II) acetyl acetonate (97%), gold (III) chloride trihydrate (99%), oleylamine (70 %), octadecylamine (90%) were purchased from Sigma Aldrich and tetradecylamine (95%) was purchased from TCI. All the chemicals were used as received.

4.2.2 Galvanic Replacement Reaction

$AuCu_3$ alloy nanorods with an aspect ratio of 2.8 (35.5 nm in length and 12.6 nm in diameter) were synthesized following the literature[38]. Nanorods synthesized in a single batch were used in the GRR reactions. 1 mL of 0.43 mg/mL $AuCu_3$ rods in toluene and 0.20 mL of oleylamine were added into a glass vial. 2.54 mM $HAuCl_4$ solution in chloroform was prepared right before the reaction. A varied volume of $HAuCl_4$ solution

(0.65 mL, 0.8 mL, 1 mL and 2 mL) was added to the stirring nanorod solution. The reaction was allowed to proceed for 1 hr and monitored by UV-vis spectroscopy. To acquire reaction intermediates, excess ethanol was added to the reaction solution at desired times and the mixture was centrifuged for 5 minutes at 7000 rpm. The precipitate was further purified by washing twice in a mixture of toluene: ethanol (1:9 v/v) followed by centrifugation. All the GRR experiments were carried out at room temperature.

4.2.3 Dark Field Scattering Spectroscopy of Single Particles

To prepare the sample for the single particle studies, 10 μL of highly diluted Au-Cu nanoparticle solution in toluene was drop casted onto a clean No.1 coverslip (Fisher Scientific) and allowed to dry. The sample was then mounted onto a Nikon Ti-u microscope and illuminated by an unpolarized halogen lamp through a dark field condenser (NA 0.85). The light scattered by the single nanoparticles was collected using a 100x oil immersion objective (variable NA 0.8-1.3) at NA of 0.8. The signal was then sent to a spectrograph (Isoplane SCT 320, Princeton Instruments) equipped with a CCD camera (PIXIS 1024 BR, Princeton Instruments). The entrance slit was adjusted so signal from a single particle was collected. Under the same experimental setting, background signal was collected from a nearby region without nanoparticles. The spectra of the nanoparticle are corrected for the background. For in situ measurements, $AuCu_3$ nanorods were mounted in a home-built flow-cell and 20 μL of water was injected into the flow cell to obtain the scattering spectra at 0 min. This was done to ensure the refractive index of the medium around the nanoparticles remained same during the reaction. Then 20 μL of gold precursor (1 mg Au/1mL water) was injected into the flow-cell and spectra were collected at specific time intervals for 2 hrs.

4.2.4 Instrumentation

Extinction spectra of the nanoparticles were obtained using a UV-Vis spectrometer (Cary 60, Agilent technologies). Transmission electron microscopy (TEM) images were acquired using a Tecnai T-12 microscope operated at an accelerating voltage of 120 KV. High angle annular dark field-scanning transmission electron microscopy (HAADF-STEM) images and energy dispersive X-ray (EDX) elemental mapping measurements were performed using a FEI -Talos microscope operated at an accelerating voltage of 200 KV.

4.2.5 Theoretical Model

Discrete dipole approximation (DDA) method is used in the theoretical calculations.[39] The DDA method is a numerical method to solve the Maxwell equations. In the method, the target metal nanorod is represented with an array of polarizable cubes. The coupled dipole method is used to investigate the interactions among polarizable cubes and the cubes interaction with incident light. As long as the size of the polarizable cube is small enough, the electrodynamics simulations are close to exact. In our calculations, the size of the polarizable cube is 0.25 nm. The dielectric function of Au and Cu are taken from the Palik Handbook.[40]

4.3 Results and Discussion

4.3.1 Concentration Dependent GRR

GRR between $AuCu_3$ nanorods and $HAuCl_4$ was investigated at varied $HAuCl_4$ concentrations. The progress of GRR was monitored using UV-Vis spectroscopy as

shown in Figure 4.1 and the peak wavelengths and intensity of the UV-Vis spectra

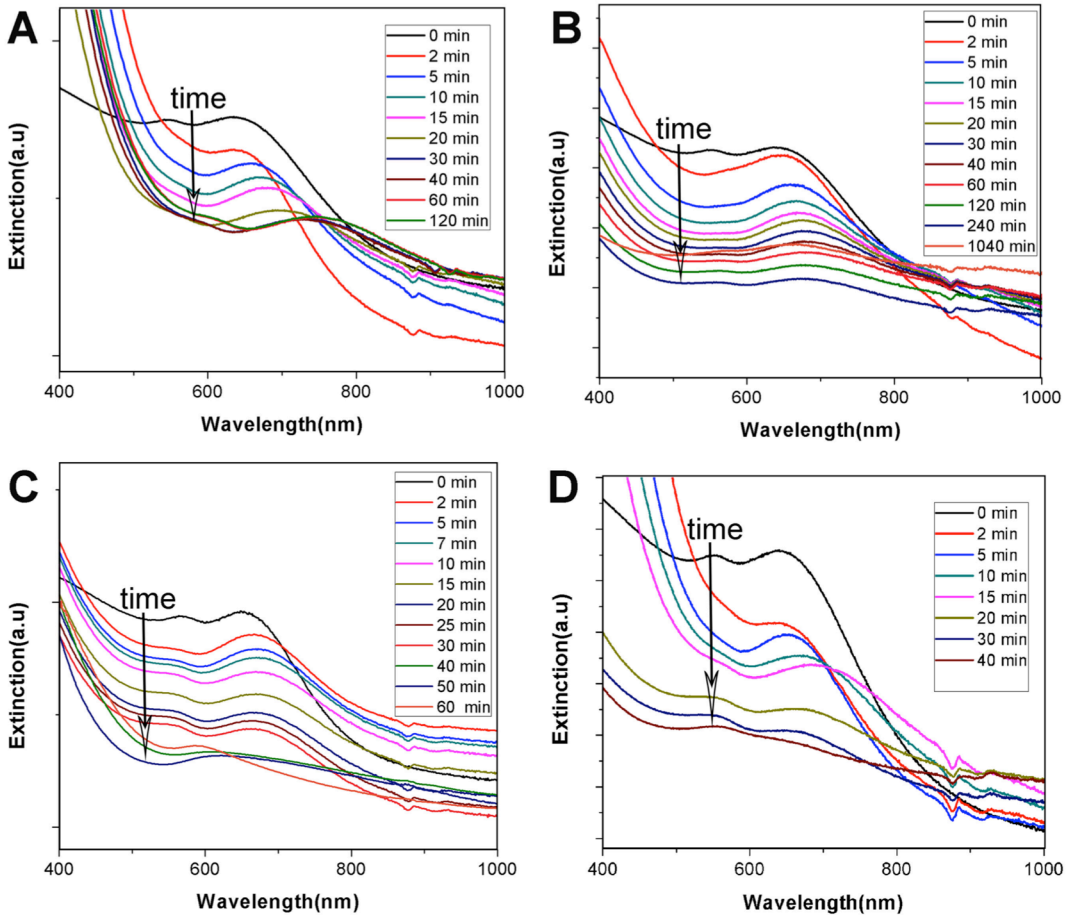

Figure 4.1. In situ UV-visible extinction spectra of AuCu alloy nanorods during galvanic replacement reaction with $HAuCl_4$ of different volumes (A) 0.65 mL, (B) 0.80 mL, (C) 1 mL and (D) 2 mL.

indicated the reaction progress. Specifically, different volumes of 2.54 mM $HAuCl_4$ solution, i. e. 0.65 mL, 0.80 mL, 1.0 mL and 2.0 mL were added to 1 mL of $AuCu_3$ nanorod solution and were reacted for 1 hr at room temperature. The peak wavelength of the solutions was plotted as a function of time and shown in Figure 4.2A. When 0.65 mL of $HAuCl_4$ was added, the extinction peak of the solution continued to red shift (Figure 4.2A, black line), indicating the formation of hollow rods, which was also proven by

TEM (Figure 4.2B).[41, 42] These findings are consistent with our previous studies where

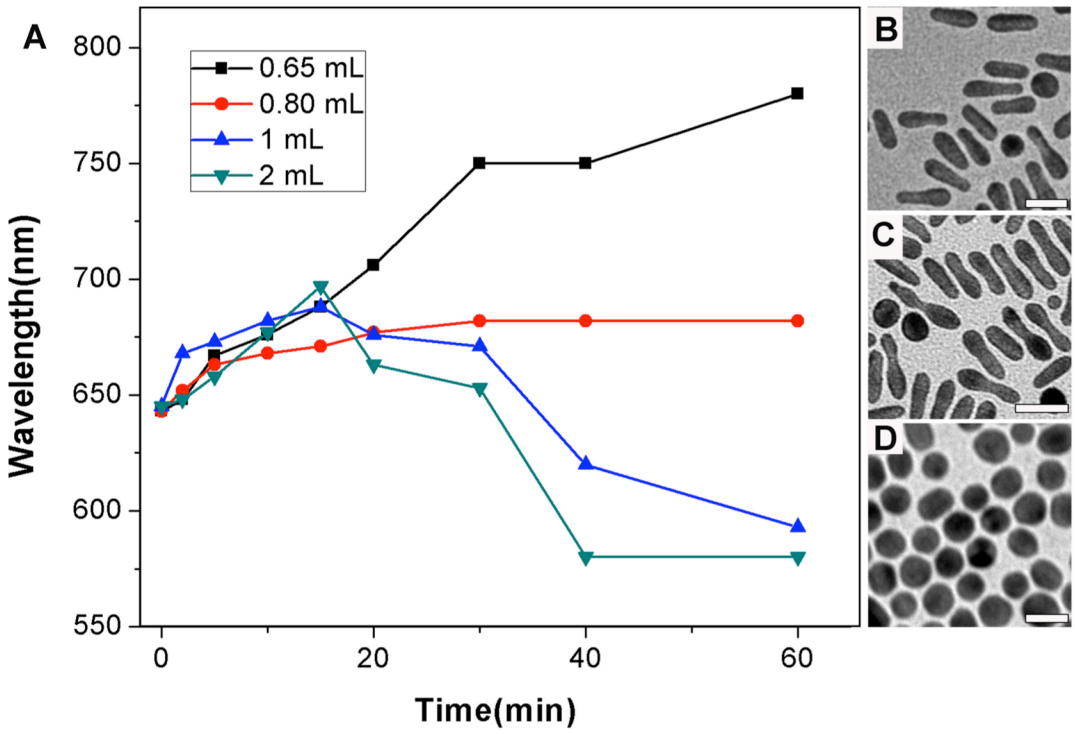

Figure 4.2. GRR between $AuCu_3$ nanorods and varied concentrations of $HAuCl_4$ monitored by UV-vis spectroscopy and TEM. (A) Extinction peak wavelength of four samples vs. reaction time. The volumes of $HAuCl_4$ are 0.65 mL (black line), 0.80 mL (red line), 1 and 2 mL (blue and cyan lines). The morphology of the corresponding products were studied by TEM showing (B) hollow rods at 0.65 mL, (C) mixture of hollow and peanut particles at 0.80 mL, and (D) spheroidal particles at 1 and 2 mL. Scale bar= 20 nm.

0.5 mL of $HAuCl_4$ was used to react with $AuCu_3$ nanorods.[43] When 1.0 mL or 2.0 mL of $HAuCl_4$ precursors were added, the extinction spectra initially red shifted and then blue shifted to ~580 nm (blue and cyan lines in Figure 4.2A). TEM images of the final products showed that the nanorod turned into spheroids (Figure 4.2D). Due to the faster GRR rate, the reaction reached completion at ~ 40 mins when 2.0 mL of $HAuCl_4$ was

added to the solution. This was 20 mins earlier than when only 1.0 mL of $HAuCl_4$ was included in the reaction. Interestingly, when 0.80 mL of $HAuCl_4$ was added, the extinction spectra red shifted during the reaction. (Figure 4.2A, red line). Once the reaction reached 30 mins, no further changes were observed in the spectra for 19 hrs (Figure 4.1B). TEM characterization of the products revealed that there was a mixture of dumbbell-shaped particles, hollow nanorods, and some spheroidal particles, as shown in Figure 4.2C. The results suggested that there are two reaction pathways, dictated by volume of $HAuCl_4$ precursors, which directly controls the GRR rate.

The TEM (Figure 4.2C) of the products, when an intermediate $HAuCl_4$ concentration (volume of 0.8 mL) was used, suggested that the nanorods might have undergone a dumbbell-shaped intermediate state before breaking. In order to understand how the structure transforms, samples were collected at different reaction times when 1.0 mL $HAuCl_4$ was added and studied using TEM. Figure 4.3 A-I shows the large area TEM, high resolution TEM (HRTEM), and atomic resolution image of the samples before the reaction (A-C), at 30 mins (D-F), and 1 hr (G-I) of the reaction. From Figure 4.3A, the aspect ratio of the $AuCu_3$ nanorod templates is 2.8 with an average length of 35.5±4.2 nm and diameter of 12.6±1.3 nm. The atomic resolution image in Figure 4.3C obtained from the boxed region in the HRTEM images in Figure 4.3B, indicates a lattice spacing of 0.216 nm, corresponding to (111) plane of $AuCu_3$, consistent with previous results.[43, 44] At 30 mins of reaction, the initial nanorods turned into dumbbell shaped particles, where two particles on the ends are connected by a narrow junction (neck), as shown in Figure 4.3D. The particles on the sides having a diameter of 13.6±1.5 nm and a narrow junction portion (neck) with a diameter of approximately 7.8 nm. Careful observation of the

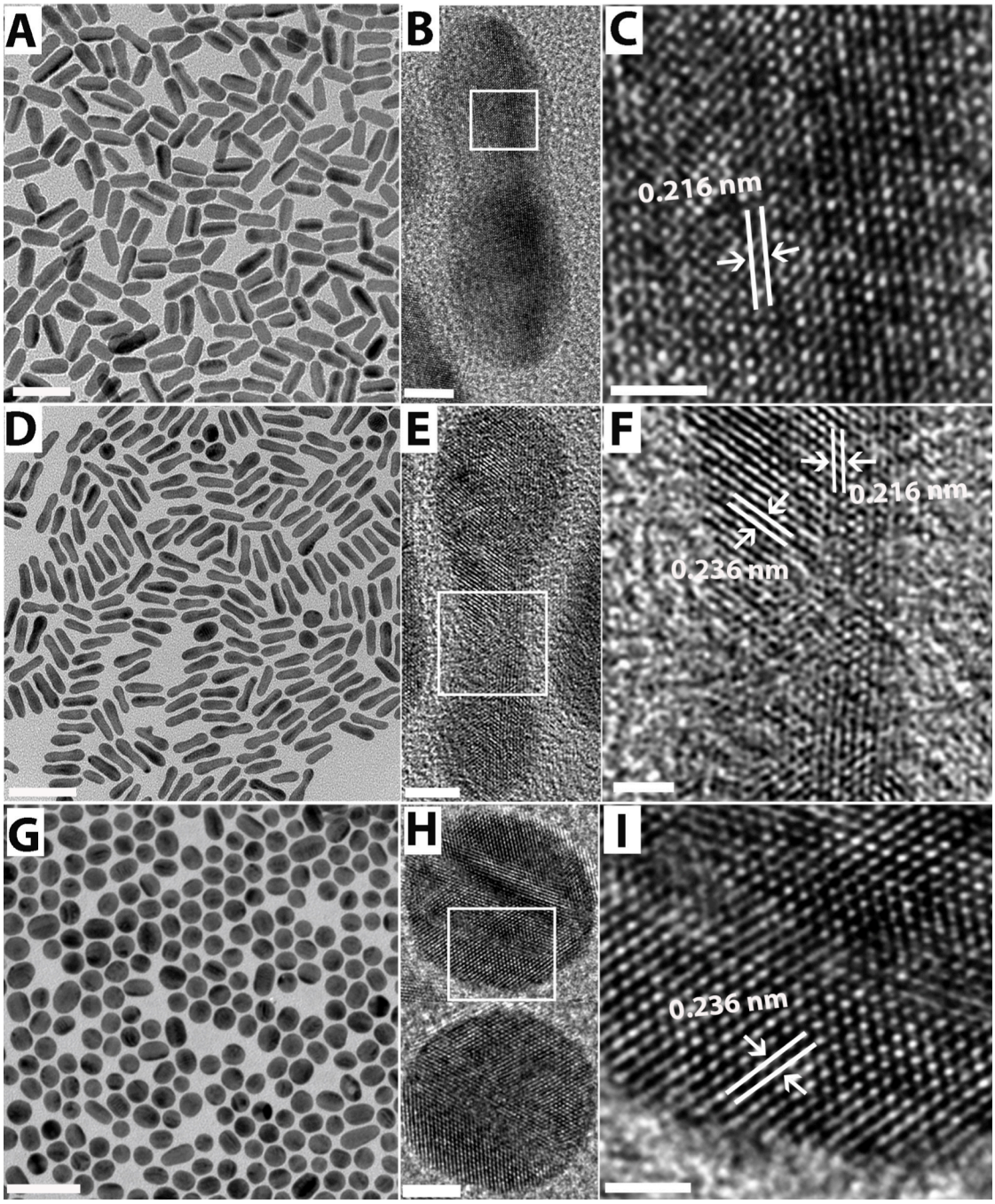

Figure 4.3. TEM images of the samples: initial $AuCu_3$ rods (A), and aliquots collected at 30 min (D) and 1 hr (G) after the injection of Au Precursor. (B and C), (E and F) and (H and I) are the corresponding high-resolution TEM images. Scale bar= 50 nm for (A), (D) and (G), 5 nm for (B), (E) and (H), and 1 nm for (C), (F) and (I).

HRTEM image (Figure 4.3E) of a single particle indicates that the neck portion might be

hollow (boxed region). Further confirmation is needed though to determine the hollowness of the neck region. The lattice spacing of the outer surface of the rod is 0.236 nm along, corresponding to the (111) planes of pure fcc Au phase, while that of the center of the rod remains at 0.216 nm (Figure 4.3F). The result shows that Au has been deposited on the surface of the nanorod. The sample collected after 1hr reaction time was found to be nearly spherical with an average diameter of 17.8±3.5 nm (Figure 4.3G), much bigger than the diameter of the initial nanorods. The particles are solid as seen in Figure 4.3H, and Figure 4.3I indicates again the deposition of Au on the surface of the particles, which results in the particle size growth.

The TEM of the intermediate dumbbell-shaped particles with a hollow "neck" indicates the diffusion of atoms must have occurred before the nanorods break. In order to offer insight into how the Cu and Au atoms in the nanorods rearrange and diffuse during GRR,

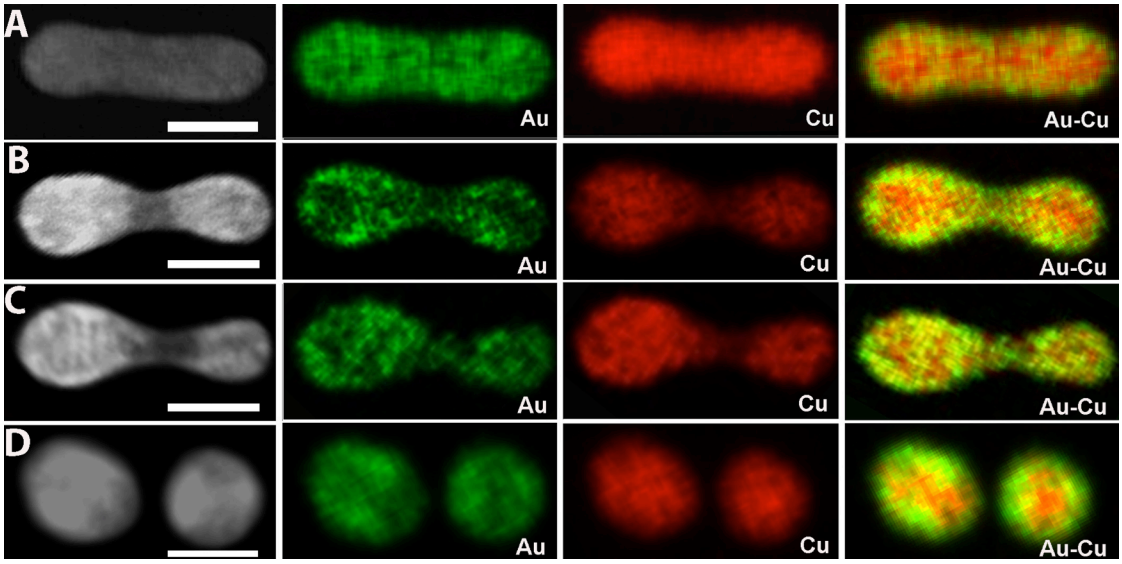

Figure 4.4. EDX elemental mapping images of samples obtained at different reaction times during the galvanic replacement reaction; (A) 0 min, (B) 30 min, (C) 45 min and (D) 1 hr. Green represents Au and red represents Cu in the images. Scale bar=10 nm.

STEM-EDX elemental mapping was performed on the samples. Figure 4.4A shows the EDX map of the initial nanorod template, with both Au and Cu distributed uniformly all along the rod. The overlaid (Au+Cu) image indicates that the rod is rich in Cu phase and quantitative analysis shows Cu is 76% and Au is 24 % (Figure 4.5). The STEM image in Figure 4.4B acquired from a sample collected at 30 min, clearly shows the formation of a hollow junction (neck) region at the nanorod center, with high contrast on the ends. The elemental maps reveal that the ends are rich in Cu with a layer of Au phase on surface as clearly seen in the overlaid image. This is also consistent with the HRTEM data in Figure 4.3E and 4.3F. To further confirm the hollowness of the junction, line scans have been performed on the intermediate and the results are summarized in Figure

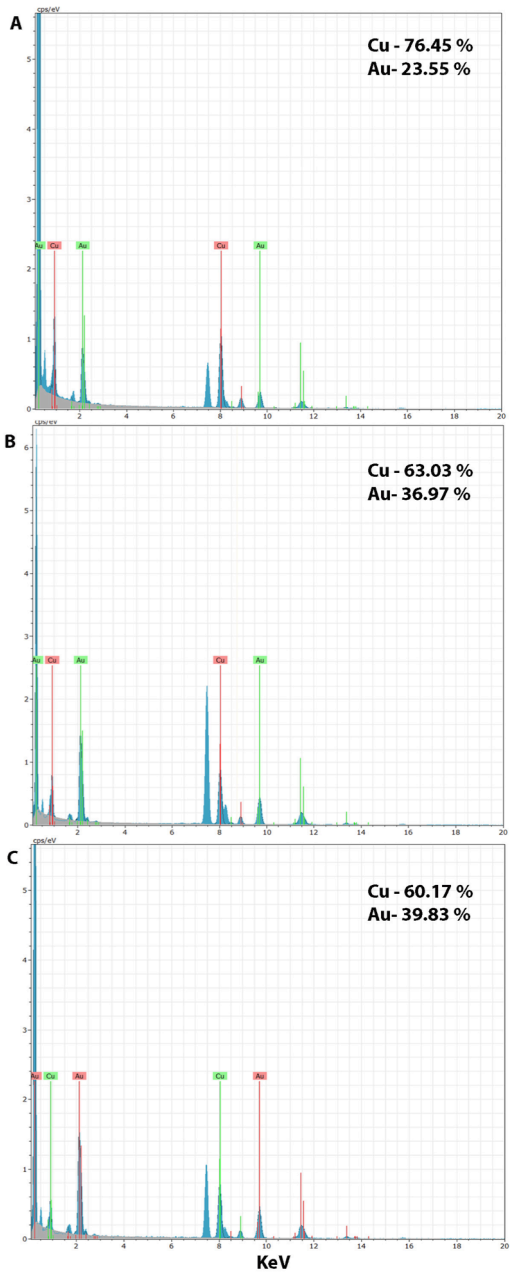

Figure 4.5. EDS of initial $AuCu_3$ rods (A) and samples separated after 30 min (B), and 1 hr (C) after adding $HAuCl_4$.

4.6. The Cu and Au distribution along the longitudinal direction (see line scan 1 in Figure 4.6) shows a dip at the center of the rod, due to the hollowness in the junction. The line

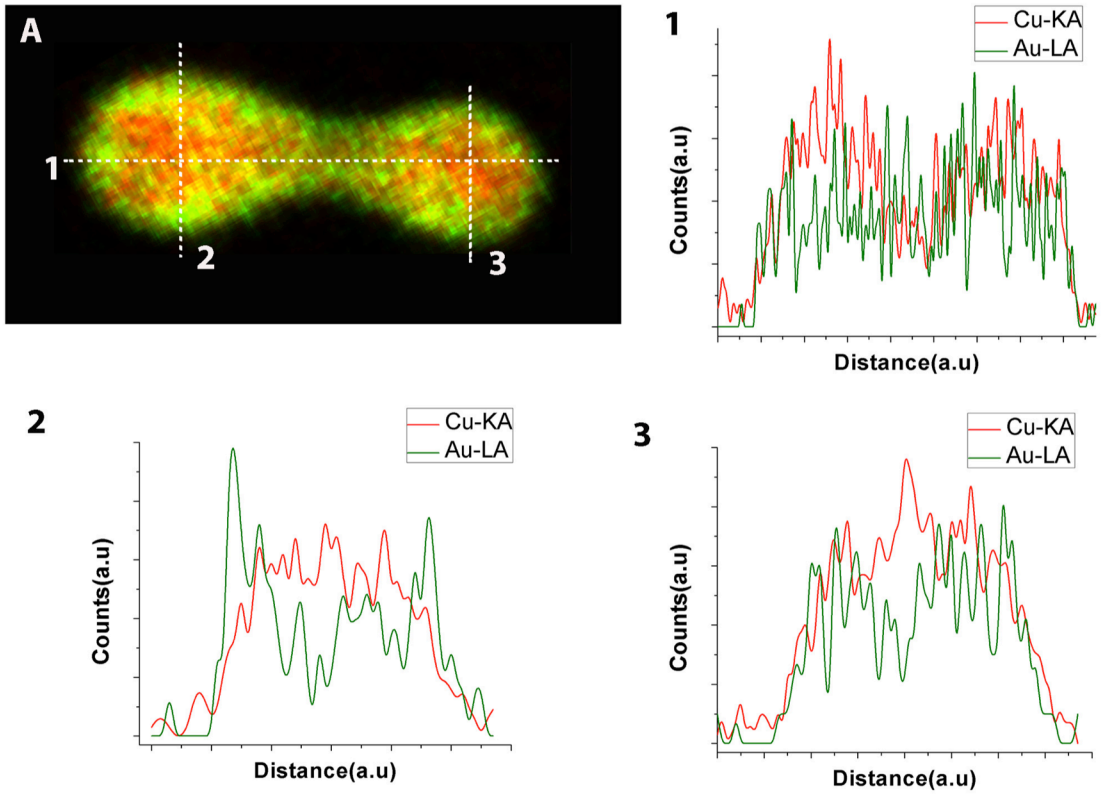

Figure 4.6. Line scans performed on the intermediate sample separated at 30 min of reaction. (A) EDX mapping image. Line scans along (1) the longitudinal axis of the intermediate and (2 and 3) along the transverse direction at the two ends of the intermediate. Longitudinal scan clearly indicates hollow junction and transverse scans show Au@AuCu structure at the ends.

scan also indicates that tips are rich in Cu compare to Au. The transverse line scans on the tips (2, 3 in Figure 4.6) clearly show that there is an Au shell on the surface, making the ends of the intermediate have an AuCu@Au core@shell-like structure. These results are also consistent with HRTEM measurements in Figure 4.3F. The EDS quantification revealed that the overall content of Au increased from 24% to 37% in the intermediate compared to initial template, due to the replacement of Cu by Au (Figure 4.5). The

intermediate acquired at 45 min is a mixture of peanut-shaped and spheroidal particles. The hollow junction in the peanut-shaped particles became narrower as shown in STEM image in Figure 4.4C. Figure 4.4D shows the EDX maps of spheroidal particles obtained after 1 hr reaction time. The maps show the particles are composed of Au-Cu alloy in the center, and covered with Au shell on the outside (also see Figure 4.7) consistent with HRTEM image in Figure 4.3I. The structure is similar to the ends of the peanut-shaped

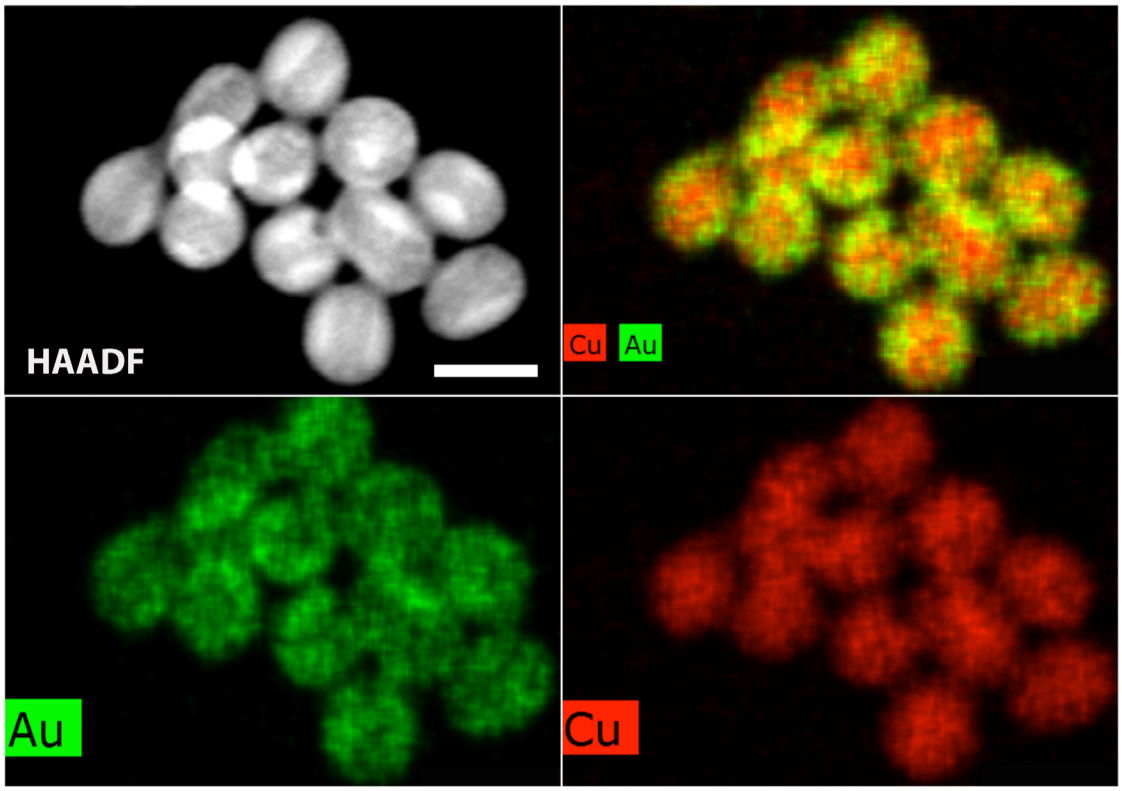

Figure 4.7. EDX elemental mapping of the sample obtained after 1 hr of reaction. The overlaid image clearly indicates the Au@AuCu structure similar to the ends of the intermediate separated at 30 min.

particle, confirming that final products are resulted from the breaking of the peanut-shaped particles. The Au shell prevented the Cu in the center from being replaced continuously; therefore, the final products obtained are AuCu@Au core@shell spheroids. The TEM and EDX analysis revealed an unusual intermediate where a hollow junction

was formed, which is also further confirmed from the line scans in Figure 4.6. We believe that the hollowness must involve the diffusion of Cu atoms to the ends of the nanorods.

4.3.2 GRR Mechanism

The UV-Vis, EDX and HRTEM characterizations suggest that oxidation of Cu by $HAuCl_4$ and vacancy mediated diffusion dominates the structural transformation of the nanorod at different stages of the reaction. We hypothesize that interplay between GRR and Kirkendall effect during reaction leads to the peanut-shaped intermediates with a hollow junction before the nanorods break into spheroids. The important steps are illustrated in scheme 1. Initially (step 1), when $HAuCl_4$ precursor is added into the solution, the Cu atoms on the surface of nanorod get oxidized. Simultaneously, Au (III) is reduced to Au (0) and deposited at the sites where galvanic exchange takes place at a stoichiometric ratio of 3: 2 (Cu: Au).[44] Tips of nanorods are usually more reactive than the sides as demonstrated in the previous studies.[45, 46] In particular for polycrystalline nanorods, tips are demonstrated as highly reactive sites due to their high curvature and surface energy. For

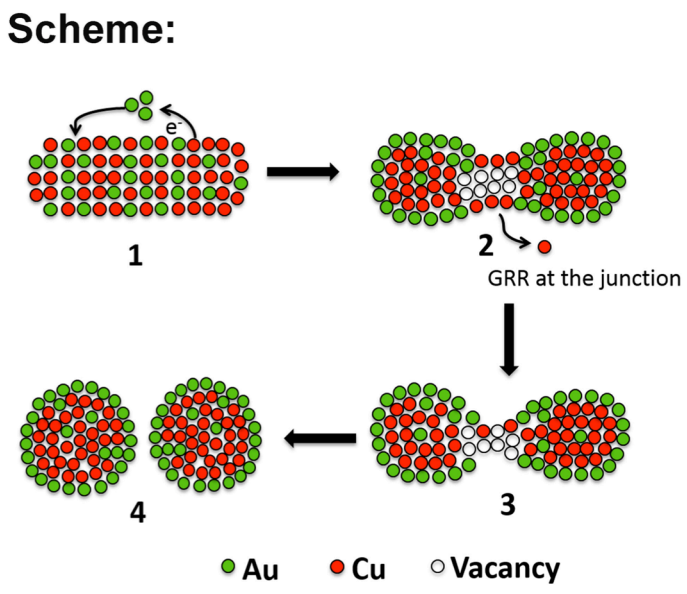

Scheme 4.1. Mechanism of morphological transformation of $AuCu_3$ alloy nanord rod into alloy spheroids via asymmetric peanut shaped intermediate with a hollow junction.

example, the groups of Song and Vaia,[47] [48] have shown that in the synthesis of Au/Ag nanorods using Au nanorods as template, Ag preferentially grew on the tips of the Au nanorods. Hence, we assume the more reactive tips of the initial template leads to faster GRR at the tips. This creates more vacancies at the tips than the sides causing diffusion of both surface and bulk Cu atoms from the center to the tips (step 2). Thus, dumbbell-shaped structure with a hollow narrow junction is formed, as seen in the TEM images in Figure 4.3B. Further oxidation happens at the center of the rod, where the surface is more exposed to Au precursor in the solution compared to the tips (as they are sealed by Au, due to faster GRR initially). The continuing removal of atoms from the surface of the center, results in the narrowing of the junction part (step 3). The hollow junction portion is further weakened by on-going galvanic replacement, leading to the breakage of the dumbbell shaped particle into spheroids (step 4). Overall, the morphological transformation from alloy nanorod to nearly core shell spheroidal particle happens through a dumbbell-shaped intermediate with a hollow junction, governed by the relative rate of GRR and Kirkendall effect during reaction.

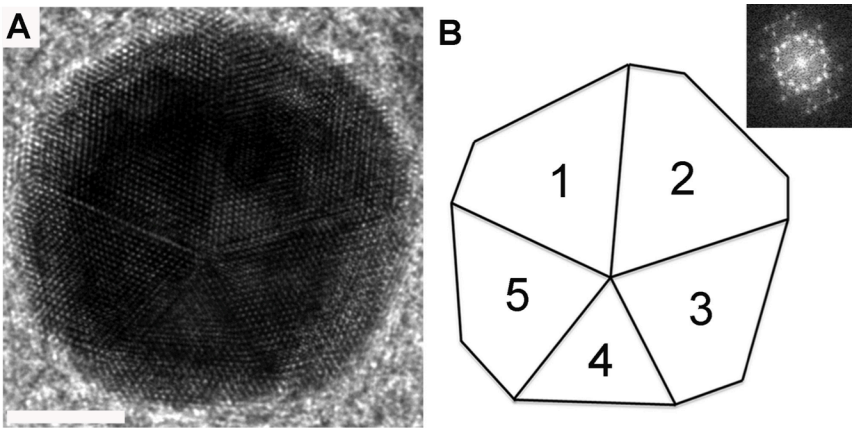

Figure 4.8. (A) HRTEM image of a standing $AuCu_3$ alloy nanorod, showing penta twinned structure. (B) Is the representation of (A). The insert represents the diffraction pattern of A, indicating the nanorod is polycrystalline. The scale bar = 5 nm.

In order to

understand the tip preferred galvanic exchange, HRTEM analysis of the tips have been performed on standing rods facing the electron beam[49] and the results are summarized in Figure 4.8. The rods are made to stand on the TEM grid by drop casting a highly

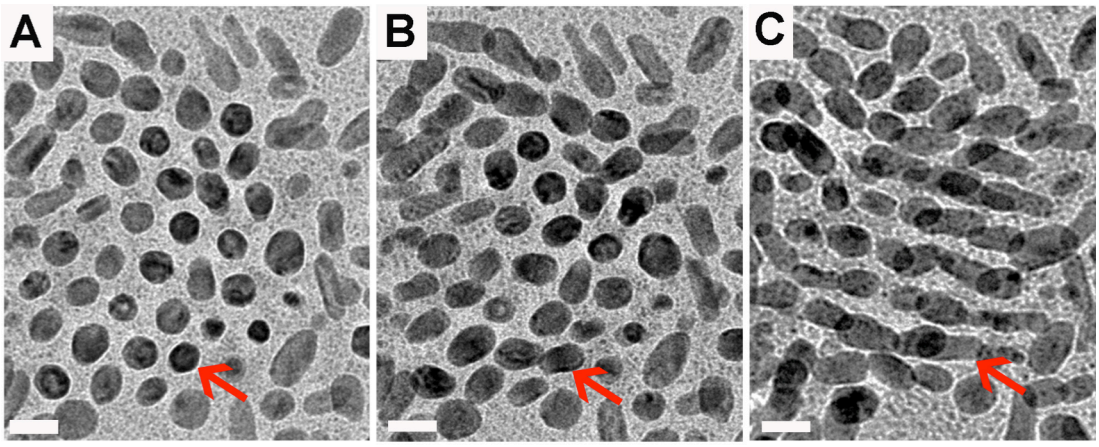

Figure 4.9. $AuCu_3$ nanorod tip analysis. (A-C) TEM images of a standing $AuCu_3$ alloy nanorods viewed by rotating the stage to different angles, with red arrow pointing to one particular rod.

concentrated solution. Titling the sample stage and looking at the tail portion confirm the rods are indeed standing up, as shown in Figure 4.9. The red arrow in Figure 4.9A-C indicates the transformation of spherical particle into a structure with tail as shown in Figure 4.9C, as the stage is tilted, indicating that Figure 4.8A shows the HRTEM image of a standing rod. Figure 4.8B is representation of 4.8A, with the inset showing the FFT pattern. Figure 4.8B reveals that the nanorod is polycrystalline in nature. Specifically, it has a penta-twinned structure with each twin plane having more than one facet as shown in Figure 4.10. Figure 4.10A is the standing rod, with tip facing the beam as shown in figure 4.10C and 4.10B is the representation of 4.10A showing the major facets of each crystal. The crystal facets are figured out from the FFT patterns shown in the figure 4.10

from 1-5, representing each crystal. The (200) facet indicated by red sarrow in each crystal is found to bisect the major plane, indicating that all major planes of each crystal are high energy (200) facets. The twin boundaries were known to have unfilled lattice spaces, which make them more reactive than crystallites due to strain effect.[50, 51] In

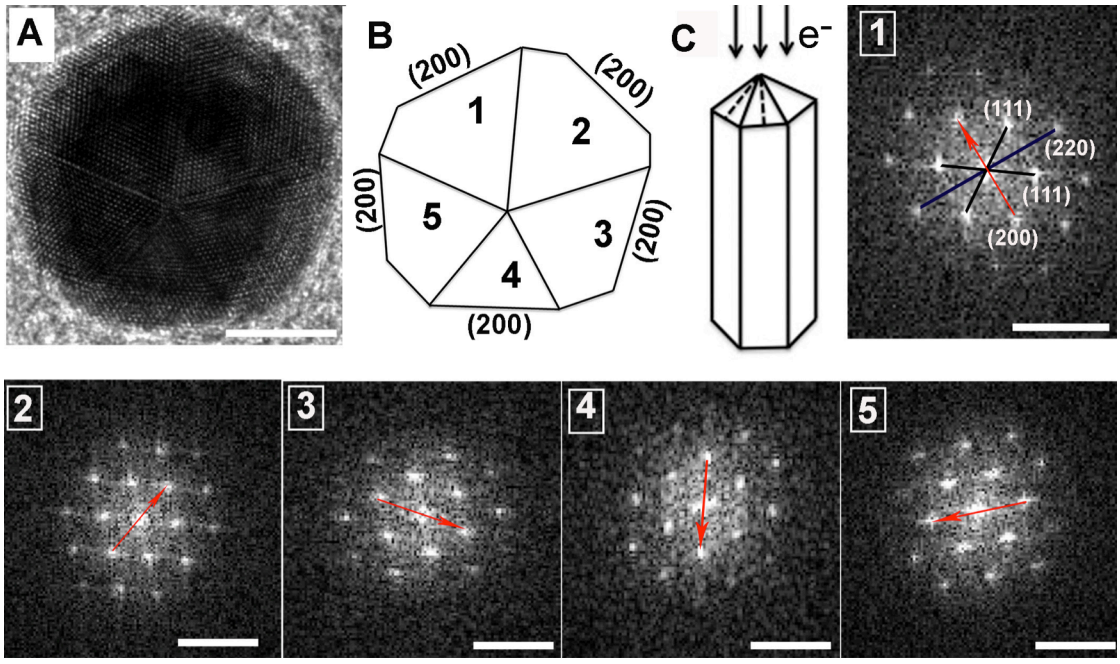

Figure 4.10. $AuCu_3$ nanorod tip analysis. (A) HRTEM image of a standing $AuCu_3$ alloy nanorod. (B) Representation of (A), showing penta twinned structure with major (200) facets. (C) Representation of a standing nanorod and electron beam direction. (1-5) Corresponding FFT patterns of each twin plane represented in (B). Red arrow indicates (200) direction in each plane. The scale bar for HRTEM= 5 nm and FFT patterns= 10.1 nm

addition, the tips of the nanorod have higher curvatures than the sides.[52, 53] These factors make the reactivity of the tips of the nanorod higher than that of the sides; thus, GRR is faster at the tips than the sides at initial stage of there action

4.3.3 Single Particle Scattering

Although a significant amount of information has been obtained regarding the reaction process through characterization of the intermediates using HRTEM and EDS, little is

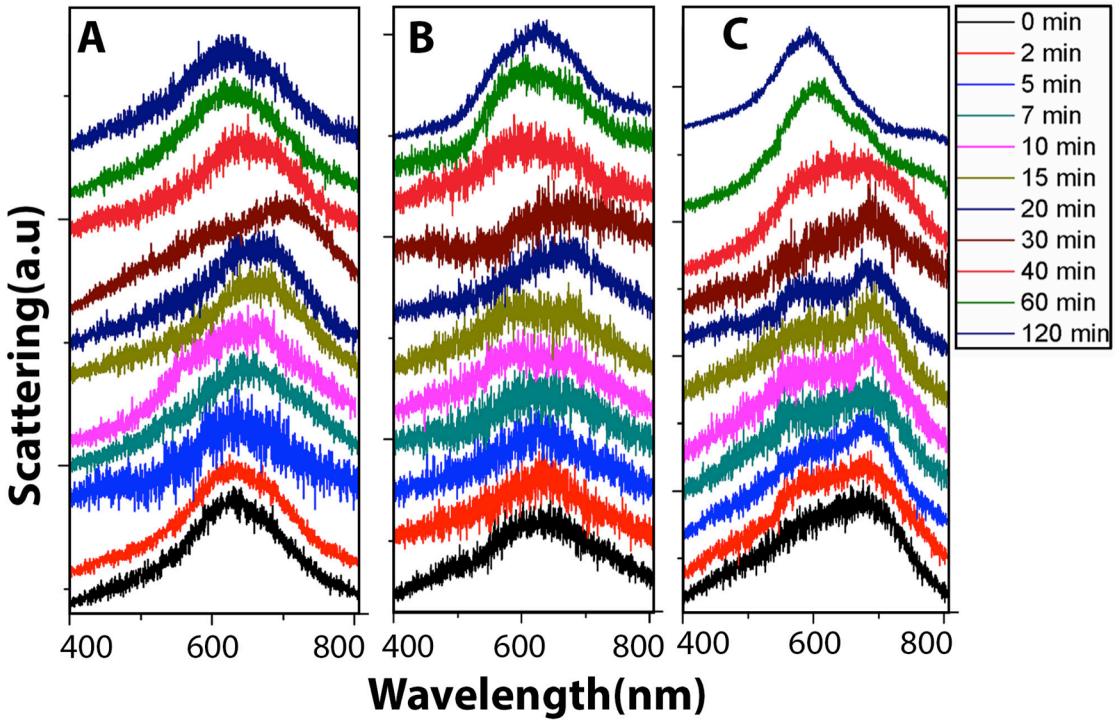

Figure 4.11. In situ dark field scattering spectra of Au-Cu alloy nanorods during galvanic replacement with $HAuCl_4$. A, B, C are spectra of three individual nanorods during reaction, showing an initial red shift with a shoulder followed by a blue shift.

known about what occurs during the initial stages of the reaction. It is still unclear when exactly the hollow junction forms in the structure. Specifically, we question whether the junction forms first followed by hollowing, vice-versa, or if the junction creation and hollowing is a simultaneous process. In order to understand this and capture the critical transition points in the reaction, in situ studies are preferred. In this work, single particle scattering spectroscopy is used to monitor the reaction *insitu*. Single particle studies provide information of the reaction kinetics of individual particles, which are smeared out in the ensemble measurements as shown by the broad peaks in Figure 4.1.[35, 54-55] To

perform the experiment, small amount of dilute $AuCu_3$ nanorod templates were drop casted on a coverslip to allow single particle measurements. The single particle scattering spectra of selected nanorods were monitored at regular time intervals for 2 hrs after the addition of 1 mL $HAuCl_4$. The spectral evolution with time for representative individual nanoparticles is shown in Figure 4.11 and Figure 4.12. The starting template, $AuCu_3$ nanorods display a strong longitudinal LSPR peak at ~ 630 to 680 nm depending on their aspect ratio. After the injection of the Au precursor, all the spectra show a common trend of a red shift, accompanied by changes in the spectral features as seen in Figure 4.11 and Figure 4.12. An additional peak at around 600 nm appears in the 10-min spectrum in Figure 4.10A, and in the 10-20 min spectra in 4.10B. Also, a clear shoulder shows up in the spectra from 2-30 min in 4.10C and grows stronger as the reaction progresses. The extent of the peak shifts and the relative intensity of the additional peak

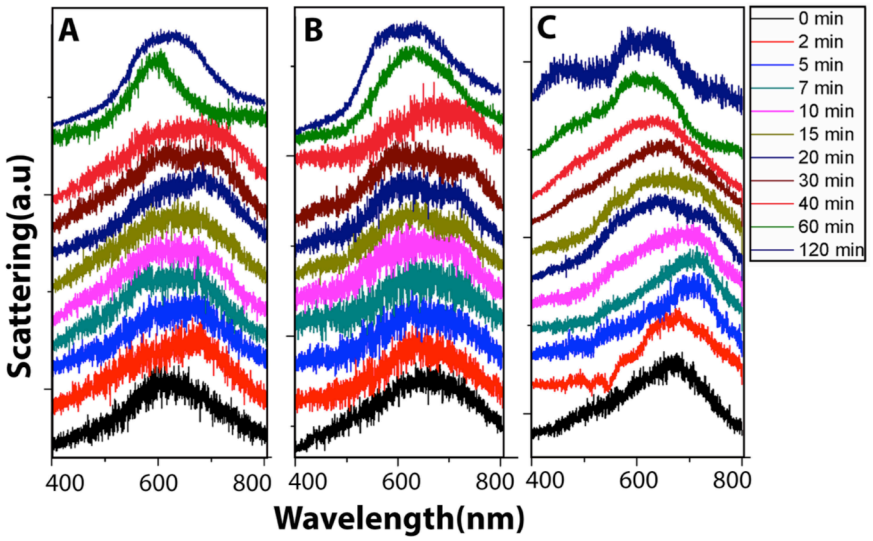

Figure 4.12. In situ dark field scattering spectra of Au-Cu alloy nanorods during galvanic replacement with $HAuCl_4$. A, B, C are traces of three individual nanorods during galvanic exchange, showing initial red shift with a shoulder around 600 nm. The shoulder grows stronger at later stages.

are different for individual nanorods due to the variations in reaction kinetics and morphology of the individual nanorods. At ~30-40 min of reaction, a sudden blue shift in the spectra was observed for all the nanorods studied. After this transition event, some spectra showed a small blue shift for up to 60 min of the reaction. No significant changes were observed when the reaction is continued to 120 min. From the above analysis, two transition events are identified: one occurred at ~10-15 mins of reaction, where a shoulder peak at ~ 600 nm appeared in the spectra; the other one took place at ~30-40 mins of reaction, where the spectra showed a blue shift in the peak wavelength. We

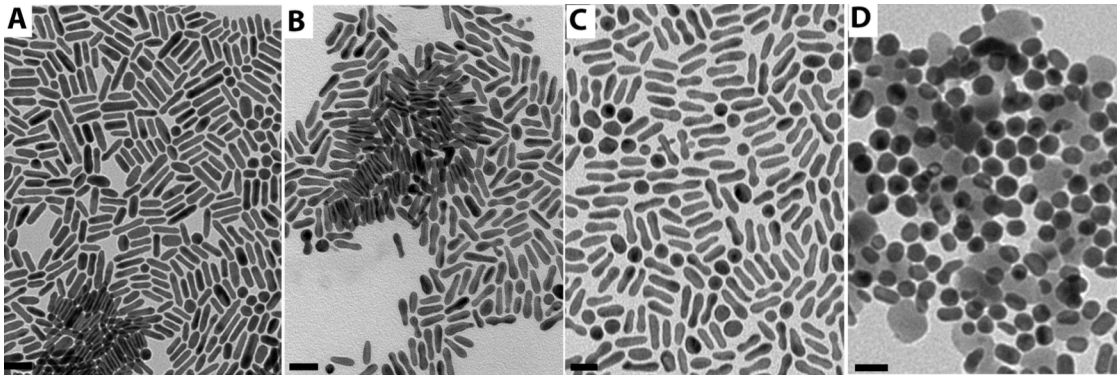

Figure 4.13. TEM images of the samples, (A) Initial $AuCu_3$ nanorods, (B), (C) and (D) are samples obtained after 10 min, 20 min and 45 min of galvanic replacement reaction performed on Cu grid to represent the GRR on glass substrate with $HAuCl_4$ precursor dissolved in water. The precursor was removed using a kim wipe at the regular time intervals and later allowed to dry for TEM measurements. The intermediates and final products morphology obtained here are similar to solution phase GRR. This indicates that the GRR on substrate is similar to that of solution phase and dissolving Au precursor in water has no effect on reaction mechanism. The scale bar= 50 nm

believe these transition events are related to the morphological changes in the nanorods during GRR. The red shift in the single particle spectra followed by blue shift at a later reaction stage is consistent with the trend of the spectral shift in the ensemble

measurements (in Figure 1 and 2). To ensure the morphological changes in the nanoparticles during the single particle measurements reflect what happened in the solution phase, GRR was performed on $AuCu_3$ nanorods deposited on TEM grid to represent the GRR on glass substrate with $HAuCl_4$ precursor dissolved in water. The precursor was removed using a kim wipe at the regular time intervals and later allowed to dry for TEM measurements. The intermediates and final products morphology obtained here are similar to solution phase GRR as shown in Figure 4.13. This indicates that the GRR on substrate is similar to that of solution phase and dissolving Au precursor in water has no effect on reaction mechanism. Same structural changes observed in Figure 4.13, showing that the solvent and substrate did not affect the GRR reaction pathway. To understand the in situ spectral changes in the nanorods during GRR, electrodynamics

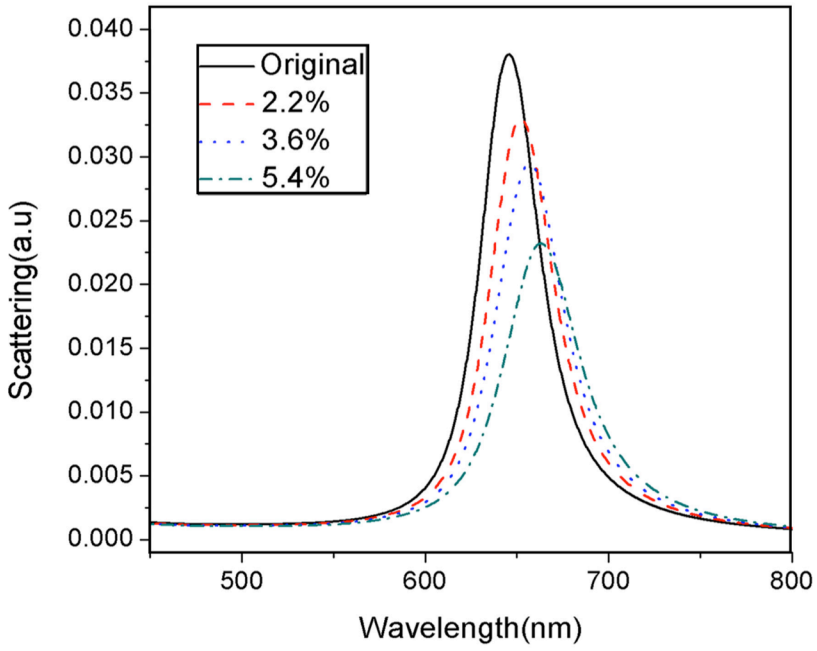

Figure 4.14. Calculated scattering spectra of the $AuCu_3$ nanorod (black) and after different extents of galvanic replacement on the surface of the nanorod, Red: 2.2%, blue: 3.6%, and Cyan: 5.4%. Galvanic replacement on the surface at the initial stages only causes red shift in the longitudinal mode of the nanorod.

simulations were performed using the discrete dipole approximation (DDA) method.[39] In the calculations, we assume the $AuCu_3$ rod is 20 nm in length and 10 nm in diameter in order to match the measured resonance wavelength in the experimental spectra. We have varied the Au/Cu ratio according to the experimental conditions in the simulations and the spectrum profiles are changed only slightly, which has been shown in our previous

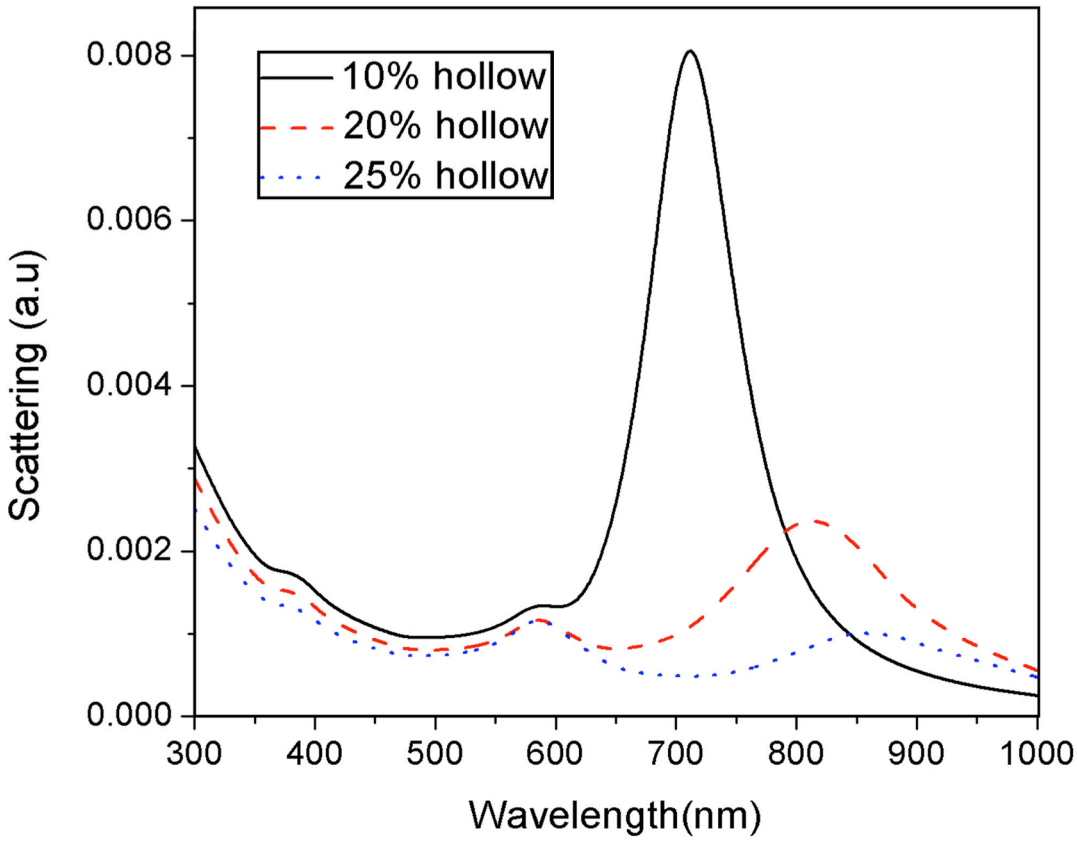

Figure 4.15. Calculated scattering spectra of $AuCu_3$ nanorod of varied hollowness at the center. Black: 10%, red: 20%, blue: 25%. The scattering spectra displayed a shoulder around 600 nm due to the hollow junction at the center of the rod.

work.[42] Initially, the faster rate of Cu oxidation and replacement by Au leads to small vacancy sites near the surface of the rod and the calculations with similar configurations

show a red shift in the LSPR of the nanorod as shown in Figure 4.14, as observed in the experiments. As the reaction progresses, diffusion of Cu to the tips of the nanorod leaves vacancy sites in the center. In the theoretical calculations, a number of small vacancies are added randomly to the nanorod. When vacancies are added in the center of the nanorod, an additional blue shoulder/peak appears in the spectra as seen in Figure 4.15. These theoretical findings are consistent with the TEM and EDX images of the intermediate stage of peanut-shaped particles. The blue shoulder is due to the enhanced transverse mode excitation of the deformed nanorod and the coupling between two ends of the rod. We found that the volume of the vacancy has to be above 10% of the volume of the nanorod for the blue peak to appear. The relative intensity of the blue peak (~ 600 nm) to the red

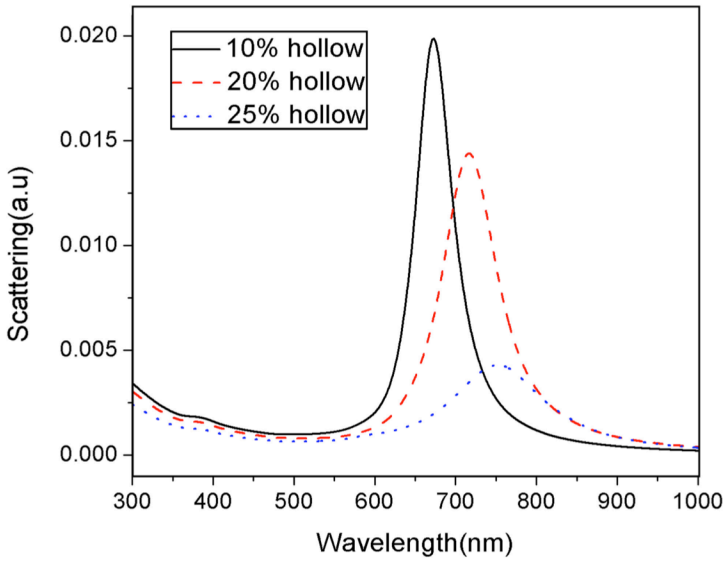

Figure 4.16. Calculated scattering spectra of the $AuCu_3$ nanorod with different %volumes of hollowness at random locations, black: 10%, red: 20%, and blue: 25%. Hollowing at random locations other than center of the nanorod only cause red shift in the longitudinal mode, but doesn't cause peak splitting. This indicates the experimentally observed peak splitting in in situ experiments was due to creation of hollow region exactly at the center of the nanorod resulting from tip preferential Cu diffusion.

peak (at ~ 680 nm) increases when the volume of the vacancy increases. In contrast, if vacancies are created randomly in the entire rod, the LSPR will only red shift, but does not show the additional feature at ~ 600 nm as shown in Figure 4.16. The red shift might be also caused due to formation of the junction at the center due to surface atom diffusion as mentioned before. Also, we observed that when increasing the hollowness of the junction, the splitting between the two plasmon modes is more significant, and the intensity decreases. At 25% hollowness of the junction, the red peak is likely shifted out of the detection range of the CCD camera we used. This would explain why the LSPR of the particle at ~30-40 mins in Figure 4.11 appears to be a single blue shifted peak. As the reaction continues, the nanoparticle breaks into spheroids and grows in size. Since the nanoparticles observed in the in-situ measurement are immobilized on the substrate, there will still be strong coupling between the two spheroidal particles when they are close to each other.[56, 57] This coupling causes a discrepancy in the peak positon of the nanospheroids in solution (~ 550 nm, cyan line in Figure 4.17), and on substrate (~ 600

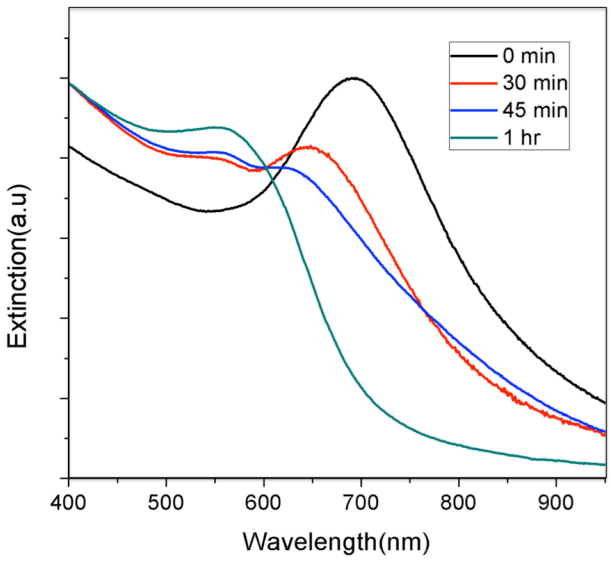

Figure 4.17. Ensemble extinction spectra of initial $AuCu_3$ nanorods (black) and samples separated at 30 min (red), 45 min (blue) and 1 hr (scion). The blue shift followed by increase in peak intensity at 570 nm indicates formation of Au Cu alloy nanoparticles

nm). The experimental and theoretical optical studies support our hypothesis of a nanorod transformation mechanism. That is, the GRR dominates the reaction at the beginning, leading to narrowing of the nanorod center. The Kirkendall effect becomes more dramatic as the reaction continues, resulting in hollowness of the junction. At last, GRR at the center of the intermediates breaks the nanorod into spheroids.

4.3.4 Hollow Junction Dependent Optical Properties

Junction dependent optical properties of nanoparticles are of high interest currently due to their potential applications in photonic devices, non-linear spectroscopies and catalysis.[53-54] As previously reported, when two metal particles are connected by a conductive junction, two plasmon modes were observed.[58-60] One is a charge transfer plasmon mode (CTP) at a longer wavelength (similar to longitudinal mode), and the other is a bonding dipolar plasmon (BDP) mode at a shorter wavelength. The strength and separation between these two modes depends on the conductivity and dimensions of the junction. Here, we show that it will also depend on the internal structure (hollowness) of the junction. In order to further examine the effect of hollowness of junction on the plasmon modes, we calculated the scattering spectra of a dumbbell shaped particle (end diameter= 8 nm, total length=21 nm) with a junction diameter of 6 nm as shown in Figure 18A. The length of the junction was fixed as 5 nm, while the hollowness D_{in} was varied from 0 to 5 nm as showed in Figure 18. When the junction was solid (D_{in} = 0 nm, black spectra), the scattering spectrum of nanorod displayed a single peak from the longitudinal mode of the nanorod, even though the junction was present. When the D_{in} was increase to 2 nm, the spectra red shifted (red spectra) compared to the solid junction. Further increase in D_{in} only by 1 nm resulted in the additional plasmon mode along with a red shift of ~60 nm

(blue spectra) as in Figure 18B. When D_{in} was increased to 4 nm, a drastic red shift was accompanied by reduction in the intensity. The spectrum displayed multiple shoulder peaks. Further increasing the D_{in} to 5 nm resulted in total loss of the scattering intensity in the visible wavelength, as shown in Figure 18B (pink spectrum). The calculations

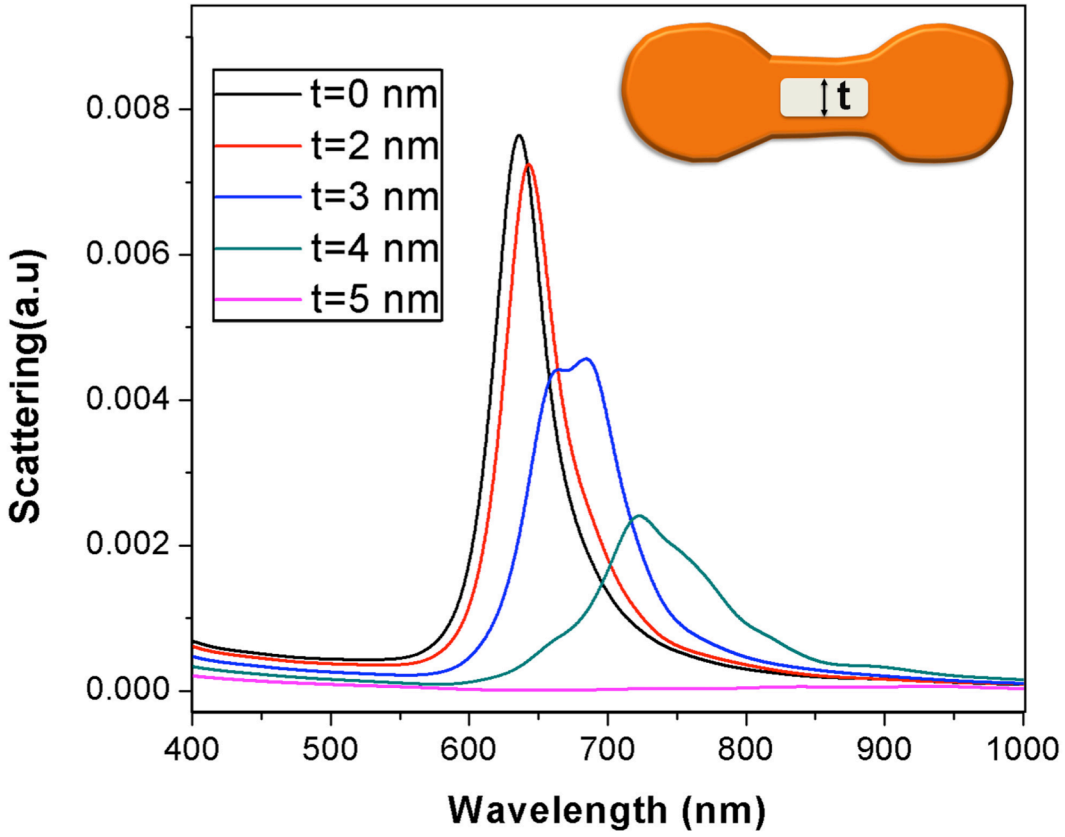

Figure 4.18. (A) Schematic illustration of a dumbbell shaped rod with a hollow junction and (B) corresponding scattering spectrum of a rod with a junction of thickness 6 nm and length 5 nm, containing hollow portion of varying thickness D_{in}. Black: D_{in} = 0 nm, red: D_{in} = 2 nm, blue: D_{in} = 3 nm, sea green: D_{in} = 4 nm, pink: D_{in} = 5 nm.

show the extreme sensitivity of the LSPR of the nanoparticle to the internal structure of the junction.

4.4 Conclusions

In summary, we demonstrated that when GRR is performed with $AuCu_3$ nanorods and $HAuCl_4$, different products can be obtained by simply changing the concentrations of $HAuCl_4$. The change in rates of GRR is the key that determines the morphology of the products. HRTEM, EDX, and in situ dark field scattering reveals the formation of a unique intermediate with a hollow junction and dumbbell shape during GRR. DDA simulations showed that the creation of the hollow junction (of at least 10% volume of the rod) at the center of the nanorod caused peak splitting supporting the experimental explanation of the reaction mechanism. Theoretical studies also showed that small changes in the hollowness of the junction would change the scattering spectrum significantly. Hence, single particle scattering can be used as an exquisite tool to probe the conductance and the internal structure of the nanoscale junctions.

4.5 Reference

1. M. B. Cortie and A. M. McDonagh, *Chem. Rev.*, 2011, **111**, 3713-3735.
2. M. G. Blaber, M. D. Arnold and M. J. Ford, *J. Phys.: Condens. Matter*, 2010, **22**, 143201.
3. A. Walther and A. H. E. Müller, *Chem. Rev.*, 2013, **113**, 5194-5261.
4. D. Wang and Y. Li, *Adv. Mater.*, 2011, **23**, 1044-1060.
5. C. Chen, Y. Kang, Z. Huo, Z. Zhu, W. Huang, H. L. Xin, J. D. Snyder, D. Li, J. A. Herron, M. Mavrikakis, M. Chi, K. L. More, Y. Li, N. M. Markovic, G. A. Somorjai, P. Yang and V. R. Stamenkovic, *Science*, 2014, **343**, 1339-1343.
6. D. M. Alonso, S. G. Wettstein and J. A. Dumesic, *Chem. Soc. Rev.*, 2012, **41**, 8075-8098.
7. S. Guo, S. Zhang, X. Sun and S. Sun, *J. Am. Chem. Soc.*, 2011, **133**, 15354-15357.
8. R. He, Y.-C. Wang, X. Wang, Z. Wang, G. Liu, W. Zhou, L. Wen, Q. Li, X. Wang, X. Chen, J. Zeng and J. G. Hou, *Nat. Commun.*, 2014, **5**, 4327-4332.
9. M. S. Yavuz, Y. Cheng, J. Chen, C. M. Cobley, Q. Zhang, M. Rycenga, J. Xie, C. Kim, K. H. Song, A. G. Schwartz, L. V. Wang and Y. Xia, *Nat. Mater.*, 2009, **8**, 935-939.
10. F. Wang, C. Li, H. Chen, R. Jiang, L.-D. Sun, Q. Li, J. Wang, J. C. Yu and C.-H. Yan, *J. Am. Chem. Soc.*, 2013, **135**, 5588-5601.
11. C. J. DeSantis and S. E. Skrabalak, *Langmuir*, 2012, **28**, 9055-9062.
12. S. Zhou, G. S. Jackson and B. Eichhorn, *Adv. Funct. Mater.*, 2007, **17**, 3099-3104.
13. R. G. Weiner, A. F. Smith and S. E. Skrabalak, *Chem. Commun.*, 2015, **51**, 8872-8875.
14. J. Erlebacher, M. J. Aziz, A. Karma, N. Dimitrov and K. Sieradzki, *Nature*, 2001, **410**, 450-453.
15. G. G. Li, E. Villarreal, Q. Zhang, T. Zheng, J.-J. Zhu and H. Wang, *ACS Applied Materials & Interfaces*, 2016, **8**, 23920-23931.
16. Y. Sun, *Natl. Sci. Rev.*, 2015, **2**, 329-348.
17. Y. Hu, Y. Liu, Z. Li and Y. Sun, *Adv. Funct. Mater.*, 2014, **24**, 2828-2836.

18. X. Xia, Y. Wang, A. Ruditskiy and Y. Xia, *Adv. Funct. Mater.*, 2013, **25**, 6313-6333.
19. S. F. Tan, G. Lin, M. Bosman, U. Mirsaidov and C. A. Nijhuis, *ACS Nano*, 2016, **10**, 7689-7695.
20. B. Goris, L. Polavarapu, S. Bals, G. Van Tendeloo and L. M. Liz-Marzán, *Nano Lett.*, 2014, **14**, 3220-3226.
21. Y. Sun and Y. Xia, *Science*, 2002, **298**, 2176-2179.
22. E. González, J. Arbiol and V. F. Puntes, *Science*, 2011, **334**, 1377-1380.
23. H. Jing and H. Wang, *Chem. Mater.*, 2015, **27**, 2172-2180.
24. G. S. Métraux, Y. C. Cao, R. Jin and C. A. Mirkin, *Nano Lett.*, 2003, **3**, 519-522.
25. M. H. Oh, T. Yu, S.-H. Yu, B. Lim, K.-T. Ko, M.-G. Willinger, D.-H. Seo, B. H. Kim, M. G. Cho, J.-H. Park, K. Kang, Y.-E. Sung, N. Pinna and T. Hyeon, *Science*, 2013, **340**, 964-968.
26. Y. Sun, B. T. Mayers and Y. Xia, *Nano Lett.*, 2002, **2**, 481-485.
27. L. Polavarapu, D. Zanaga, T. Altantzis, S. Rodal-Cedeira, I. Pastoriza-Santos, J. Pérez-Juste, S. Bals and L. M. Liz-Marzán, *J. Am. Chem. Soc.*, 2016, **138**, 11453-11456.
28. Y. Sun and Y. Xia, *J. Am. Chem. Soc.*, 2004, **126**, 3892-3901.
29. W. Wang, M. Dahl and Y. Yin, *Chem. Mater.*, 2013, **25**, 1179-1189.
30. X. Li, Q. Chen, I. McCue, J. Snyder, P. Crozier, J. Erlebacher and K. Sieradzki, *Nano Lett.*, 2014, **14**, 2569-2577.
31. P. Chen, X. Zhou, N. M. Andoy, K.-S. Han, E. Choudhary, N. Zou, G. Chen and H. Shen, *Chem. Soc. rev.*, 2014, **43**, 1107-1117.
32. L. Shi, C. Jing, W. Ma, D.-W. Li, J. E. Halls, F. Marken and Y.-T. Long, *Angew. Chem. Int. Ed.*, 2013, **52**, 6011-6014.
33. Y. Liu and Y. Sun, *Nanoscale*, 2015, **7**, 13687-13693..
34. C. Novo, A. M. Funston and P. Mulvaney, *Nat. Nano.*, 2008, **3**, 598-602.
35. Y. Park, C. Lee, S. Ryu and H. Song, *J. Phys. Chem. C*, 2015, **119**, 20125-20135.
36. J. G. Smith, I. Chakraborty and P. K. Jain, *Angew. Chem. Int. Ed.*, 2016, **55**, 9979-9983.
37. J. G. Smith, Q. Yang and P. K. Jain, *Angew. Chem. Int. Ed.*, 2014, **53**, 2867-2872.

38. S. Chen, S. V. Jenkins, J. Tao, Y. Zhu and J. Chen, *The J. Phys. Chem. C*, 2013, **117**, 8924-8932.
39. T. B. Draine, *Astrophys. J.*, 1988, **333**, 848-872.
40. E. D. Palik, *Handbook of optical constants of solids*, Academic Press, Boston, 1988.
41. M. Chandra, A.-M. Dowgiallo and K. L. Knappenberger, *J. Am. Chem. Soc.*, 2010, **132**, 15782-15789.
42. N. R. Sieb, N.-c. Wu, E. Majidi, R. Kukreja, N. R. Branda and B. D. Gates, *ACS Nano*, 2009, **3**, 1365-1372.
43. S. Thota, S. Chen and J. Zhao, *Chem. Commun*, 2016, **52**, 5593-5596.
44. S. Thota, S. Chen, Y. Zhou, Y. Zhang, S. Zou and J. Zhao, *Nanoscale*, 2015, **7**, 14652-14658.
45. P. D. Cozzoli, T. Pellegrino and L. Manna, *Chem. Soc. rev.*, 2006, **35**, 1195-1208.
46. R. Costi, A. E. Saunders and U. Banin, *Angew. Chem. Int. Ed.*, 2010, **49**, 4878-4897.
47. D. Seo, C. I. Yoo, J. Jung and H. Song, *J. Am. Chem. Soc.*, 2008, **130**, 2940-2941.
48. K. Park and R. A. Vaia, *Adv. Mater.*, 2008, **20**, 3882-3886.
49. E. Carbó-Argibay, B. Rodríguez-González, S. Gómez-Graña, A. Guerrero-Martínez, I. Pastoriza-Santos, J. Pérez-Juste and L. M. Liz-Marzán, *Angew. Chem. Int. Ed.*, 2010, **49**, 9397-9400.
50. B. T. Sneed, A. P. Young and C.-K. Tsung, *Nanoscale*, 2015, **7**, 12248-12265.
51. S. Patala, L. D. Marks and M. Olvera de la Cruz, *J. Phys. Chem. C*, 2013, **117**, 1485-1494.
52. J. Wu, L. Qi, H. You, A. Gross, J. Li and H. Yang, *J. Am. Chem. Soc.*, 2012, **134**, 11880-11883.
53. H. Katz-Boon, M. Walsh, C. Dwyer, P. Mulvaney, A. M. Funston and J. Etheridge, *Nano Lett.*, 2015, **15**, 1635-1641.
54. Y. Park, C. Lee, S. Ryu and H. Song, *J. Phys. Chem. C*, 2015, **119**, 20125-20135.
55. A. F. Smith, R. G. Weiner, M. M. Bower, B. Dragnea and S. E. Skrabalak, *J. Phys. Chem. C*, 2015, **119**, 22114-22121.

56. Y. Sun, J. J. Foley, S. Peng, Z. Li and S. K. Gray, *Nano Lett.*, 2013, **13**, 3958-3964.
57. Y. Hu and Y. Sun, *J. Am. Chem. Soc.*, 2013, **135**, 2213-2221.
58. F. Wen, Y. Zhang, S. Gottheim, N. S. King, Y. Zhang, P. Nordlander and N. J. Halas, *ACS Nano*, 2015, **9**, 6428-6435.
59. S. Lerch and B. M. Reinhard, *Adv. Mater.*, 2016, **28**, 2030-2036.
60. T. P. Rossi, A. Zugarramurdi, M. J. Puska and R. M. Nieminen, *Phys. Rev. Lett.*, 2015, **115**, 236804.

Chapter 5. CdS Length-Dependent Trap State Emissions in Ag-CdS Metal-Semiconductor Hybrid Nanorods

5.1 Introduction

Hybrid nanoparticles are formed by combination of two different materials into a single nanosystem in a controlled manner. The synergistic interaction between the components often lead to enhanced catalytic and optical properties compared to the individual components.[1-3] Hybrid metal-semiconductor nanostructures have attracted lot of attention in the recent years due to their unique electronic properties.[4] For example, the overlap of metal's Fermi level with the electronic states of semiconductor results in efficient charge separation at the metal-semiconductor interface, making them promising candidates for photo catalysis,[5-7] photo electrochemical cells[8] and solar cell applications.[8, 9] Hybrid nanorods also play a key role in charge transport, hence can be used as key component in novel nanoelectronic devices.[10-13] These properties are size, shape and composition dependent, hence they can be fine-tuned over a wide range for desired applications by bottom up synthetic control.

Many hybrid nanostructures with different metal, semiconductor components were fabricated after the pioneering work of Banin et al.[1] Morphologies of the hybrid structures were fine tuned for exploring complex optical and electronic interactions.[14-31] The excitonic features from the semiconductor and plasmonic features from the metal have different origins; hence their interaction is very complex. Due to the nano sizes of the components, the optical properties of these structures are determined by quantum

confinement in semiconductor and dielectric confinement in metal parts.[32, 33] Recently, Sonnichsen et al.[34] calculated absorption of hybrid nanorods based on the pure electrodynamic interactions between metal and semiconductor components using DDA simulations. In this study, they found that the absorption of Au-CdS retain the optical properties of the original components; while for Au-CdSe system, the absorption is totally different from their individual components. For Au-CdSe, overlap of the Au and CdSe absorbance lead to the mixing of the electronic states of the metal and semiconductor, resulting in a distinct absorption for the hybrid structure. The emission from all these hybrid structures was quenched due to charge transfer from the semiconductor to the metal component. The absorption and emission properties depend on the band energies of the components and interactions vary for each individual system. Hence, in order understand the complex plasmon-exciton interactions, optical properties of many other hybrid systems still need to be explored.

In this study, Ag-CdS rods with three different lengths of the CdS component were fabricated and explored for the optical interactions. High-resolution transmission electron microscopy (HRTEM) and energy dispersive X-ray spectroscopy (EDS) studies confirm the formation of a metal alloy and semiconductor junction. Optical studies showed that the absorption of hybrid rods is broad and red shifted from the Ag seed. Surprisingly, hybrid nanorods still displayed photoluminescence despite the charge transfer between the metal and semiconductor. Furthermore, the emission of the Ag-CdS rods tends to blue shift with the increase in CdS length. Control studies revealed that band edge emission from semiconductor component was quenched, while trap state emission was not effected in the hybrid nanorods. This might be due to different underlying charge transfer

mechanisms between metal and semiconductor components and/or unique band alignments in the hybrid nanorods, which needs to be further verified. Understanding the band alignments in these hybrid structures helps to fine- tune them and improve charge transfer efficiency for photo catalytic and solar cell applications.

5.2 Experimental section

5.2.1 Chemicals

Silver nitrate, sulfur powder, cadmium (II) acetylacetonate (98%), Cadmium acetate dihydrate, trioctylphosphine (95%), oleylamine (70%) were purchased from sigma Aldrich and used without any further purification.

5.2.2 Synthesis of Ag seeds

Ag seeds were prepared by following the protocol developed by Shen et al[35] with some minor changes. 5.0 mL of oleylamine and 51 mg of silver nitrate (0.3 mmol) were degassed for 15 minutes at room temperature in a three-neck flask. Then, Ag precursor was reduced in presence of olelylamine by raising the temperature to 150 °C for 20 minutes to form seeds. The reaction mixture was then cooled to 50 °C to collect the samples. Ethanol was added to the collected samples, followed by centrifugation for 5 minutes at 5000 rpm for two times. After removing the unreacted precursor, the samples were stored in ethanol and further used for the synthesis of Ag-CdS nanorods, Ag-Cd particles within the next 24 hours.

5.2.3 Synthesis of Ag-CdS hybrid nanorods

Ag-CdS nanorods were obtained by following a protocol developed by Chen et al[31] with some minor modifications. 5.0 mg of silver seeds were obtained from previous step by drying out ethanol and dissolving them back into 5.0 mL of oleylamine. This mixture was loaded into three-neck flask and degassed for 10 minutes at room temperature. The temperature was raised to 150 °C and both sulfur and cadmium precursors were injected simultaneously. Sulfur precursor solution was prepared by adding 3.2 mg of sulfur powder (0.1 mmol) to 1ml of oleylamine and dissolved after being sonicated for 5 minutes. Cadmium precursor solution was prepared by dissolving 31 mg of cadmium acetylacetonate (0.1 mmol) in 1.0 mL of oleylamine followed by sonication and heating using hot air gun. The precursors were allowed to react for different amount of reaction time to obtain hybrid nanorods with different CdS part lengths. The collected samples were cooled to 80 °C and ethanol was added, followed by centrifugation at 5000 rpm for 5 minutes. All the samples were washed up to three times with ethanol and toluene solvent mixture to remove unreacted precursors. The resulting precipitate was dispersed in toluene for TEM and optical analysis.

5.2.4 Synthesis of Ag-Cd particles

5.0 mg of Ag seeds collected from previous step were dissolved in 5.0 mL of oleylamine and was loaded into the flask with three necks. The solution was degassed for 15 minutes at room temperature, then the reaction temperature was raise to 150 °C. Once the temperature reached 150 °C, only cadmium precursor was injected. Cadmium precursor solution was prepared by dissolving 31 mg of cadmium acetylacetonate (0.1 mmol) in 1.0 mL of oleylamine followed by sonication and heating using hot air gun. The reaction was allowed to take place for 5 minutes at 150 °C. Then the reaction mixture was cooled to 80

°C and ethanol was added, followed by centrifugation (5000 rpm, 5 min) and washing up to three times with ethanol and toluene. The resulting precipitate was dispersed in toluene for further TEM and optical analysis.

5.2.5 Synthesis of CdS nanorods

To make CdS nanorods, 40 mg of cadmium acetate dihydrate (0.15mM) was loaded into a 25 mL three-necked flask. The precursor was degassed for 15 minutes at room temperature, then 5 mL trioctylphosphine (TOP) was injected into the flask and temperature was raised to 260 °C. Sulfur precursor was injected at 260 °C and allowed to react for 2 hours. Sulfur precursor was made by adding 24 mg of sulfur powder (0.76mmol) into 1mL TOP and sonicated for 1 minute. After 2 hours, reaction mixture was cooled 80 °C, and the sample collected was centrifuged at 5000 rpm for 5 minutes. The sample was washed three times in ethanol and toluene solvent mixture and finally dissolved in toluene for further analysis.

5.2.6 Single Particle Photoluminescence Spectroscopy

To prepare the sample for the single particle studies, 10 μL of highly diluted CdS nanorod solution in toluene was drop casted onto a clean No.1 coverslip (Fisher Scientific) and allowed to dry. The fluorescence of individual QDs was collected with a home-built confocal fluorescence microscope using a Nikon Ti-u microscope equipped with a piezo stage (PI 320, Physik Instrument). The QDs were excited using a Picoquant 405 PDL 800-B pulsed diode laser, focused through a 100x oil-immersion objective (Nikon, NA = 1.3). A 450 nm long pass filter was used to cut off the signal from laser. The emission from the sample was sent to a spectrograph (Isoplane SCT 320, Princeton

Instruments) equipped with a CCD camera (PIXIS 1024 BR, Princeton Instruments). The entrance slit was adjusted so that the signal from a single particle was collected.

5.2.7 Characterization instruments

Ultraviolet- visible (UV-Vis) spectrometer (Cary 60, Agilent technologies**)** was used to measure the absorption spectra of the nanoparticles. A spectrofluorometer (Fluromax plus, Horiba Scientific) was used to measure the ensemble photoluminescence spectra of the samples. Low- resolution transmission electron microscopy (TEM) images were obtained using FEI-Tecnai electron microscope operating at an accelerating voltage of 120 kV. HRTEM, high angle annular dark field microscopy- scanning transmission electron microscopy (HAADF-STEM) images and fast fourier transform (FFT) analysis were obtained using FEI-Talos microscope operating at an accelerating voltage of 200 kV. Elemental analysis was performed using energy dispersive X-ray spectroscopy (EDS) detector attached to the FEI Talos microscope.

5.3 Results and Discussion

5.3.1 Structural Characterization

Sample were collected at 5, 10 and 20 minutes after the injection of Cd and S precursors to obtain the hybrid Ag-CdS nanorods, with three different lengths of CdS component. Figure 5.1 displays the TEM, and the corresponding HRTEM images of the samples obtained. The average diameter of the Ag tip part was determined to be 9.2 ± 1.2 nm, while the length of CdS component (tail) increased with reaction time as seen in Figure 1. In particular, the sample separated at 5 minutes of reaction displayed a shorter tail portion

with a length of 13.1 ± 2.5 nm (L1), similar to the Ag seed size. The contrast between the two regions is clearly seen in the corresponding HRTEM images as shown in Figure 5.1D. The sample separated after 10 minutes had an increased CdS tail length of 33. 4 ± 6.2 nm (L2), as shown in Figure 5.1B. The crystal lattice displays tight and loose packing in the tip and tail portions respectively, as clearly seen in the HRTEM image in Figure 5.1E. The hybrid rods separated after 20 minutes of reaction displayed a longer CdS partcompared to the previous samples as seen in Figure 5.1C and 5.1F. The average

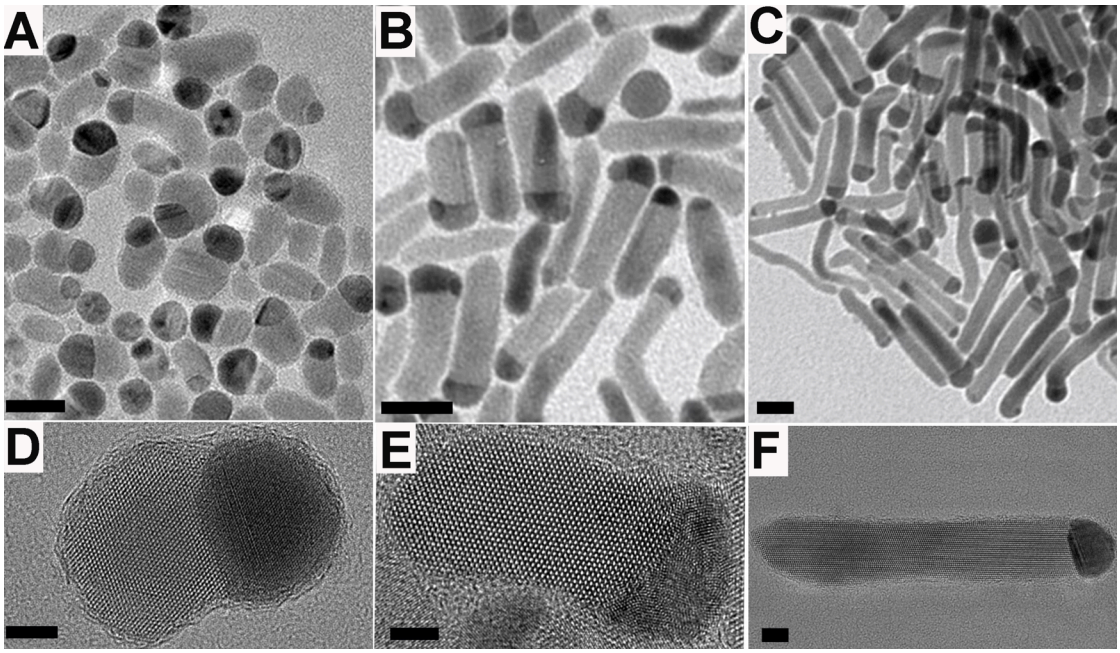

Figure 5.1. TEM images of the samples: Products separated after 5 minutes (A), and at 10 min (B) and 20 min (C) after the injection of Cd and S precursor. (D-F) are the corresponding HRTEM images. Scale bar= 20 nm for (A-C) and 5 nm for (D-F).

length of the CdS part was determined to be 64.4 ± 10 nm (L3). From the TEM and HRTEM, it was clear that CdS is grown on one side of the Ag tip part and the length of the CdS part increased from 13 nm to 65 nm (L1 to L3) with increasing reaction time. HRTEM analysis indicates that both Ag tip and CdS tail are high crystalline in nature.

The dark tip with very tight crystal packing might be Ag, while the low contrast region might correspond the CdS, which further needs to be confirmed with the FFT analysis.

5.3.2 FFT Studies

To confirm the composition and orientation of crystal planes, FFT analysis was performed on the samples separated after 20 minutes of the reaction. The results are summarized in the Figure 5.2. Figure 5.2A displays the HRTEM image of the hybrid rod

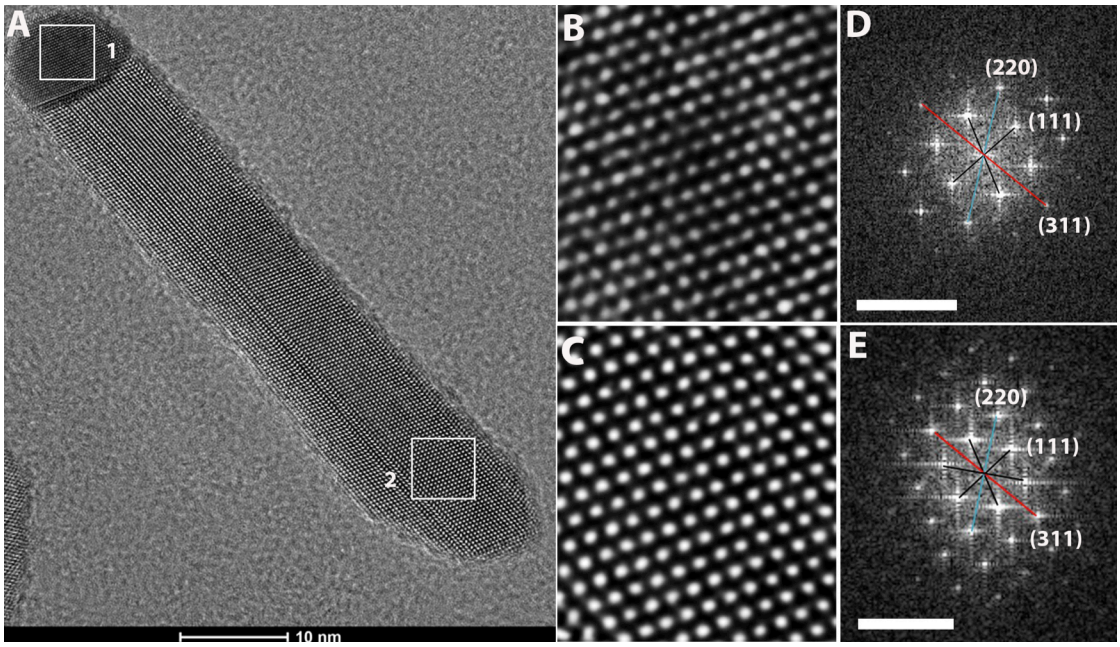

Figure 5.2. (A) HRTEM image of hybrid nanorod separated after 20 min reaction (B and C) are zoomed in images of the boxed regions 1 and 2 from (A). (D and E) are corresponding FFT patterns. The scale bar for (D) and (E) is 10 nm

with a tail length of 65 nm and tip size of 9 nm. The lattice displays twin boundaries across the CdS part indicating the polycrystalline nature, as seen in Figure 5.2A. Figure 5.2B and 5.2C are the zoomed in images of the regions labeled by "1" and "2" in Figure 5.2A. Figure 5.2B and 5.2C display the arrangement of individual atoms and highly crystalline nature of the sample. FFT analysis was performed on 5.2B and 5.2C and the

results are displayed in Figure 5.2D and 5.2E respectively. The d-spacing values of 0.244 nm, 0.152 nm and 0.127 nm in Figure 2D can be indexed as (111), (220) and (311) planes of face centered cubic structure of the Ag. However, these values are slightly higher than 0.232 nm, 0.148 nm, and 0.122 nm of pure Ag fcc lattice, (ICPDS NO: 00-001-1164). This deviation suggests that the tip part is not made of pure Ag. Instead, Cd might have diffused into the tip, as the d-spacing values are close to that of the Ag_3Cd_1 composition (ICPDS NO:01-073-8710). On the other hand the FFT analysis from tail part in Figure 5.2E corresponds to the wurtzite structure of CdS. The measured d-spacing values were 0.336 nm, 0.206 nm and 0.176 nm, which can be indexed as (111), (220) and (311) crystal planes of CdS (ICPDS NO: 00-001-0647). The FFT analysis also confirm that the CdS growth direction was (311) as indicated by red arrow in Figure 5.2E. The FFT analysis indicated that tail portion is made up of pure CdS, while the tip might be a mixture of Ag and Cd, which needs to be further verified.

5.3.3 Elemental Analysis

To figure out the spatial elemental distribution and confirm FFT results, EDS mapping was performed on the samples. The results are summarized in Figure 5.3. Figure 5.3A-C show the HAADF-STEM images of the hybrid nanorods acquired after 5, 10 and 20 minutes of reaction. The other panels in Figure 5.3 represent the EDS mapping images of Ag (red), Cd (green), S (blue) and their corresponding overlays. Figure 5.3A displays high contrast in the tip region compare to the tail part similar to the results obtained by TEM and HRTEM. Distribution of elements clearly indicates Ag (red) was only confined to the high contrast tip region, while S (blue) was present in the tail portion only. In contrast, Cd (blue) was distributed in both the tail and the tip. The distribution of Cd in

the tip portion explains the deviation in the d-spacing values from pure Ag phase as observed in Figure 5.2D. Observation of the overlaid panels corresponding to Ag+Cd and

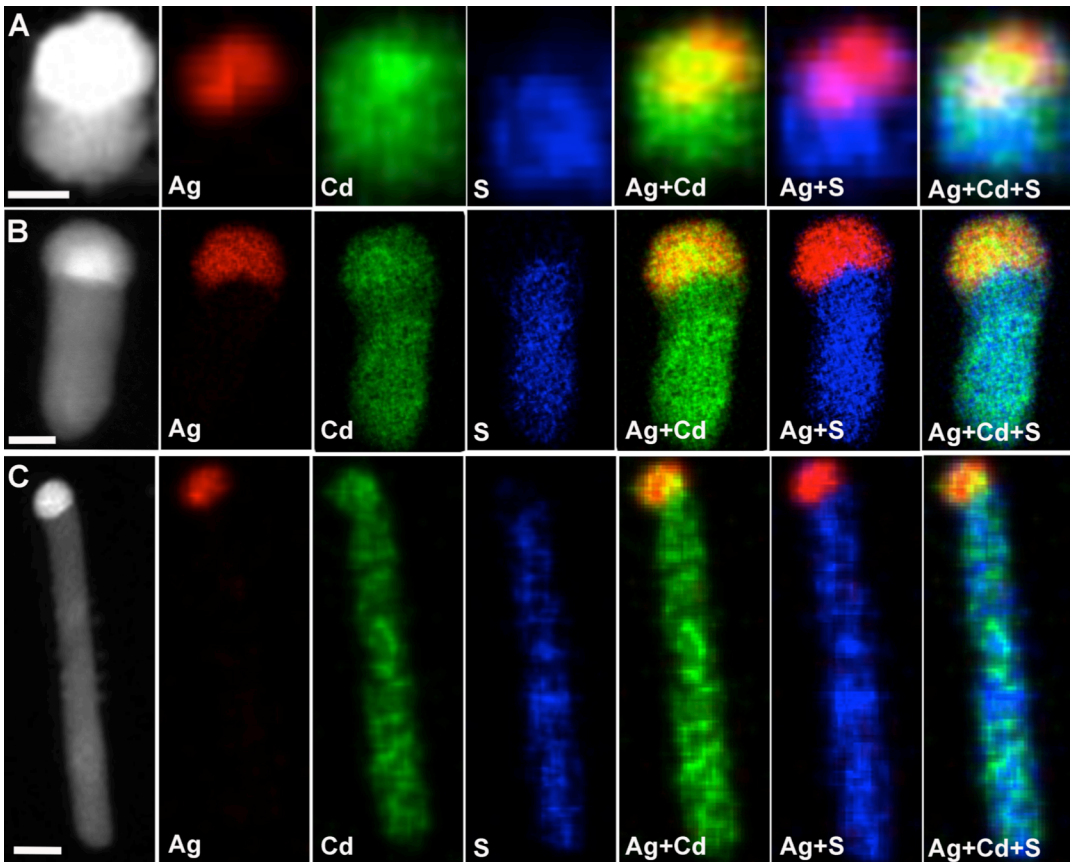

Figure 5.3. EDX elemental mapping images of the hybrid rods obtained at different reaction times (A) 5 min, (B) 10 min, (C) 20. Red represents Ag, Green represents Cd and blue represents S in the images. Scale bar=10 nm.

Ag+S in Figure 5.3A clearly demonstrates the alloying of Cd with Ag in the tip region. The EDS analysis on the other two samples acquired after 10 and 20 minutes of reaction showed similar results, as shown in Figure 5.3B, 5.3C and corresponding panels. The increase in reaction time does not lead to the sulfurization of the tip region. In all the cases Ag or S were confined only to the tip or tail portions, while Cd was distributed all over the hybrid rods.

In order to find out the exact atomic percentage, EDS spectroscopy was performed on all three samples and an example of the results is shown in Figure 5.4. Figure 5 .4A represents the mapping image of the nanorod as seen in Figure 5.3B. Figure 5.4B and 5.4C show the EDS spectrum obtained from regions 1 and 2 from the tail and tip of the nanorod. The analysis indicates that the tail part was made of 53% Cd and 47%

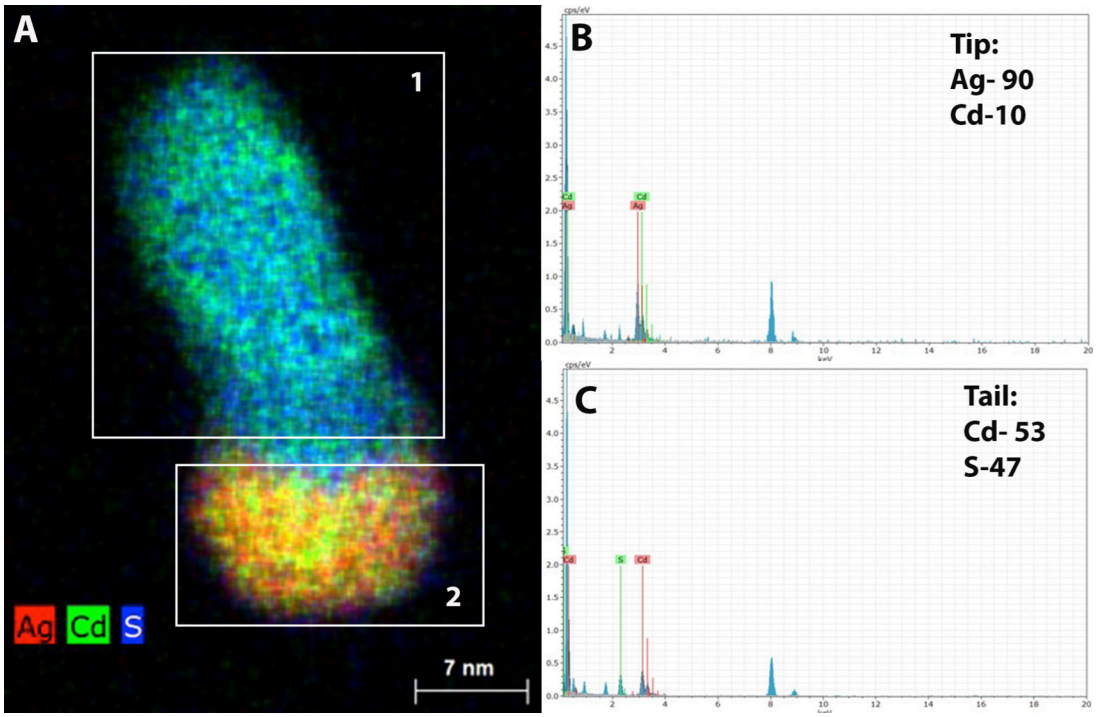

Figure 5.4. EDS spectral analysis of hybrid rod separated at 10 min. (A) elemental mapping and (B and C) EDs spectra obtained from boxed regions 1 and 2 in (A)

S, while the tip was made of 90% Ag and 10% Cd. This analysis further confirms the presence of Cd in the tip region. The results agree well with FFT results and explain the deviation of d-spacing values in Figure 5.2, from pure Ag to Ag_3Cd_1 composition. The TEM analysis in conjunction with EDS studies showed that the hybrid nanorods with three different lengths of CdS, were grown on Ag-Cd tip. Metal and semiconductor parts

were controllably combined into a single nanostructure and corresponding optical interaction between the two needs to be explored.

5.3.4 Optical Properties of Hybrid Nanorods

We measured the absorption and photoluminescence spectra of the hybrid nanorods in order to understand their optical properties. The results obtained are summarized in Figure 5.5. Figure 5.5A shows the ensemble UV-Vis spectra of the hybrid rods of three different CdS lengths, L1= 13 nm, L2= 33 nm and L3 = 65 nm. Hybrid nanorods of length L1 (black) have a single peak around 420 nm. FWHM of the peak was approximately 120 nm. Similarly, the hybrid nanorods of length L2 (red) displayed a single peak around 425 nm, which is slightly red shifted compared to that of the L1 rods. The longer rods of length L3 (blue) have different line shape compared to that of the

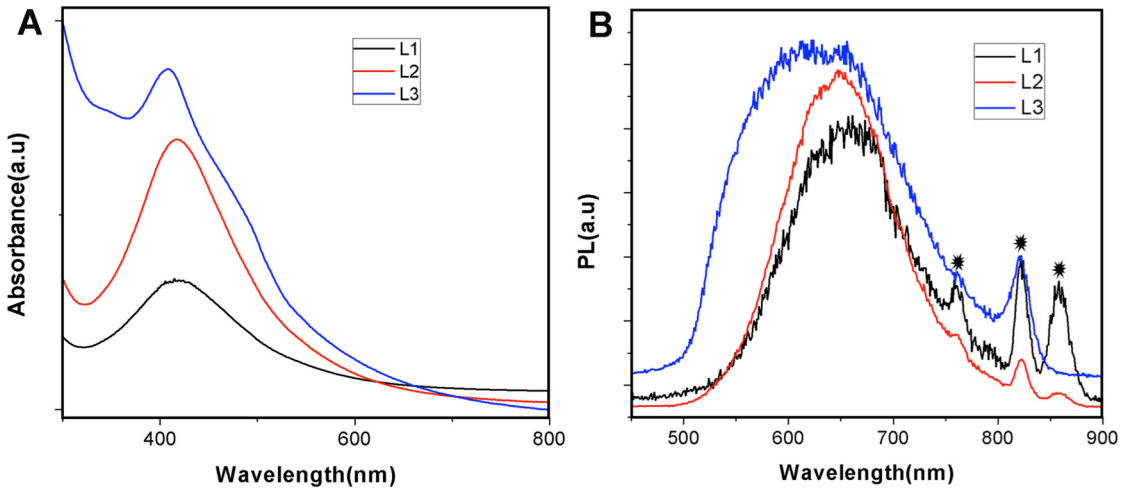

Figure 5.5. Optical properties of AgCd-CdS hybrid rods. (A) absorption (B) photoluminescence of three hybrid rod samples L1=13nm, L2=33nm, L3=65 nm

other two lengths. The longer rods displayed a narrow peak at 415 nm, with a broad shoulder around 485 nm as shown in Figure 5.3A. Overall, L1 and L2 have displayed

only a single broad absorption peak regardless of two absorbing components present in the nanorods (metal and semiconductor). In contrast, L3 displayed two features from both the metal and semiconductor components. The results show the effect of CdS length on the absorption of hybrid structures.

Photoluminescence (PL) spectroscopy was performed on the nanorods to understand the influence of the metal on the emission of the semiconductor. The results are summarized in Figure 5.5B. Surprisingly, all the three hybrid nanorods displayed PL as shown in Figure 5.5B. The PL major peak was at 658, 650 and 623 nm for hybrid rods with the lengths L1, L2 and L3 respectively, while the FWHM was110, 120 and 200 nm. A clear trend of blue shift and increase in FWHM is observed in the PL spectra with increase in

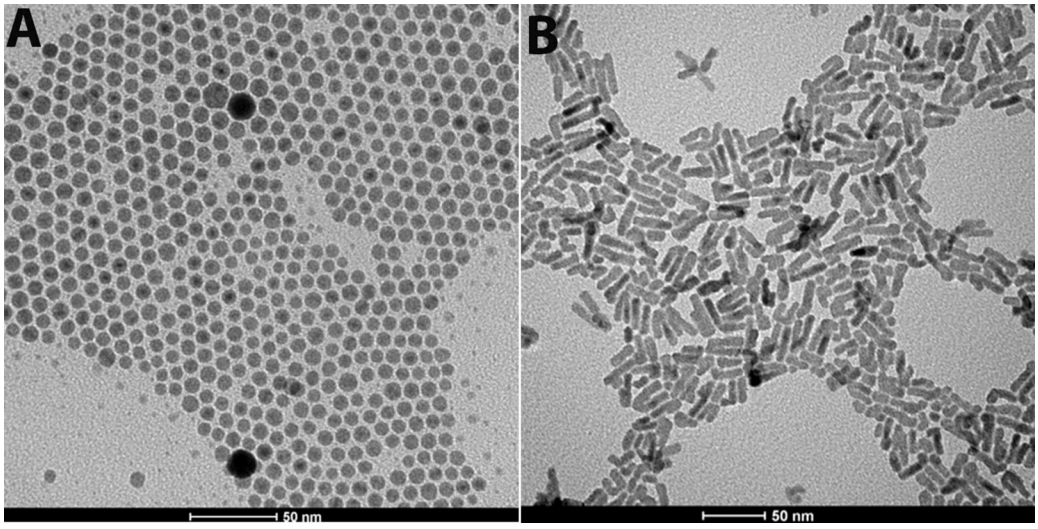

Figure 5.6. TEM images of the (A) Ag seeds (B) CdS nanorods

the CdS length. The additional peaks around 760 nm, 820 nm and 860 nm (marked by asterisk) were likely from random scattering of light in the system. Previously reported semiconductor hybrid nanostructures didn't exhibit PL due to the non-radiative transfer of the excited electron from the semiconductor component into the metals Fermi level.[4] In

order to understand these unique absorption and emission properties of the hybrid systems, optical properties of the individual components was required.

Control experiments were performed on Ag seeds and CdS rods, as shown in Figure 5.6. The Ag seeds prepared in olelyamine were washed three times in ethanol and toluene and dispersed in toluene for structural and optical studies. The average diameter of the Ag seeds was determined to be 10 nm. The CdS nanorods were made in TOP and dispersed

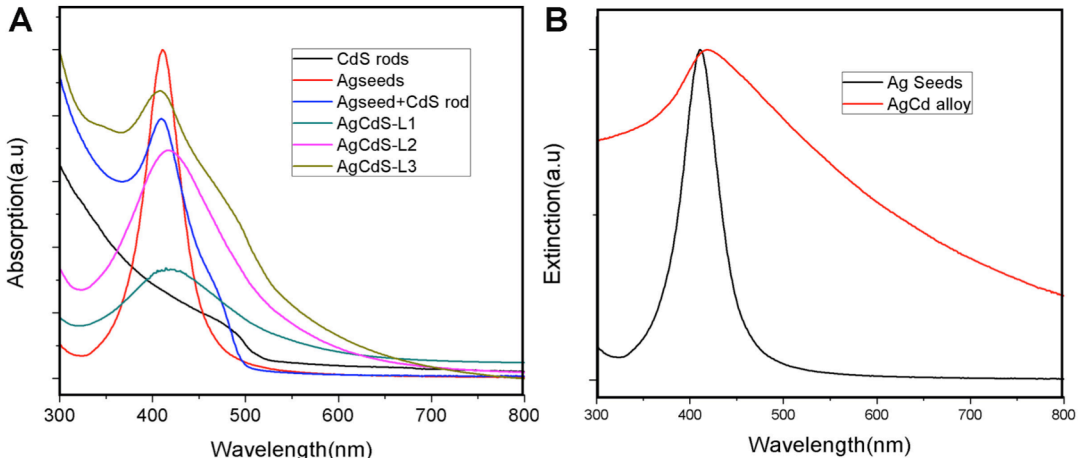

Figure 5.7. Absorption properties of different samples (A) comparing absorption of Ag seeds, CdS rods and Ag+CdS mixture with hybrid rods lengths L, L2 and L3. (B) Comparison of absorption of Ag seeds with Ag-Cd alloy particles

in toluene. The TEM image of the nanorods is shown in Figure 5.6B. The length of nanorods is 27± 3 nm, comparable to the hybrid nanorods of length L2. The extinction of the Ag seeds and absorption of CdS rods were obtained for comparison. To understand how they interact when separated in solution, Ag seeds and CdS nanorods were mixed in 1:1(V/V) ratio and the absorption spectrum of the mixture was measured. The absorption of the individual components and the mixture were compared with that of the hybrid rods. All the results are summarized in Figure 5.7A. The Ag seeds displayed a narrow peak around 415 nm (red spectra) due to localized surface

plasmon resonance (LSPR).[36,37] The narrow peak width indicated uniform size distribution of the seed sample. On the other hand, CdS nanorods displayed a broad absorption band around 480 nm (black spectra). This was consistent with the previous studies, as the band gap for CdS system is 2.4 eV.[38-40] When Ag seeds and CdS nanorods were mixed, they displayed absorption, which is a linear combination of the two components (Figure 5.7A, blue line). But, when these two components were combined into a single structure, hybrid nanorods L1 and L2 displayed a single peak, which is red shifted and broadened compared to Ag seeds. This might be due to the asymmetric dielectric constant around the silver tips or alloying of Cd into Ag tip. The absorption of longer rods L3 was similar to that of the Ag seed and CdS rod mixture, indicating that they behave as separate components as the length of CdS part is increased above 50 nm. This indicated that the interaction of metal part with the semiconductor component is localized in space.

To explain the FWHM of L1 and L2 peaks, control experiments were performed to make Ag-Cd alloy particles and the absorption obtained is shown in Figure 5.7B. The Ag-Cd alloy particles displayed a broad peak around 440 nm. Structural characterization and elemental analysis were performed on Ag-Cd samples. Figure 5.8A shows the STEM image of Ag-Cd particles, and size distribution was found to be similar to that of the Ag seeds. The EDS mapping results shown in Figure 5.8B-E confirmed the presence of Cd in the sample and the particles were alloyed. Alloying of Cd into Ag tip might be one of the reasons for the redshift and broadening of the absorption spectra of hybrid nanorods. Also, formation of mixed electronic states at the junction region was proved through STEM studies previously.[4] Recently Sonnichsen et al.[34] reported formation of mixed

electronic states in hybrid structures, when the absorptions of the components overlap.

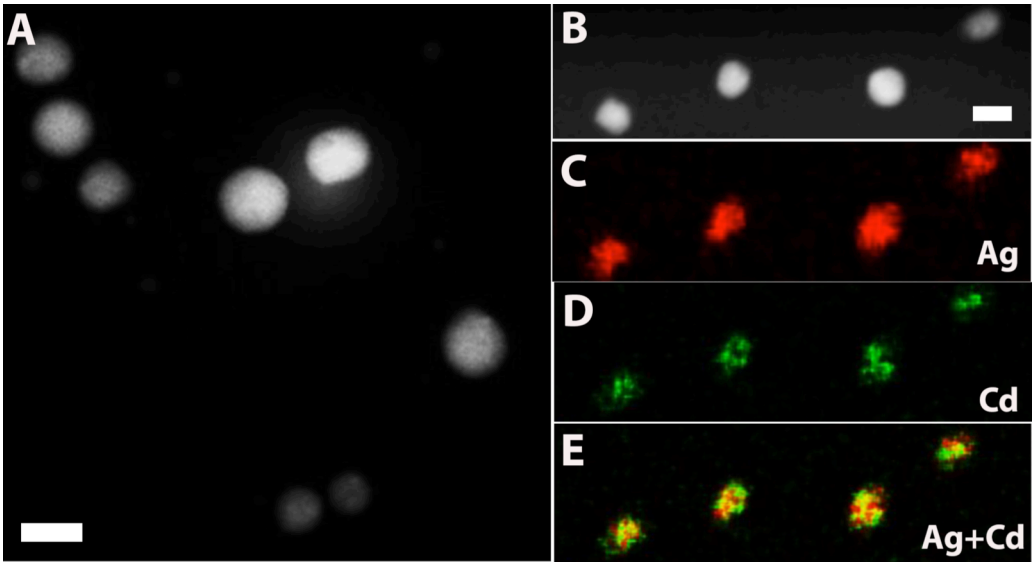

Figure 5.8. STEM and EDS of Ag-Cd alloy particles (A) STEM images of Ag-Cd particles. (B-E) EDS mapping (C) Red is Ag, (D) green is Cd and (E) is overlay

Since, Ag and CdS absorptions overlap in our hybrid rods, formation of mixed states was believed to be the cause for unique absorption patterns. But further calculations are required to support these conclusions. [34]

To explain the PL of the hybrid nanorods, both ensemble and single particle PL of CdS nanorods was performed and results are summarized in Figure 5.9. The ensemble PLdisplayed a narrow peak at 509 nm and broadband from 600-800 nm, as shown in Figure 5.9A. The narrow band was due to band edge emission, while the broad band was from trap state emission, due to presence of surface defects as reported in the literature.[41] The additional features around 540 and 580 nm were expected to be from solvent scattering. To further confirm this, single particle PL was performed by drop coating highly diluted CdS rods on a cover glass. The single particle PL displayed only two peaks

as shown in Figure 5.9B. The two peaks correspond to band edge emission and trap state emission as mentioned before. Hence, other features in ensemble PL are from the solvent scattering. Ensemble and single particle PL both display a strong trap state emission.[41] When the metal tip was attached to CdS, the emission from hybrid nanorods was modified, as seen in Figure 5.5B. The band edge emission from CdS was completely quenched, as we don't see any features around 500 nm for all the three lengths of hybrid rods. The large FWHM of the PL spectra of hybrid rods and blue shift trend with increase in the length suggest that PL was not due to band edge emission. Also, wavelengths of hybrid rod emissions match well with trap state emission from the CdS rods. Hence, the

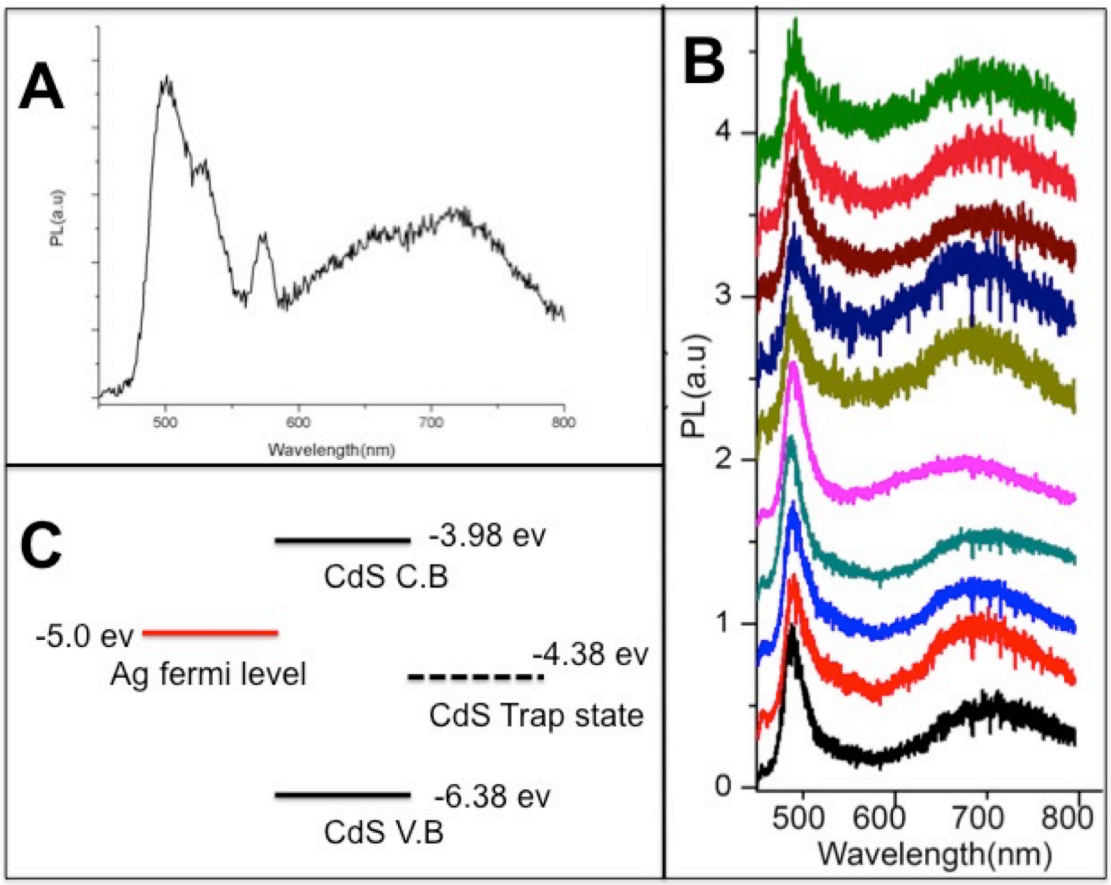

Figure 5.9. Photolumniscence and band alignnments in Cds and Ag-Cds rods. (A and B) ensemble and single particle PL of CdS rods. (C) band alignment in Ag-CdS rods

emission from hybrid nanorods was expected to be from the trap state. The quenching of the band edge emission is due to charge transfer process from CdS conduction band to Ag Fermi level. The expected band alignment for hybrid Ag-CdS rods are shown in Figure 5.9C, as reported in the literature.[31] Since, the trap states are at low energies compared to the Fermi level of Ag as shown in Figure 5.9C, charge transfer phenomenon might not effect the trap state emission. Further time resolved absorption and PL spectroscopy studies along with calculations might confirm these conclusions.

5.4 Conclusion

Metal-semiconductor Ag-CdS hybrid nanorods of three different lengths were synthesized. The TEM, HRTEM and EDS analysis indicate that the metal part is an alloy of Ag and Cd, but sulfurization was absent. The hybrid rods of 13 and 33 nm CdS length, displayed a red shifted broad absorbance compared to Ag seeds. Asymmetric dielectric function and mixed electronic states caused these changes in line shape. But, when the length of CdS part was 65 nm, the Ag-CdS rods had an absorption feature similar to that of the mixture of Ag seeds and CdS rods. The hybrid nanorods also showed PL despite of charge transfer process to metal component. The PL peak blue shifted with the increase in the CdS length. Control studies revealed that band edge emission from semiconductor was quenched, while trap state emission was not effected in the hybrid nanorods. The band alignments in the hybrid nanorods need to be further explored for wide applications in photo catalysis and solar cells.

5.5 References

1. T. Mokari, E. Rothenberg, I. Popov, R. Costi and U. Banin, *Science*, 2004, **304**, 1787-1790.
2. T. Mokari, *Nano Rev*., 2011, **2**, 10.3402/nano.v3402i3400.5983.
3. A. Vaneski, A. S. Susha, J. Rodríguez-Fernández, M. Berr, F. Jäckel, J. Feldmann and A. L. Rogach, *Adv. Funct. Mater*., 2011, **21**, 1547-1556.
4. U. Banin, Y. Ben-Shahar and K. Vinokurov, *Chem. Mater*., 2014, **26**, 97-110.
5. V. Subramanian, E. E. Wolf and P. V. Kamat, *J. Am. Chem. Soc*., 2004, **126**, 4943-4950.
6. Y. Shemesh, J. E. Macdonald, G. Menagen and U. Banin, *Angew. Chem. Intl. Ed*., 2011, **50**, 1185-1189.
7. H. Song, *Acc. Chem. Res*., 2015, **48**, 491-499.
8. M. Gratzel, *Nature*, 2001, **414**, 338-344.
9. L. Zhou, X. Yu and J. Zhu, *Nano Lett*., 2014, **14**, 1093-1098.
10. M. T. Sheldon, P.-E. Trudeau, T. Mokari, L.-W. Wang and A. P. Alivisatos, *Nano Lett*., 2009, **9**, 3676-3682.
11. M. Achermann, *The J. Phys. Chem. Lett*., 2010, **1**, 2837-2843.
12. R. Lavieville, Y. Zhang, A. Casu, A. Genovese, L. Manna, E. Di Fabrizio and R. Krahne, *ACS Nano*, 2012, **6**, 2940-2947.
13. A. Figuerola, I. R. Franchini, A. Fiore, R. Mastria, A. Falqui, G. Bertoni, S. Bals, G. Van Tendeloo, S. Kudera, R. Cingolani and L. Manna, *Adv. Mater*., 2009, **21**, 550-554.
14. S. E. Habas, P. Yang and T. Mokari, *J. Am. Chem. Soc*., 2008, **130**, 3294-3295.
15. I. Jen-La Plante, S. E. Habas, B. D. Yuhas, D. J. Gargas and T. Mokari, *Chem. Mater*., 2009, **21**, 3662-3667.
16. S. Naskar, A. Schlosser, J. F. Miethe, F. Steinbach, A. Feldhoff and N. C. Bigall, *Chem. Mater*., 2015, **27**, 3159-3166.
17. K. Wu, Z. Chen, H. Lv, H. Zhu, C. L. Hill and T. Lian, *J. Am. Chem. Soc*., 2014, **136**, 7708-7716.
18. G. Manna, R. Bose and N. Pradhan, *Angew. Chem. Intl. Ed*., 2014, **53**, 6743-6746.

19. Y. Kim, K. Y. Park, D. M. Jang, Y. M. Song, H. S. Kim, Y. J. Cho, Y. Myung and J. Park, *J. Phys. Chem. C*, 2010, **114**, 22141-22146.
20. S. Liang, X.-L. Liu, Y.-Z. Yang, Y.-L. Wang, J.-H. Wang, Z.-J. Yang, L.-B. Wang, S.-F. Jia, X.-F. Yu, L. Zhou, J.-B. Wang, J. Zeng, Q.-Q. Wang and Z. Zhang, *Nano Lett.*, 2012, **12**, 5281-5286.
21. L. J. Hill, M. M. Bull, Y. Sung, A. G. Simmonds, P. T. Dirlam, N. E. Richey, S. E. DeRosa, I.-B. Shim, D. Guin, P. J. Costanzo, N. Pinna, M.-G. Willinger, W. Vogel, K. Char and J. Pyun, *ACS Nano*, 2012, **6**, 8632-8645.
22. P. Li, Z. Wei, T. Wu, Q. Peng and Y. Li, *J. Am. Chem. Soc.*, 2011, **133**, 5660-5663.
23. D. D. Fanfair and B. A. Korgel, *Crys. Growth Des.*, 2008, **8**, 3246-3252.
24. J. V. Embden, A. S. R. Chesman, J. J. Jasienaik, *Chem. Mater.*, 2015, **27**, 2246.
25. T. Aiwei, W. Yu, Y. Haihang, Z. Chao, Y. Chunhe, L. Xu, P. Hongshang, Z. Fujun, H. Yanbing and T. Feng, *Nanotechnology*, 2013, **24**, 355602.
26. V. Fernàndez-Altable, M. Dalmases, A. Falqui, A. Casu, P. Torruella, S. Estradé, F. Peiró and A. Figuerola, *Chem. Mater.*, 2015, **27**, 1656-1664.
27. F. Wang, A. Dong, J. Sun, R. Tang, H. Yu and W. E. Buhro, *Inorg. Chem.*, 2006, **45**, 7511-7521.
28. F.-R. Fan, Y. Ding, D.-Y. Liu, Z.-Q. Tian and Z. L. Wang, *J. Am. Chem. Soc.*, 2009, **131**, 12036-12037.
29. S. Barth, J. J. Boland and J. D. Holmes, *Nano Lett.*, 2011, **11**, 1550-1555.
30. H. Shen, H. Shang, J. Niu, W. Xu, H. Wang and L. S. Li, *Nanoscale*, 2012, **4**, 6509-6514.
31. S. Chen, S. Thota, G. Reggiano and J. Zhao, *J. Mater. Chem. C*, 2015, **3**, 11842-11849.
32. A. P. Alivisatos, *J. Phys.Chem.*, 1996, **100**, 13226-13239.
33. S. Eustis and M. A. El-Sayed, *Chem. Soc. Rev.*, 2006, **35**, 209-217.
34. E. Shaviv, O. Schubert, M. Alves-Santos, G. Goldoni, R. Di Felice, F. Vallée, N. Del Fatti, U. Banin and C. Sönnichsen, *ACS Nano*, 2011, **5**, 4712-4719.
35. C. Shen, C. Hui, T. Yang, C. Xiao, J. Tian, L. Bao, S. Chen, H. Ding and H. Gao, *Chem. Mater.*, 2008, **20**, 6939-6944.

36. K. M. Mayer and J. H. Hafner, *Chem. Rev.*, 2011, **111**, 3828-3857.
37. M. Rycenga, C. M. Cobley, J. Zeng, W. Li, C. H. Moran, Q. Zhang, D. Qin and Y. Xia, *Chem. Rev.*, 2011, **111**, 3669-3712.
38. J. Planelles, F. Rajadell and J. I. Climente, *J. Phys. Chem. C*, 2010, **114**, 8337-8342.
39. F. Wang, A. Dong and W. E. Buhro, *Chem. Rev.*, 2016, **116**, 10888-10933.
40. P. Thakur, S. S. Joshi, S. Kapoor and T. Mukherjee, *Langmuir*, 2009, **25**, 6377-6384.
41. A. E. Saunders, I. Popov and U. Banin, *J. Phys. Chem. B*, 2006, **110**, 25421-25429.

Appendix

List of Publications and Presentations

Journal Articles

First Author

1. **Thota, S**., Chen, S., Zhang, Y., Zou, S., and Zhao, J. " Structural Defect Induced Peak Splitting in AuCu Bimetallic Nanorods ", *Nanoscale*, (2015), *7*, 14652.

2. **Thota, S**., Chen, S., Zhao, J. "An Unconventional Mechanism of Hollow Nanorod Formation: Asymmetric Cu Diffusion in Au-Cu Alloy Nanorods during Galvanic Replacement Reaction", *Chemical Communications*, (2016), *52*, 5593.

3. **Thota, S**., Chen, S., Zhao, J. "Formation of Bimetallic Dumbbell Shaped Particle with a Hollow Junction during Galvanic Replacement Reaction", *Nanoscale*, (2017), *9*, 6128.

4. **Thota, S**., Zhao, J. "Tuning optical properties of metal- semiconductor hybrid nanorods by varying semiconductor part length", *Manuscript in preparation*

5. **Thota, S**., Zhao, J. "Synthesis, Optical and Catalytic Properties Au-Cu alloy nanoparticles", (Invited Review), *Manuscript in preparation*

Co-author

6. Tian, X., Zhou, Y., **Thota, S**., Zou, S., Zhao, J. "Plasmonic Coupling in Single Silver Nanosphere Assemblies by Polarization Dependent Dark-Field Scattering Spectroscopy." *The Journal of Physical Chemistry C* (2014), *118*, 13801.

7. Jenkins, A, J., Zhou, Y, **Thota, S**., Tian, X., Zhao, X., Zou, S., Zhao, J. "Blue-Shifted Narrow Localized Surface Plasmon Resonance from Dipole Coupling in

Gold Nanoparticle Random Arrays", *The Journal of Physical Chemistry C* (2014), *118*, 26276.

8. Chen, S., **Thota, S**., Reggiano, G., Zhao, J. "Generalized seeded growth of Ag-based metal chalcogenide nanorods *via* controlled chalcogenization of the seeds", *Journal of Materials Chemistry C*, (2015), *3*, 11842.

9. Dey, S., Chen, S., **Thota, S**., Shakil, Md. R., Suib, S., Zhao, J. "Effect of Gradient Alloying on Photoluminescence Blinking of Single CdSSe Nanocrystals", *Journal of Physical Chemistry C*, (2016), *120 (37)*, 20547.

10. Mazrui, N., Jonsson, S., **Thota, S**., Zhao, J., Mason, R., "Enhanced availability of mercury bound to dissolved organic matter for methylation in marine sediments", *Geochimica et Cosmochimica Acta*, (2016), *194*, 153.

11. Vijayan, S., **Thota, S**., Zhao, J., Aindow, M., "In Situ TEM Heating Experiments on PVP-Capped Silver Nano-Cubes", *Microscopy and Microanalysis,* (2016), *22 (S3)*, 822.

12. Chen, S., **Thota, S**., Wang, X., Zhao, J. "From Solid to Core@Shell to Hollow Pt-Ag nanocrystals: Thermally Controlled Surface Segregation to Enhance Catalytic Activity and Durability", *Journal of Materials Chemistry A*, (2016), *4*, 9038-9043(Hot Article).

13. Chen, S., Reggiano, G., **Thota, S**., Zhao, J., "Au-Cu-Ag Nanorods synthesized by Seed-medicated Co-reduction and Their Optical Properties", *Particle & Particle Systems Characterization*, (2017), 1600384.

14. Tan, R., Yuan, Y., Nagaoka, Y., Eggert, D., Wang, X., **Thota, S**., Guo, P., Yang, H., Zhao, J., Chen, O., "Monodisperse Hexagonal Pyramidal and Bipyramidal Wurtzite CdSe-CdS Core-Shell Nanocrystals", *Chemistry of Materials*, (2017), *29(9)*, 4097.

15. Chen, S., **Thota, S**., Koenigsmann, C., Zhao, J., "Synthesis of Hollow Pt-Ag Nanoparticles by Oxygen-Assisted Acid Etching as Electrocatalysts for the Oxygen Reduction Reaction", *ChemCatChem*, (2017), under review.

16. Lu, L., Chen, S., **Thota, S**., Wang, X., Zou, Y., Fan, S., Zhao, J., "Composition Controllable Synthesis of PtCu Nanodendrites with Efficient Electrocatalytic Activity for Methanol Oxidation Induced by High Index Surface and Electronic Interaction", *The Journal of Physical Chemistry C*, (2017), under review

17. Mazrui, N., King'ondu, K., Awino, J., **Thota, S**., Zhao, J., Jessica Rouge Mason, R., "The Precipitation, Growth and Stability of β-HgS Nanoparticles Formed in Presence of Marine Dissolved Organic Matter", *Environmental Science: Processes & Impacts*, (2017), under review

Conference Presentations

1. 252nd ACS Meeting & Exposition, Philadelphia, Pennsylvania, August 21st – 25th, 2016. (Poster)-Outstanding Poster Award

2. Gordon Research Conference: Noble Metal Nanoparticles, South Hadley, Massachusetts, June 19th – 24th, 2016. (Poster)

3. MRS Fall Meeting & Exhibit, Boston, Massachusetts, November 29th–December 4th, 2015. (Poster)

4. 250nd ACS Meeting & Exposition, Boston, Massachusetts, August 16th–20th, 2015. (Poster)

5. Gordon Research Conference: Nanomaterial's for Application in Energy Technology, Ventura, California, February 22nd – 27th, 2015. (Poster)